CHALMERS
UNIVERSITY OF TECHNOLOGY

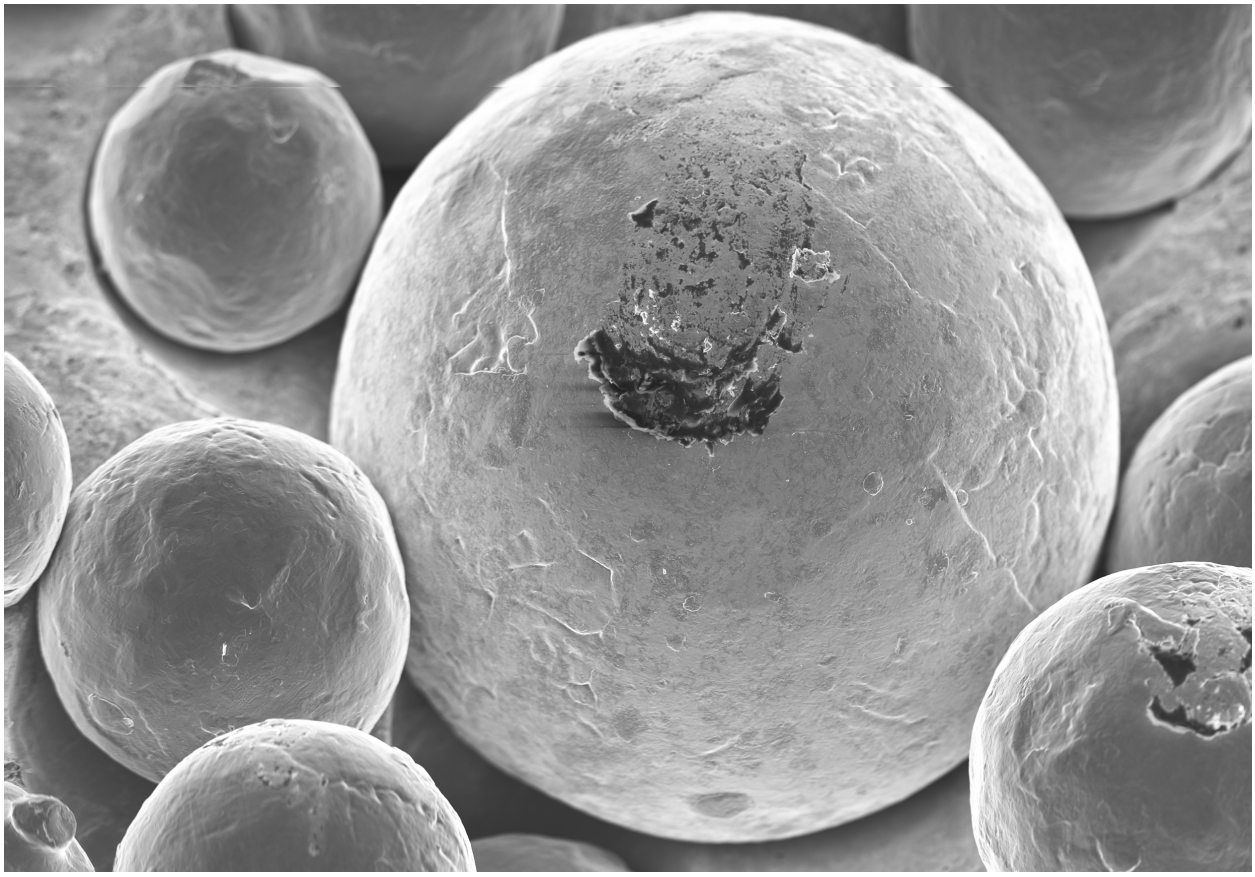

Understanding process atmosphere interactions in Electron Beam Powder Bed Fusion (EB-PBF) additive manufacturing

An assessment of the low-pressure process atmosphere composition and its effect on Ti-6Al-4V powder

Master's thesis in Materials Engineering

OSKAR BURGMAN & CHRISTIAN LUNDBERG

DEPARTMENT OF INDUSTRIAL AND MATERIALS SCIENCE

CHALMERS UNIVERSITY OF TECHNOLOGY
Gothenburg, Sweden 2021
www.chalmers.se

Master's thesis 2021

Understanding process atmosphere interactions in Electron Beam Powder Bed Fusion (EB-PBF) additive manufacturing

An assessment of the low-pressure process atmosphere composition and its effect on Ti-6Al-4V powder

Master's thesis in Materials Engineering

OSKAR BURGMAN & CHRISTIAN LUNDBERG

CHALMERS
UNIVERSITY OF TECHNOLOGY

Department of Industrial and Materials Science
Division of Materials and Manufacture
Chalmers University of Technology
Gothenburg, Sweden 2021

Master's Thesis
Understanding process atmosphere interactions in Electron Beam Powder Bed Fusion (EB-PBF) additive manufacturing.
An assessment of the low-pressure process atmosphere composition and its effect on Ti-6Al-4V powder

Master's thesis in Materials Engineering
OSKAR BURGMAN & CHRISTIAN LUNDBERG

Examiner: Prof. Eduard Hryha, Department of Industrial and Materials Science
Supervisor: Bo Williamsson, Linde Gas AB
Supervisor: Dr. Joakim Ålgårdh, GE Additive/Arcam

Master's Thesis 2021
Department of Industrial and Materials Science
Division of Materials and Manufacture
Chalmers University of Technology
SE-412 96 Gothenburg
Telephone +46 31 772 1000

Cover: SEM picture of a smiling powder particle captured by the authors.

Typeset in LaTeX
Gothenburg, Sweden 2021

Master's Thesis
Understanding process atmosphere interactions in Electron Beam Powder Bed Fusion (EB-PBF) additive manufacturing.
An assessment of the low-pressure process atmosphere composition and its effect on Ti-6Al-4V powder
OSKAR BURGMAN & CHRISTIAN LUNDBERG
Department of Industrial and Materials Science
Chalmers University of Technology

Abstract

The composition of the process atmosphere and its effect on the Ti-6Al-4V powder during Electron Beam Melting with an Arcam Q20plus was studied. Oxygen concentration and water vapour content were monitored in-situ in the build chamber and in the gas exiting the chamber, using lambda sensors and a dew point meter. Composition changes were analysed in the process atmosphere using mass spectrometry and in Ti-6Al-4V powder, using X-ray photoelectron spectroscopy, Inert Gas Fusion Analysis, and Scanning Electron Microscopy. Results show that the low supply of oxygen introduced from the process atmosphere result in the moderate increase in oxygen content, measured in the powder. The powder used had a high initial oxygen concentration, which could also explain the low oxygen pick-up seen in the study. A limited increase in oxide layer thickness can be observed on the studied powder, in agreement with the moderate increase in general oxygen content. The powder morphology and overall visual appearance studied in scanning electron microscopy also remained unchanged. The study also shows that residual air and water are notable constituents of the process atmosphere as the process starts. These constituents are gradually replaced by helium during the first few hours of the manufacturing process, while preheating occurs, where the oxygen content stabilises to a partial pressure below 0.1 ppm in the process. This is within the limit of oxygen contained in the helium. No significant variations in the oxygen content in the atmosphere between builds was registered. The gas flow exiting the Q20plus proved to be insufficient for the extractive lambda sensor and the dew point meter, rendering them unusable for this specific process. The mass spectrometry results potentially indicate minor air leaks into the vacuum chamber, as the relative amounts of nitrogen remain stable.

Keywords: additive manufacturing, electron beam melting (EBM), Ti-6Al-4V, powder, vacuum, oxygen uptake, mass-spectrometry, process gas monitoring

Acknowledgements

This thesis would not have been possible without the help of many fantastic people. It was performed as a collaboration between CAM^2 at Chalmers University of Technology, GE Additive, and Linde Gas AB. A big thanks to everyone involved at Arcam, Chalmers, and Linde Gas.

A special thanks to,

Eduard Hryha, for your guidance and wisdom during this thesis.

Joakim Ålgårdh, for believing in us and making this thesis possible.

Oskar Zeilinski and Tobias Skattberg, for your unconditional helpfulness with everything related to making this thesis progress, and also for the good times.

Ahmad Raza, for the helpful discussions and for aiding us in our analysis.

Martin Plomgren, for your good mood and your tireless work in the materials lab at Arcam.

Urban Andner, for the operator's course and your willingness to stop by and help us when needed.

Bo Williamsson and Anders Åström, for your patience and help during the many consultation meetings.

Luca Girotto, for happily helping us with the installation of the sensors.

Oskar Burgman & Christian Lundberg, Gothenburg, July, 2021

Glossary

AM Additive Manufacturing. 1

APA Advanced Plasma Atomization; a method to produce powder for Powder Bed Fusion . 9, 10

CAM^2 Centre for Additive Manufacturing – Metal. 2

DP A designation for the dew point meter manufactured by Vaisala. 17

EB-PBF Electron Beam Powder Bed Fusion. 1, 2

EBM Electron Beam Melting; a registered trademark of Arcam AB. 2

EBU Electron Beam Unit; the module containing the cathode among other components. 17

EMF Electromotive force; difference in electric potential. 13

IGFA Inert Gas Fusion Analysis; a method for quantitatively establish oxygen and nitrogen concentration in a sample. 2

metallisation Metallic coating; a deposition of aluminium that can be found inside the EB-PBF printer after a print cycle. 2

MS Mass spectrometry; an analytical technique that is used to measure the mass-to-charge ratio of ions which produces an isotopic signature of a sample. 26

ODE Ordinary differential equation. 23

POA A designation for the oxygen sensor trademarked as OXYSENSOR ™ POA by Linde Gas AB. 17

PRS Powder Recovery System; a system to enable powder recovery of a build. 1, 8, 11, 19

SATP Standard Ambient Temperature and Pressure; used in conjunction with the ideal gas law when standard conditions are present. Defined as 298.15 K and 100 kPa. 23

SEM Scanning Electron Microscopy; a method to look at external morphology, crystal orientation and chemical composition in conductive materials. 2

smoke A powder cloud formed inside the build chamber, caused by the repelling forces from the built-up charge on the powder. 7

T90 A measurement of the response time of a gas detector. 14

VAC A designation for the vacuum adapted oxygen sensor trademarked as OXYSENSOR™ VAC by Linde Gas AB. 17

XPS X-ray Photoelectron Spectroscopy; a surface-sensitive method to analyse the chemical composition of a material. 2

Contents

1
Introduction

Additive manufacturing (AM) has, in recent years, emerged as a viable candidate for the manufacturing of complex components with highly reduced weight and assembly complexity. While regularly manufactured parts involve many different process steps and a final component assembly, additive manufacturing inherently offers part complexity "for free" [1]. Some of the challenges faced when delving into additive manufacturing include considering the process atmosphere. It is widespread in the materials community that Ti-6Al-4V has a particular affinity for oxygen. Previous research has tracked the oxygen uptake and the powder's recyclability in the Electron Beam Melting process, but the process atmosphere interactions are not fully understood. While quite well-studied in laser-based processes, which occur at near atmospheric pressures, the effect of the process atmosphere in Electron Beam Powder Bed Fusion (EB-PBF) has seen less research. The powder in an Electron Beam Melting process experiences prolonged time at elevated temperatures, at a high vacuum, creating a complicated oxidation process during the print. The material and electron beam interactions with the process atmosphere further complicate the process and its results. Thus, it is of great interest to track the process atmosphere's role in the process and how it affects the analysed powder.

1.1 Background

Due to its high surface area, metal powder possesses high reactivity and is prone to oxidation and water accumulation when subject to an unprotected atmosphere. Several studies show that Ti-6Al-4V powder degrades and oxidises after each EBM process cycle [2][3]. These factors will also depend on the alloy composition, powder handling, AM processing as well as re-use during AM processing [4]. Oxygen pick-up will gradually change the material properties, leading to higher strength and increased brittleness [2]. Furthermore, oxygen inclusions can have a detrimental effect on printed components' mechanical properties, especially fatigue. [2].

Previous research has shown that most of the oxygen pick-up occurs during the build cycle [5]. The other stages related to the EBM-process e.g. powder handling during PRS and loading, vacuuming of recovered powder, shown in figure 1.1, do not entail a significant oxygen increase in the powder [5]. However, these stages can lead to increased water content in the powder, which later disassociates during the printing cycle forming hydrogen, hydroxyl groups and oxygen. The results also showed a

rather significant amount of water vapour in the low-pressure atmosphere, which is partially introduced from the powder. The same study shows that water is also introduced in the vacuum chamber from air when it is under atmospheric pressure. Metallisation covering the internal surfaces will also adsorb water from the air. The metallisation is a product of metal vaporising due to melting in the low pressure of the vacuum environment [3]. The main constituent of the metallisation layer is aluminium when processing Ti-6Al-4V; since it has a vaporising rate of around two to three magnitudes larger compared to titanium and vanadium [5]. The metallisation layer can be removed while cleaning the vacuum chamber in-between prints and during the machine's service.

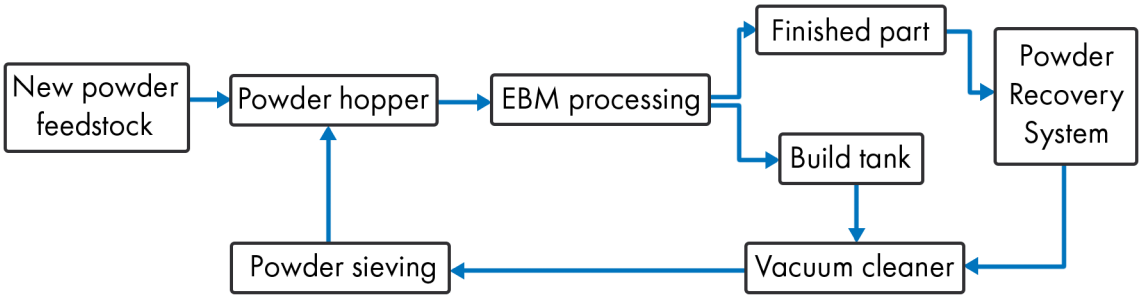

Figure 1.1: EBM powder flowchart

A change in the powder chemistry due to the previously mentioned circumstances will influence the quality and consistency of the process, which is not favourable for a process that requires both. Thus, the scope of this thesis is to devise a method and quantitatively establish the relationship between process atmosphere inside an Arcam EB-PBF (hereafter referred to as EBM) print chamber and the degradation of the powder. The thesis was conducted at the Department of Industrial and Materials Science at Chalmers University of Technology, which is hosting the competence centre for additive manufacturing - metal (CAM^2), in collaboration with Linde Gas AB and Arcam (GE Additive).

1.2 Scope

The main objective was to quantitatively establish the relationship between the powder's chemical composition and the process atmosphere inside an EBM print chamber. This thesis investigates how the atmospheric composition behaves when manufacturing with an Arcam Q20plus system. Oxygen concentration and water content were monitored in-situ in the build chamber and the off gas leaving the chamber, using lambda sensors and a dew point meter. Composition changes were analysed on the process atmosphere using mass spectrometry (MS) and on Ti-6Al-4V powder samples, using X-ray photoelectron spectroscopy (XPS), Inert Gas Fusion Analysis (IGFA), and Scanning Electron Microscopy (SEM).

1.3 Research questions

This thesis' research questions focus on the variation of the oxygen and the water content present in the powder correlated with the process atmosphere.

1. How will the oxygen content in the process atmosphere vary over an EBM build cycle, and how does it affect the oxygen pick-up by the powder?

2. What is the relationship between the data gathered from the oxygen sensors, the dew point meter and the mass spectrometer during processing atmosphere monitoring? What new insights can be found from correlating this information?

1.4 Delimitations

Oxidation state, chemical composition and contaminants were analysed on powder samples and not printed components, the powder material is limited to Ti-6Al-4V.

The printing was conducted using a specific Arcam EBM Q20plus at GE Additive, as to not introduce new machine variations.

Complications due to the ongoing covid-19 pandemic resulted in a postponed installation of the sensors, which resulted in a reduced time frame for measurements from what was initially planned. The measurements started at the beginning of March instead of the end of January like initially intended, limiting the number of trials and hence the extent of the study and statistics.

2

Theory

This chapter highlights and describes relevant theoretical background necessary for description of experiments and discussions in this thesis.

2.1 Powder Bed Fusion

Powder Bed Fusion (PBF) is an additive manufacturing technique that uses a powder stock in combination with an energy system to melt the powder selectively to produce a component. PBF can utilise a wide range of materials such as polymers, ceramics and metals as powder material. A common trait between all PBF-processes is the utilisation of a rake, or a roller, to spread out the powder evenly across the build volume in between layers. The energy systems most commonly associated with PBF are laser-based (LB-PBF) and electron beam (EB-PBF) systems. Laser-based systems are further subdivided into LB-PBF/p and LB-PBF/m, where the suffix designates if it is a polymer or metal used in the process. The EB-PBF process is restricted by the material's electrical conductivity making the technology more suitable for metals, whereas polymers are generally dielectric and not compatible with the technology.

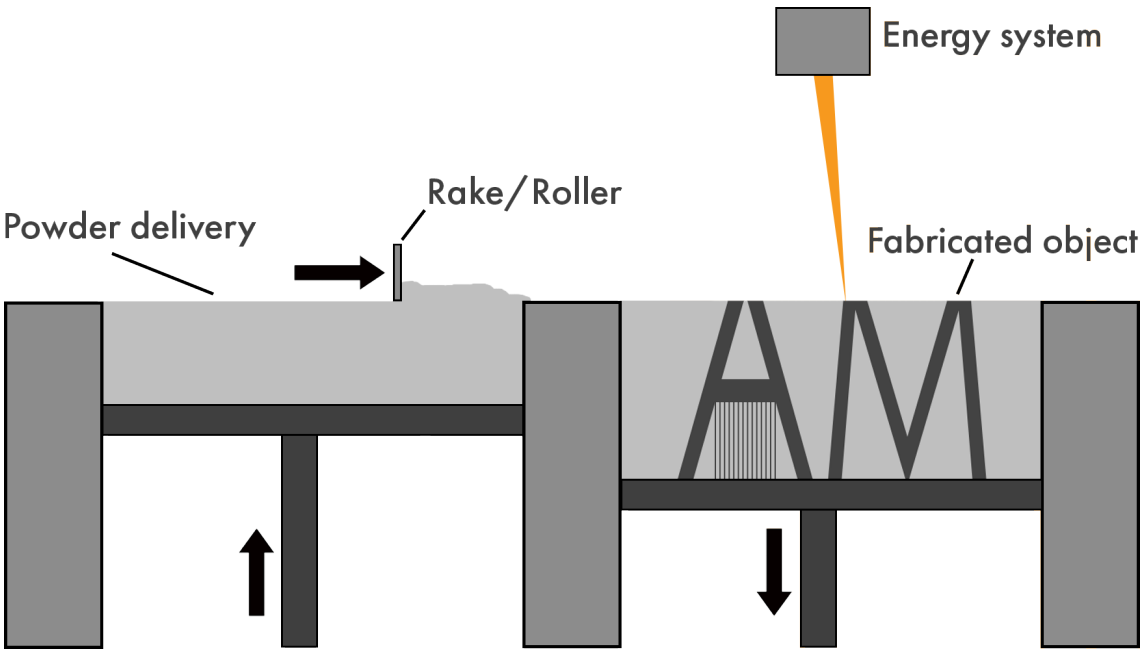

Figure 2.1: Schematic of a generic PBF process. Illustrated by the authors

2.2 Arcam EBM

EBM is an EB-PBF technology patented and developed by Arcam AB since 1993 [6]. The technology is described as melting electrically conductive powder layerwise by an electron beam to produce three-dimensional bodies. EBM is used today for the production of various metal components in the aerospace and medical industry because of the materials available and complex structures possible [7]. Akin to a scanning electron microscope (SEM), the electron beam is generated by a cathode in the form of a tungsten filament or a LaB_6 crystal with an energy range of between 50 W to 6000 W. The generated electrons are accelerated with an energy of 60 keV and collimated with magnetic lenses. Depending on the printed geometry, the beam profile can be customised with regards to power and focus. These three magnetic lenses located in the column correct the possible astigmatism of the electron beam with the first lens, focusing the beam to a spot with a diameter between 0.1 mm to 2 mm with the second lens and deflects the beam around the build area with the third lens [1].

The technology uses a vacuum system designed to minimise the scattering of the generated electron beam while also controlling the reactivity of the process atmosphere by introducing a controlled amount of helium. Helium is mainly supplied to decrease the evaporation of alloying elements. These two aspects become a trade-off since a lower pressure entail less scattering of the beam while also increasing the evaporation rate of the alloying elements from the melt. The low pressure in the system also enables excellent thermal insulation of the build volume. In combination with an atmosphere with low reactivity, these aspects allow the EBM to operate favourably at an elevated temperature during the build phase. The high temperature has several advantages to the final product, such as no residual stresses and material properties that are better than cast and similar to wrought counterparts [8]. The low pressure during the build phase also makes the final component to have excellent susceptibility to Hot Isostatic Pressing (HIP).

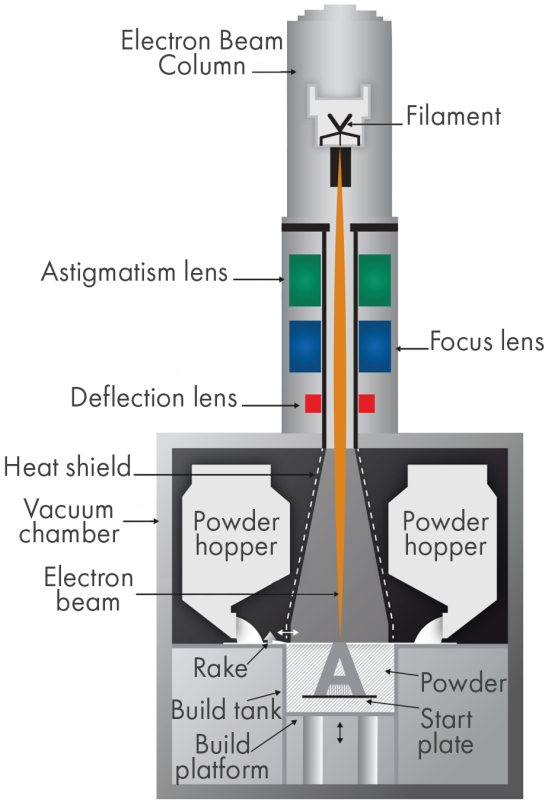

Figure 2.2: The various elements of an EBM [1]. Adapted with permission.

The defining trait of EBM, to use electrons as the energy carrier, brings limitations to

the technology, most prominently that the material must be electrically conductive for the technique to work. On the other hand, it also provides exciting aspects such as an efficient energy delivery to the printed volume, which enables a relatively low energy consumption [9].

2.2.1 Process description

A 3D model of the desired component is imported to a slicer program that interprets and converts the 3D model into a build file consisting of 2D layers (STL) with set parameters that the EBM use to produce the component. The build file contains many parameters in a so-called print theme, which includes, e.g. support structure type, scanning path geometry, energy input and so on. These themes are developed and optimised in-house by Arcam.

Reloading the EBM starts with letting ambient air into the depressurised chamber. The machine is then loaded with powder from a numbered batch of either virgin powder or recycled powder, which can have its usage traced by data logged on previous build cycles. The machine is cleaned before each new print cycle by scraping metallisation from the internal components, removing any excess or spilt powder, and replacing consumables such as the start plate, heat shields, protective foils placed in the column, and the replaceable lead glass on the door. The process is then started, and the vacuum is pumped with two different initial partial pressures of around 10^{-5} mbar in the build chamber and 10^{-7} mbar in the column. When the desired vacuum levels are reached, helium is introduced to the system. The helium is then supplied continuously to maintain and provide a stable, inert atmosphere of around 10^{-3} mbar in the build chamber, 10^{-6} mbar in the column, and help with removing the static charge from the powder.

When the pressure is steady, the start plate is heated by a defocused scanning of the electron beam to a uniform temperature of 600 °C - 750 °C [1]. The preheating temperature depends on the material used in the process. As previously mentioned, the printing process is dependent on what print theme is applied to the build, where the type of support structure and energy input, along with several other parameters, can vary. In general, the print is achieved by first scanning each component's contours present on that layer, followed by hatching, which scans the components' bulk area. The build table is normally lowered between 50 µm and 100 µm for each layer, and a rake supplies a thin layer of powder in between scanning. The powder surrounding the parts is heated to around 80 % of the metals melting temperature. The heating phase of the process slightly sinters the powder by creating necking connections between the particles and also the ground; this helps to reduce the 'smoke' that can occur during the build as the new connections between the particles and the start plate increase the conductivity of the powder and removing the built up charge. If the charge becomes too great, the resulting repulsive force can exceed the frictional and gravitational forces, ejecting the powder into the process atmosphere resulting in the phenomenon referred to as smoke [1].

Another positive aspect of this partial sintering is the increased structural integrity of the surrounding powder bulk, which reduces the number of supports needed for a print relative to other AM technologies and enables components to be built on top of each other in a stacked fashion. The build file needs to have been designed to allow a smooth energy input along the z-axis to ensure an even heat distribution throughout the build.

Once the printing cycle is finished, the system is cooled by supplying helium to the build chamber; note that this is not an obligatory step. As the built volume needs an inert atmosphere while cooling, and the vacuum provides minimal heat dissipation, it could take several days for the volume to cool down if helium was not used. The cooling process utilises a helium pressure of around 0.4 bar as it is a good compromise between cooling rate and gas consumption. Once the temperature is below 80 °C, the operator can open the doors and remove the sintered cake that encapsulates the printed components manually or by removing the entire build tank. The build is then transferred by trolley to the PRS, where the powder is removed for reuse, and the final parts are extracted. The recycled powder captured in the PRS can then be reused in the EBM, creating a near-net-shape manufacturing process.

Figure 2.3: An Arcam EBM Q20plus [10]

Whenever a machine is left for a substantial time, a mode called 'Powder protection' can be used. The powder protection mode works by first pumping a high vacuum to avoid contaminants in the system; a partial pressure of approximately 10^{-3} mbar of helium is then introduced to protect the powder.

2.2.2 Arcam EBM Q20plus

In this thesis, an Arcam EBM Q20plus was used for experimentation. The Q20plus is an EBM model developed and manufactured by GE Additives subsidiary Arcam. The characteristic technical aspects of this particular model are presented below in table 2.1.

Table 2.1: Arcam EBM Q20plus technical data [11].

Max. beam power	3 kW
Max. build volume	350 mm x 380 mm (⌀ x H)
Cathode type	Single crystalline
Min. beam diameter	140 µm
Max. EB translation speed	8000 m/s
Active cooling	Water-cooled heat sink
Min. chamber pressure	5×10^{-4} mBar
Typical build pressure	4×10^{-3} mBar (partial pressure of He)
He consumption, build process	4 l/h
He consumption, ventilation	100 - 150 l/build
Power supply	3 x 400 V, 32 A, 7 kW
Size approx.	2,400 mm x 1,300 mm x 2,945 mm (W x D x H)
Weight	2,900 kg
CAD interface	STL
Available materials	Arcam EBM Ti6Al4V Grade 5
	Arcam EBM Ti6Al4V Grade 23

2.2.3 LogStudio

The software 'LogStudio' is a software developed by Arcam and can be found installed on the terminals of the Arcam EBM printers. It is a software used to measure and log a myriad of parameters related to the printing process and the machine in general. The software has been vital when referencing timestamps to events pertaining to all the different sensors used in this thesis.

2.3 Titanium

The element titanium is a silvery grey refractory metal with a myriad of excellent properties and a wide range of practical applications. Titanium was first isolated into its pure form in 1910 by the metallurgist Matthew Hunter, who through the Hunter process managed to reduce titanium tetrachloride ($TiCL_4$) with sodium (Na) in an airtight cylinder [12]. Often seen alloyed with aluminium and vanadium, the resulting alloy incorporates both remarkable mechanical properties and chemical stability. These properties make it popular in various engineering applications where high performance is vital in a demanding environment. Another valuable aspect of titanium is the inherent biocompatibility of the metal [13].

The powder used in Arcam's process is manufactured by AP&C, another company in the GE group. The manufacturing process used is Advanced Plasma Atomization (APA) which produces a powder with martensitic α'-phase microstructure. The α'-phase is metastable and transforms into the stable two-phase equilibrium state; $\alpha + \beta$, as the powder is used [2]. The β-phase is Al-lean and V-rich and has a higher oxygen content than the lath-shaped α-phase [2].

Table 2.2: Standard specification for the composition of Additive Manufacturing Ti-6Al-4V with Powder Bed Fusion (ASTM F2924-14) [14].

Element	min %	max %
Aluminium	5.50	6.75
Vanadium	3.50	4.50
Iron	-	0.30
Oxygen	-	0.20
Carbon	-	0.08
Nitrogen	-	0.05
Hydrogen	-	0.015
Yttrium	-	0.005
Other elements, each		0.10
Other elements, total		0.40
Titanium	balance	

2.4 Reuse of powder

Improving the reusability of the powder is not only interesting from an economic viewpoint; but also from decreasing the overall consumption of the material, which would enhance the sustainability of the process from both aspects. The alloy investigated in this thesis is relatively energy-intensive to produce from the raw material, with an embodied energy of 655 MJ/kg - 722 MJ/kg [15]. That number is before the powder manufacturing using APA process, which would increase the energy demand even further.

During a print cycle, most of the powder is subject to an elevated temperature that increases the material's reactivity and, in turn, progress the powder's degradation. A powder batch that has been subjected to multiple process cycles will show a variation in the chemical composition compared to a virgin batch. This variation is due to the evaporation of alloying elements and diffusion of elements from the process environment; this can be problematic as the mechanical properties will vary accordingly to the current composition. Some of the alloying elements such as nitrogen, vanadium and iron stay more or less consistent between cycles [16]. In contrast, hydrogen, carbon, oxygen and aluminium has the most noticeable variation between these cycles [16]. The effect on the material properties can be subtle for some elements, but oxygen in particular has a relatively dramatic effect on the alloy; which is reflected in the stringent maximum content of the element according to ASTM standards, see table 2.2. The prominent hardening effect of oxygen in titanium makes it extra essential to have control, or at least attention, to the oxygen content in the final product or mechanical performance is not guaranteed.

2.4.1 Reusing procedure

After a build cycle has been completed, the reloading sequence goes according to figure 1.1. As it can be seen in the figure mentioned in the previous chapter, the

finished component is transferred to the PRS where the printed components are extracted from the sintered volume by blasting a pressurised powder/air mixture through the PRS-handle onto the sintered volume. The blasted powder is recaptured, filtered and collected for sieving.

The recaptured powder from both the vacuum cleaner and the PRS is poured into the powder sieve, seen in figure 2.4. The sieved powder is collected in a batch container for an easy storage solution. After sieving, the powder should not exceed the desired particle size of 105 µm. Now the powder is once again ready to be loaded into the powder hoppers, seen in figure 2.2, and to be used in another print cycle.

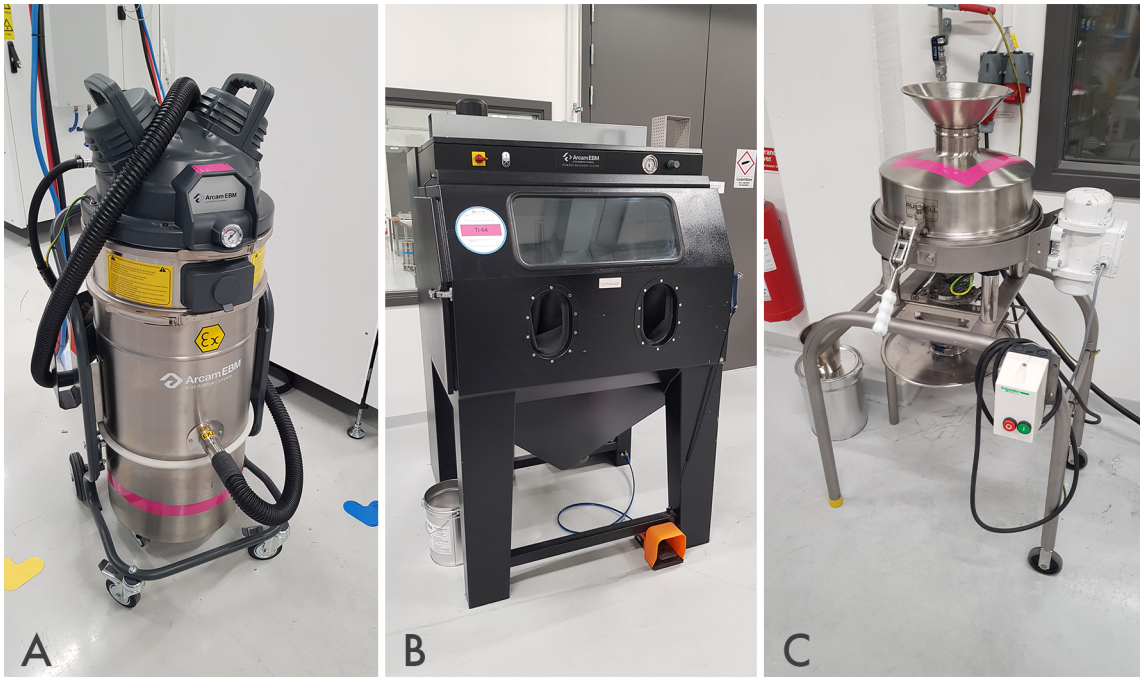

Figure 2.4: Equipment for powder reuse. A) A specialised vacuum cleaner for metal powder. B) A PRS for extracting components from the sintered volume. C) A powder sieve for separating powder with a particle size below the accepted size. Photographed with permission.

2.5 Process atmosphere

The process atmosphere is the gas mixture present in the build chamber during the build phase and it has a strong influence on the outcome of the final product. It is affected by several further addressed factors in the following paragraphs.

2.5.1 Vacuum

The printing process is performed at a high vacuum and elevated temperatures. Both of these aspects help with creating AM components with favourable properties. An EBM operates at a vacuum of about 10^{-3} mbar, producing an optimal result. The vacuum is required because the electron beam would otherwise interact on

an unacceptable level with the atmosphere that would have been present in the EBM, resulting in a component with inaccurate features or no detail at all. Another motivation to use a high vacuum in an EBM is the improved material characteristics with a lack of reactive atmosphere. The use of vacuum is especially beneficial when using reactive metals such as titanium, which reacts particularly noticeably with nitrogen, oxygen and hydrogen. The reactant's partial pressure can be reduced by continuously flushing an inert gas to the present atmosphere. There is both a qualitative and profitable interest in further investigations of these protective gases used in the printing process.

2.5.2 Process gas

The primary choice of process gas today for the EBM process is helium. The reason being that helium has numerous properties that are suitable for the EBM process; properties such as a low effect on the electron beam during printing and high thermal conductivity when cooling the finished build volume. The currently relatively cheap, although steadily rising, price of the gas also influence the choice.

Even though today's commercial gases have exceptionally high purity, some contaminants will always be present at the ppm level. For commercially available helium, the most prominent contaminants in descending order are oxygen [O_2], water vapour [H_2O] and various hydrocarbons [C_nH_m], see table 2.3. The helium grade currently in use by Arcam is helium 4.6.

Table 2.3: Specification of helium 4.6 manufactured by Linde Gas AB and used in the build process at GE Additive.

Helium 4.6 - Linde Gas AB

Element/Compound	**min, ppm**	**max, ppm**
Oxygen, O_2	-	5
Water, H_2O	-	5
Hydrocarbons, C_nH_m	-	1
Helium, He	Balance	

2.5.3 Partial pressures

The total pressure of a mixture of gases can be defined as the sum of the mixture's constituent gases' partial pressures from x to n according to Dalton's Law (2.1).

$$P_{total} = P_x + P_{x+1}...P_{n-1} + P_n \tag{2.1}$$

Although this relationship is valid for ideal gases when the gas mixture is at low pressure and high temperature, as they could be considered in the EBM process, a more elaborate calculation might be needed to give an accurate answer for scenarios where the conditions are not ideal [17].

2.5.4 Off-gas

The gas mixture exiting the Arcam EBM system is referred to as the off-gas. The off-gas exits the rough pump and evacuates into the surrounding atmosphere outside the machine. As the off-gas contains mainly helium and normal atmospheric constituents in minimal quantities, no special precautions are needed when handling the gas.

2.5.5 Water vapour

The humidity present in the print chamber is problematic because it can be dissociated in the energetic environment of the EBM into its constituent elements, namely oxygen or hydroxyl groups, through interactions with the electron beam and the heated powder. These constituent elements interact chemically with the Ti64 powder stock, which is undesirable in a controlled process such as AM. The primary source of humidity in the process is coming from the ambient atmosphere, which adsorbs on the surface of the powder and the metallisation present in the build chamber when exposed to it. Some metallisation will collect on the internal parts in the build chamber, whilst most metallisation is caught by the heat shields during the process, which are replaced in between build cycles.

2.6 In-situ measurements

This section describes techniques used to measure atmospheric composition in-situ in the process. These include oxygen sensors measuring both in the build chamber and the off-gas, a dew-point meter and flow-meter measuring on the off-gas, and the mass-spectrometer placed in the column of the EBU.

2.6.1 Oxygen sensors

Two separate oxygen sensors, more often referred to as lambda sensors, were used in-situ to measure the oxygen contents of the process atmosphere. Both sensors consist of two chemically inert and electrically conducting electrodes connected by a zirconia electrolyte. The device measures the electromotive forces (EMF), and uses the difference in potential between the sampled atmosphere and a reference gas (air). The difference in EMF is then used to calculate the oxygen concentration through the Nernst equation [18]:

$$E_{EMF} = \frac{RT}{4F} ln(\frac{pO_2}{pO_2'}) \tag{2.2}$$

Where E_{EMF} is the electromotive force (mV), R the gas constant, T is the measured Nernst temperature (Kelvin), n is the number of charges per reactant species, F is the Faraday constant, pO_2 is the sample gas oxygen partial pressure (mole fraction), and pO_2' is the reference gas oxygen partial pressure (mole fraction).

The sensors gathered data continuously throughout the printing with a T90 of 5 seconds with a gradual decrease from 20.9 % O_2 to 1,000 ppm O_2 and 10 seconds for T90 from 1,000 to 10 ppm [18].

The POA is designed for extractive measurements on a gas flow, and is fitted with a pump, a flowmeter, and a signal processing device. The POA is calibrated to a flow around $1.2\,\mathrm{l\,min^{-1}}$ to work accurately [18]. The POA is used to measure the in-situ oxygen content of the off-gas leaving the EBM print chamber.

The vacuum adapted oxygen sensor, designated VAC, is a lambda sensor for high vacuum operation. The VAC differs from the POA by operating only through diffusion from the ambient process atmosphere into the heated zirconia-electrolyte sensor head. The sensor head operates at an elevated temperature around 700 °C where the diffusion of oxygen through the electrolyte is effective [18]. The sensor head operates without extracting gas, unlike the POA. The VAC was used to measure the EBM print chamber's process atmosphere.

2.6.2 Dew point meter - Vaisala DMP248

A Vaisala DMP248 sensor was used to measure the water content in the off-gas in terms of dew point expressed in degree Celsius: °C. A value conversion to volume-based ppm was conducted on each print cycle data-set. The conversion was achieved through a converter from Panametrics supplied to the authors by Linde Gas AB, which uses tabulated values to extrapolate the water content. The dew point meter's accuracy depends on the process temperature, which determines its effective range. As the dew point meter is measuring on the off-gas of the process at around room temperature, the higher limit is around 20.06 °C or 11, 650 ppm [19].

2.6.3 Mass Flow Meter - CS Instruments VA 520

A VA 520 mass flow meter from CS Instruments was used to measure the flow in the off-gas exiting the machine. It was of interest to measure the mass flow in the off-gas as it would indicate if the flow was at the required level for the POA.

2.6.4 Mass spectrometry

Mass spectrometry is a analysis technique that measures the mass-to-charge ratio present in a chemical sample. This analysis is achieved by ionising the atomic particles from the sample with numerous, high-energy electrons. These ionised particles are later accelerated and deflected through a magnetic field which, according to their masses, deflects the lighter particles more than heavier ones. The deflection also depends on the number of positive charges on the ions; a higher charge also correlates with a higher deflection. As the ions arrive at the detector, the particle's charge is neutralised by the detector, and the resulting current from the impinging ions is measured. This signal can then be interpreted into the abundance of ions measured in the system.

2.7 Inert Gas Fusion Analysis

Oxygen and nitrogen were measured on powder samples through IGFA using a LECO ON736. According to [20], a sample is heated in a furnace in a graphite crucible, where it reacts and forms compounds with carbon, oxygen forms CO and CO_2. The fused gas is then swept by an inert gas through a heated reagent where it oxidizes, where oxygen forms CO_2 and H forms H_2O. The oxygen content is measured from the amount of CO_2. Nitrogen is measured on the remaining gas after CO_2 and H_2O are evaluated.

2.8 X-ray photoelectron spectroscopy

According to [21], XPS is a surface-sensitive technique used to investigate and analyse the chemical composition of the outermost atomic layers of materials. By irradiating the surface with X-rays, photoelectrons are released with material-specific kinetic energy. A spectrum of detected electrons per energy interval is acquired where each element has a unique spectrum. The relative composition of mixed elements is approximated by a sum of the spectrum's individual intensities. XPS can also provide information on the surface's chemical state by measuring exact peak positions and peak separations. The ability to investigate the outermost layers of the material is interesting for an oxidation-prone material like Ti-6Al-4V.

2.9 Scanning Electron Microscopy

As the name implies, a scanning electron microscope (SEM) uses a focused electron beam to scan a surface to generate an image. The electrons are scanned in a rasterised pattern and interact in various ways with the scanned surface, generating secondary electrons, backscattered electrons, and characteristic X-rays. All of these signals contain different types of information of the samples, which depending on the operator's interest, can image different aspects of the sample.

The SEM present at Chalmers is an LEO Ultra 55, used primarily for high-resolution imaging of conducting samples [22]. The same microscopy is also capable of EDX, EBSD and STEM, but as these techniques are not utilised in this thesis, they will not be discussed further.

3
Method

This chapter explains the methods and experimental setup, as well as use of various equipment used in the analysis and also the methods behind the analyses.

3.1 Installation of instruments provided by Linde Gas AB

The sensors were installed according to the diagram in figure 3.1 and are indicated as VAC, DP and POA in the diagram. The vacuum adapted oxygen sensor, designated VAC, was attached to the print chamber through an inlet valve. The dew point meter and the oxygen sensor, designated POA, are connected in series after the roughing pump, seen in figure 3.1. A technician from Linde Gas AB installed both oxygen sensors and the dew point meter. All of the sensors were connected to an external control box that translates the mV signal to logged values. These values were in turn logged with a laptop supplied by Linde Gas AB using the software 'Easyview'.

Close to the print chamber outlet, a dew point meter was installed to measure the H_2O contents in the off-gas leaving the print chamber. A predicted risk was that the moisture from the process atmosphere would not reach the sensor by having it condense on the way, which would result in unreliable data. The dew point meter was installed early in the outlet chain to minimise this risk. It was of interest to analyse the H_2O contents of the process atmosphere as previous internal research at Arcam AB has found a correlation between the powder's moisture level and the resulting oxygen content in the recycled powder.

3.2 Installation of mass spectrometer

The MS became available for use starting with the seventh build cycle. It was installed in the EBU, see figure 3.1, near the cathode with a T-coupling to orient the equipment so it would fit inside the confines of the upper compartment with closed doors. The ion trap that was initially at the install location was moved to a nearby location in the EBU; the reason was that the specific install port was the only one suitable for the MS orientation wise.

The MS was connected to a laptop with an ethernet cable. The data were logged using the software PVMassSpec from Pfeiffer Vacuum.

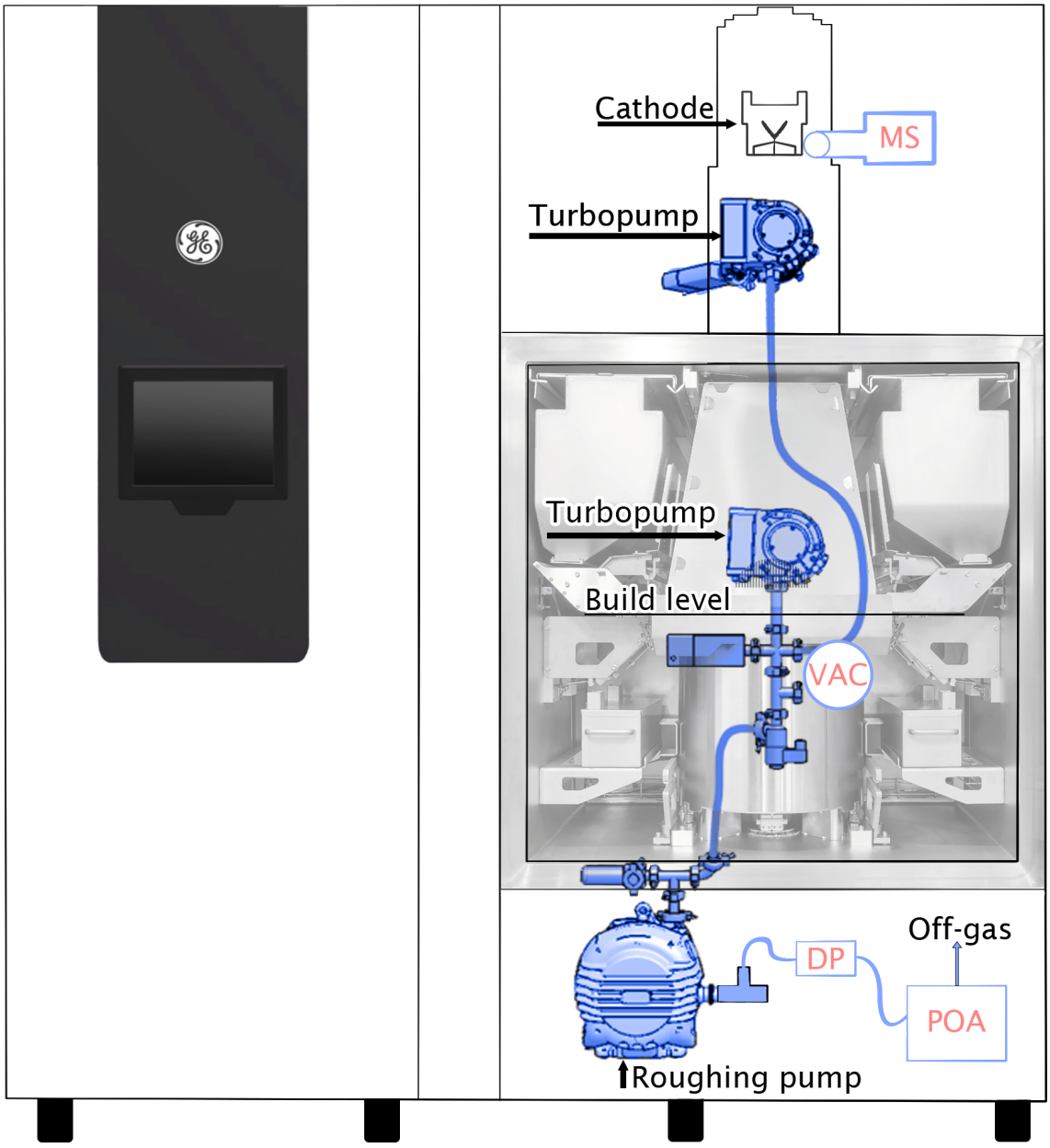

Figure 3.1: Diagram of an Arcam Q20plus without the chamber door and the approximate installation locations of the various sensors installed on the back side. Blue components indicate that they are in contact with the process gas. Illustrated by the authors, containing elements from official GE Additive literature [8][23].

3.3 Operating the Q20plus

The authors attended an operator's course for the EBM in early February. The process was then run with increasing autonomy by the authors under the supervision of Arcam personnel to gain a deeper understanding of the process. A substantial

amount of time was invested in preparing builds, resetting the machine before the restart and handling the post-processing steps required to restart the EBM.

3.4 Powder used for experiments

The powder used in the experiments was a Ti-6Al-4V powder batch with an unknown reuse history and exposure to atmospheric air. As a batch with virgin powder was not available for use in this experiment, a recycled batch had to be used. Since the change in oxygen concentration in the powder was of interest, a baseline had to be established by investigating the oxygen content in the powder. This was done by running IGFA analysis with an increased sample frequency before using the powder and for the subsequent two build cycles.

3.5 Powder sampling strategy

Powder samples were collected from the sintered powder throughout all printing cycles when possible and deemed necessary. An elaborate sampling strategy, shown in figure 3.2, throughout the build volume was applied throughout all build cycles. The numbered samples were then taken at build heights correlating with seven-hour intervals of print time; the reason to divide the samples into this interval was to achieve a high sampling frequency but with a reasonable amount of total samplings for later spectroscopy analysis. Before and after each printing cycle, a reference sample of the powder was collected; this was done to establish the bulk powder's current chemical composition.

The general sampling method applied can be seen in figure 3.2. All numbered samples are taken close to the manufactured part, where the powder is exposed to the highest temperature and a at the same time contact to the outside atmosphere, especially during cooling, is limited. The B samples were collected on the sifted powder before initiating each print cycle. The A samples were collected in the bulk of the sintered cake after printing. The numbered samples were extracted manually from the sintered powder cake with a stainless steel tool before the standard PRS procedure. The samples gathered were analysed in the various spectroscopy techniques explained upon further reading. The red ellipses indicated in figure 3.2, highlight the sampling locations from x to n, with

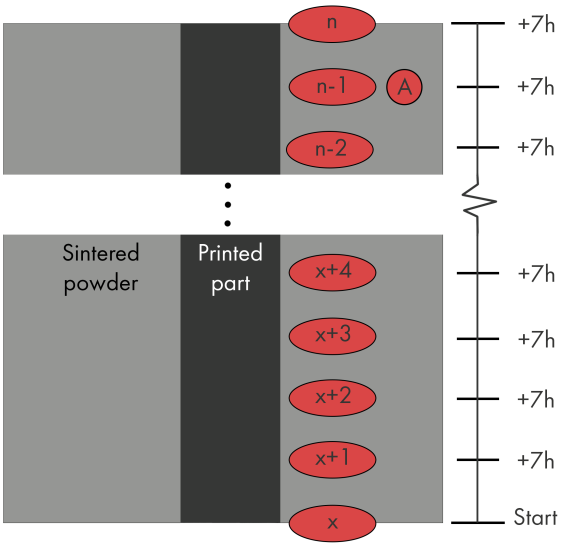

Figure 3.2: The figure above illustrates sampling method applied. Sample B, not present in the figure, is sampled from the sieved powder before each cycle.

a relative sampling frequency correlating with every 7th hour. The numerical designations were used to identify the samples during the analysis.

The Q20plus used in this thesis was shared in another project conducted by Arcam operators, which resulted in varying build sizes. Hence, all sampled prints are of alternating height and build duration. Although the print size varies, the authors strived to include a standardised geometry in every build in the form of cylinders spanning the build volume height at the same relative location; to have a greater consistency when sampling the powder.

3.5.1 Reloading of powder

As the machine was shared between the authors and Arcam operators, certain considerations had to be made to limit the chance of a failed build cycle. One consideration was to have an ample amount of powder in the hoppers, so the build cycle would not fail because of a powder shortage. This consideration resulted in a lower ratio of powder exposed to the electron beam for each build cycle, demonstrated in figure 3.3, compared to if a limited amount of powder was to be used.

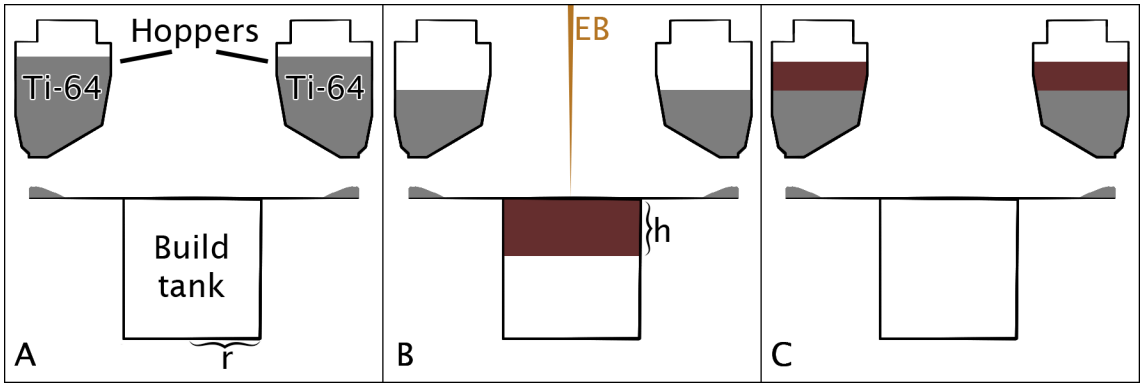

Figure 3.3: A diagram of the general powder mixing after a completed build cycle. The grey powder represents "fresh powder", while the maroon powder represents powder that has been exposed to the electron beam (EB). (A) represents the initial condition, (B) represents the exposure of the powder to the electron beam, and (C) represents the mixing of the recovered powder.

The average build height for the build cycles in this thesis is around 150 mm, as can be seen in table 3.1. The diameter of the build volume is 350 mm. The average volume of powder per build cycle can therefore be deduced from the following calculation:

$$\begin{aligned} V &= \pi r^2 h \\ &= 0.01443\ m^3 \end{aligned} \tag{3.1}$$

The average mass of powder used per build cycle becomes:

$$\begin{aligned} m &= V * \rho \\ &= 0.01443 * 2470 \\ &= 35.64\ kg \end{aligned} \tag{3.2}$$

Where ρ is the density of Ti-64Al-4V powder with the specified particle size [24]. The total mass of the powder before the first build was approximately 120 kg. This means approximately 30 % of the total powder is used per build cycle, leaving 70 % in the hoppers. This value is an average to serve as a simple demonstration of how much powder is exposed to an elevated temperature and does not represent the actual powder usage for each build cycle.

3.6 Progressive changes in method

As experiments were conducted, certain limitations were found, and improvements to the method were realised. These realisations led to changes to the continued experimentation.

3.6.1 Changes in method from B3 onwards

The need to implement a standardised volume to collect samples was discussed and implemented. A row of cylindrical test bars spanning the entire height of the build volume was used in subsequent prints as the sampled print volume.

A discrepancy in the internal time between the Arcam Q20plus and the logging computer supplied by Linde Gas was found. This inconsistency led to differing timestamps of the data logged between the computers. As both computers could not be synced to an external service from their operating system, the internal clocks were corrected by manually syncing the time to an external device with a clock using the correct time. During logging, Daylight Saving Time (DST) shifted the time one hour forwards from 02:00 AM to 03:00 AM during the night between March 27 and March 28. This shift only led to a gap in the data during that missing hour, but no data points were lost.

3.6.2 Changes in method from B6 onwards

A mass spectrometer was installed to complement the analysis. The EBM machine was calibrated to compensate for the beam interference caused by the MS installed near the EBU. The process cycle is changed not to cool the build with helium after a print; this was done to avoid damaging the MS as it needs to be turned off before helium is introduced at higher pressures.

Because of the recent failures to start, a minor maintenance was conducted. This maintenance included changing components such as cathode, anode, drift tube and other consumables.

3.7 Print cycle information

As previously explained, various build files were used in this analysis, and the individual builds differ in building time and building height. In some instances, it was not possible to collect specific samples, such as the B and A samples, because of surrounding circumstances. A detailed description of what is included for each build can be seen in table 3.1.

Table 3.1: Information about the various print cycles conducted and their associated analysis methods.

Build nr.	1	Build nr.	2	Build nr.	3
Build time	37h 25m 18s	Build time	50h 7m 42s	Build time	72h 27m 20s
Build date	21-03-09	Build date	21-03-17	Build date	21-03-25
Build height	117 mm	Build height	106 mm	Build height	183 mm
Samplings	6	Samplings	8	Samplings	11
B sample	Yes	B sample	Yes	B sample	Yes
A sample	Yes	A sample	Yes	A sample	Yes
MS	No	MS	No	MS	No
SEM	Yes (B1-B&A)	SEM	No	SEM	No
XPS	Yes (B1-B)	XPS	No	XPS	No
IGFA	Yes	IGFA	Yes	IGFA	Yes
DP	Yes	DP	Yes	DP	Yes
VAC/POA	Yes	VAC/POA	Yes	VAC/POA	Yes
Build nr.	4	Build nr.	5	Build nr.	6
Build time	Failure to start	Build time	Failure to start	Build time	35h 25m 18s
Build date	21-03-31	Build date	21-04-01	Build date	21-04-06
Build height	0 mm	Build height	0 mm	Build height	102 mm
Samplings	0	Samplings	0	Samplings	6
B sample	No	B sample	No	B sample	No
A sample	No	A sample	Yes	A sample	Yes
MS	No	MS	No	MS	No
SEM	No	SEM	No	SEM	No
XPS	No	XPS	No	XPS	No
IGFA	No	IGFA	No	IGFA	Yes
DP	No	DP	No	DP	Yes
VAC/POA	No	VAC/POA	No	VAC/POA	Yes
Build nr.	7	Build nr.	8	Build nr.	9
Build time	57h 42m 50s	Build time	49h 58m 58s	Build time	73h 46m 16s
Build date	21-04-16	Build date	21-04-20	Build date	21-04-23
Build height	180 mm	Build height	106 mm	Build height	239 mm
Samplings	9	Samplings	8	Samplings	11
B sample	Yes	B sample	Yes	B sample	Yes
A sample	Yes	A sample	Yes	A sample	Yes
MS	Yes	MS	No	MS	No
SEM	No	SEM	No	SEM	No
XPS	Yes (B7-B)	XPS	No	XPS	No
IGFA	Yes	IGFA	No	IGFA	No
DP	Yes	DP	Yes	DP	Yes
VAC/POA	Yes	VAC/POA	Yes	VAC/POA	Yes
Build nr.	10	Build nr.	11		
Build time	45h 43m 25s	Build time	60h 48m 56s		
Build date	21-04-28	Build date	21-05-06		
Build height	180 mm	Build height	130 mm		
Samplings	7	Samplings	8		
B sample	Yes	B sample	Yes		
A sample	Yes	A sample	Yes		
MS	No	MS	No		
SEM	Yes (B10-A)	SEM	No		
XPS	No	XPS	No		
IGFA	No	IGFA	No		
DP	Yes	DP	Yes		
VAC/POA	Yes	VAC/POA	Yes		

3.8 Air-helium mixture model

To gain insight into how the helium mixes in the process atmosphere, a formula consisting of an ordinary differential equation (ODE) was employed to solve this mixing problem theoretically.

The ODE represents an ideal scenario where no contaminants are present in the helium and no leaks from the outside atmosphere are taking place. It was used to give a lower boundary for the mixture model. As shown in table 3.2 below, the volume flow in and out is the same; the rationalisation behind this is that the logged pressure values from the EBM show a constant pressure of 6.9×10^{-3} mbar with an approximate helium supply of $0.125\,\mathrm{l\,min^{-1}}$ during the build phase (Technician at GE Additive, personal communication, May 28, 2021), this reveals that the same volume of gas entering the EBM must also leave as off-gas.

The concentration rates in this model have the unit moles per minute, moles $\mathrm{min^{-1}}$, as it was a convenient unit to use with regards to what information was available concerning the process. The mixing problem can be described as follows:

- The volume of the build chamber containing the process gas is approximated to 600 l.
- The initial air pressure before helium is introduced to the build chamber during the build phase, was measured to be 1.1954×10^{-4} mbar or 1.1954×10^{-2} Pa.
- Helium enters the chamber at $0.125\,\mathrm{l\,min^{-1}}$.
- As the pressure stays the same during the build process, the same volume of gas exits the chamber as off-gas.

Some assumptions have been made to decrease the complexity of the model.

- The amount of moles of air at y(0) is calculated with the ideal gas law, which is reasonable as SATP conditions are met before pumping a vacuum, and the conditions can still be considered ideal at lower pressures [25].
- The ratio of air entering the system through the gas supply is set to zero. The reasoning behind this is that the purity of the helium 4.6 entering the system, together with the low rate at which the gas is supplied, makes the effect from the air negligible.

Table 3.2: Concentration and volume flow rate for air dilution with helium.

In	Concentration air in, n/l	C_{in}	0
	Rate in, l/min	R_{in}	0.125
Out	Concentration out, n/l	C_{out}	$y(t)/600$
	Rate out, l/min	R_{out}	0.125

In these calculations, the unknown to be solved for is the air-He concentration exiting the build chamber, y(t), and how it affects the composition of the process atmosphere over time. A standard mixing formula, eq. 3.3, is used as a basis for this model.

$$\frac{dy}{dt} = (C_{in} * R_{in}) - (C_{out} * R_{out}) \tag{3.3}$$

The values from table 3.2 are inserted into eq. 3.4 and eq. 3.5.

$$C_{in} * R_{in} = (0)(0.125)(\frac{n}{l})(\frac{l}{min}) \tag{3.4}$$

$$C_{out} * R_{out} = (\frac{y(t)}{600})(0.125)(\frac{n}{l})(\frac{l}{min}) \tag{3.5}$$

Eq. 3.4 and 3.5 are inserted into equation 3.3.

$$\begin{aligned} \frac{dy}{dt} &= 0 - y(t)(\frac{0.125}{600}) \\ &= -y(t)(2.083 * 10^{-4}) \end{aligned} \tag{3.6}$$

Equation 3.6 is a separable differential equation which can after integration provide exact answers at designated times, y(t).

$$y(t) = Ce^{-2.083*10^{-4}\,t} \tag{3.7}$$

Solving for the constant C, an initial boundary condition representing the value for the amount of air present at $t = 0$ is required. By using the ideal gas law and solving for the amount of moles present in the system before helium is supplied, see equation 3.8 below, the air content in the build chamber can be estimated.

$$\begin{aligned} n &= \frac{P\,V}{R\,T}\,(\frac{Pa\,m^3}{m^3\,Pa\,K^{-1}\,mol^{-1}\,K}) \\ &= \frac{0.011954 * 0.6}{8.3145 * 293.15} \\ &= 2.94265 * 10^{-6} \end{aligned} \tag{3.8}$$

The calculated value in eq. 3.8 is used to set the initial boundary condition and calculate the constant C.

$$\begin{aligned} y(0) &= 2.94265 * 10^{-6} = C * 1 \\ &= 2.94265 * 10^{-6} = C \end{aligned} \tag{3.9}$$

The final expression for the formula describing the dilution of atmospheric air in the build chamber of the EBM with helium.

$$y(t) = 2.94265 * 10^{-6}\,e^{-2.083*10^{-4}\,t} \tag{3.10}$$

3.9 Analysis

XPS was applied to analyse the chemical composition and oxide layer thickness present on the powder at different stages. A PHI 5000 VersaProbe III Scanning XPS Microprobe located at Chalmers University of Technology was used with a

trained operator's help.

XPS analysis was carried out on the B samples of build 1 (B1) and build 7 (B7). As presented in the results, an analysis between B1 and B7 was deemed sufficient after reviewing the results. Why B7 was chosen to be analysed and not a later sample was because B7 was at the time the latest build that had an IGFA conducted, which would let the results from the XPS complement the ones from the IGFA.

As it was powder samples that were to be analysed in the XPS, the sample was mounted onto a carbon tape, and the excess powder was removed from the mounting plate with nitrogen gas.

Firstly, survey spectra of the powder surface were acquired to gain an overview of the chemical composition. A photoelectron intensity versus binding energy up to 1100 eV was acquired for all samples and then compared. In the spectra, either the metal peaks or the oxide peaks can be used to analyse the chemical transition; in this case, the oxide peaks were used as they were deemed the most suitable to quantify with a smaller chance of interference from other peaks. The peaks of interest in this survey are presented in the results.

The etch depth of the XPS was calibrated with tantalum oxide; this calibration makes it possible to translate the etch time in minutes to a depth profile in nm for the chemical analysis. To evaluate an oxide layer thickness from the depth profile, the oxide peak (O1s) maximum intensity is measured against its minimum value after prolonged etching and oxide layer thickness is found based on the half between the maximum and minimum intensities (XPS operator at Chalmers, personal communication, June 2, 2021). This value is then multiplied with the calibrated etch depth of 5.2 nm $\text{min}^{-}1$, which in turn gives the total oxide thickness in nm [26]. The validity of this value can also be correlated with the ratio of the intensity between the metallic and oxide peak of titanium in dependence on the etch depth [26].
Both oxygen sensors, designated POA and VAC, were calibrated at Linde Gas' facilities prior to the testing period. The data were logged with a laptop using the software 'EasyView' and later exported as textfiles and analysed using Excel and MATLAB. As the sensors had a sampling rate of 5 seconds, the resulting data files became large. MATLAB was used to analyse the data and plot the graphs.

The data points represented as a mV signal, were translated to a ppm value with Nernst equation and the measured Nernst temperature, T for each specific oxygen sensor. The Nernst temperatures for the VAC and POA were measured to 645.8 °C and 762.2 °C respectively. The conversion from electromotive force E_{EMF} to partial pressure pO_2, was conducted through the simplified Nernst equation [27]:

$$pO_2 = 0.2095e^{-46.421E_{EMF}/T} \tag{3.11}$$

IGFA was utilised to analyse the bulk powder's composition, focusing specifically on oxygen. A LECO ON736 located at GE Additive was used for this analysis; an operator at the facilities conducted the analysis of the powder. This instrument was

used because of its relatively fast data acquisition and availability at the testing location. Every sample analysed with LECO was analysed three times to establish the results' standard deviation. Even though it was not of primary interest, nitrogen levels in the bulk materials were also analysed and are presented with oxygen levels later in the results. The data was compiled afterwards using Excel.

Mass Spectrometry (MS) was utilised to measure the general composition of the process atmosphere, detect contaminants, and analyse the oxygen content. The mass spectrometer used is a PrismaPro QMG 250 F2 manufactured by Pfeiffer Vacuum and was installed in the EBU, see figure 3.1, by the authors and technicians at GE Additive. The software used to analyse the MS data is distributed by Pfeiffer Vacuum as 'PV MassSpec'.

SEM was utilised to analyse the morphology of the powder samples, mainly to visually compare the change in powder shape and surface morphology, if any. Secondarily, to compare the geometry of the powder with regards to shape and size between build cycles. A small sample of B1-A, B1-B and B10-A were inspected, and images of the powder particles were saved; some of these images for B1-A and B10-A can be seen in figure 4.10.

4
Results

In this section, the experimental results from the process atmosphere and the powder analyses are presented.

4.1 In-situ measurements

This section presents the results from all techniques that measure in-situ in the process. These include the oxygen sensors measuring in the build chamber and the off-gas, a dew-point meter and flow-meter measuring on the off-gas, and the mass-spectrometer placed in the column of the EBU.

4.1.1 Mass flow meter

After using the flow meter, it was determined that the flow was too low to give an accurate measurement with this instrument. The theorised amount of off-gas exiting the system is approximately $0.125\,\mathrm{l\,min^{-1}}$, which was below the measurement limit of the instrument. As the measurements were unsuccessful, the data from the measurements were not used to draw any conclusion regarding the flow of the exiting off-gas.

4.1.2 Oxygen sensors and dew point meter

The VAC showed an oxygen concentration with a stable value around 0.02 ppm - 0.04 ppm throughout the build cycles, see figure 4.1. Converted into partial pressure this is between $1.4 \times 10^{-7}\,\mathrm{mbar}$ and $2.8 \times 10^{-7}\,\mathrm{mbar}$. Since the graphs for the successive builds follow similar characteristics, the plots for B2 - B11 are placed in appendix B.

The data collected from the POA indicates an oxygen concentration of around $10 \times 10^{-13}\,\mathrm{ppm}$ is maintained throughout the build cycles, as seen in figures B.10a - B.18a in appendix B. This value is unreasonably low and does not correlate with the VAC sensor and the MS data. The POA likely failed due to insufficient flow and an under-pressure present at the sensor. The possible reasons behind the failure are explored in the discussion.

The DP sensor displayed a pretty consistent behaviour of the moisture content between the builds. In general, an initial moisture level saw an increase to levels beyond the sensor's capabilities as helium, and the preheat cycle started. As the

moisture content went below readable levels, shown as the 'dip' at 13:00 in fig 4.1a, a steady and continuous decrease of the moisture content followed. The moisture levels did not converge to a specific value during any analysed build cycles.

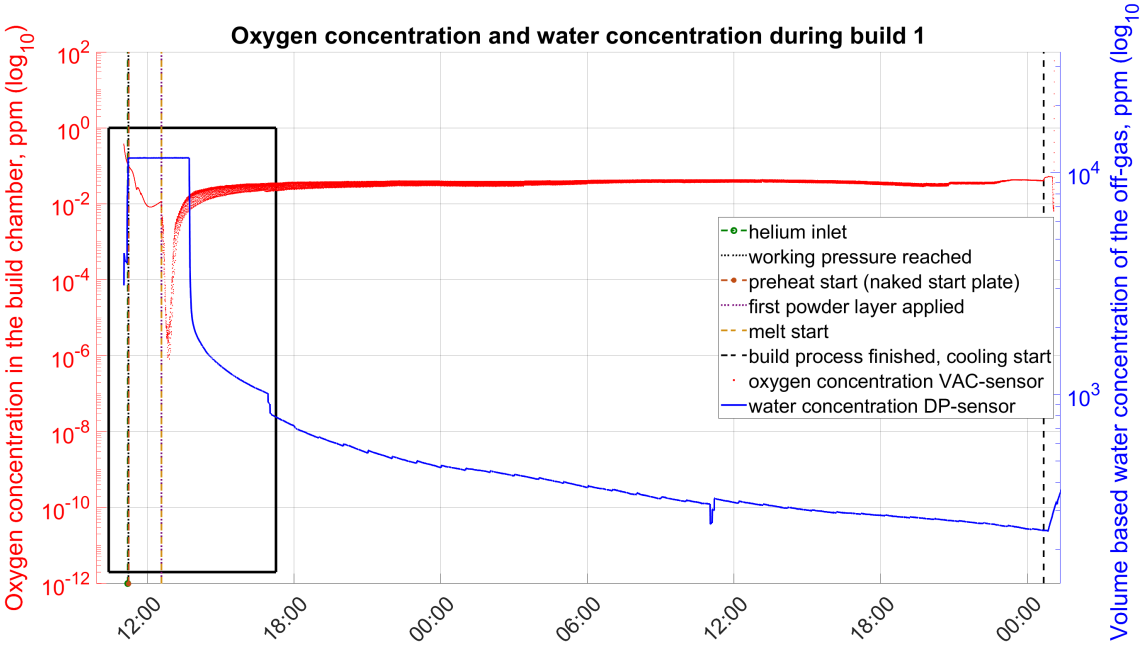

(a) The oxygen concentration in the build chamber (VAC) plotted on the primary axis, and water concentration of the off-gas plotted on the secondary axis. The preheat, start and stop times are correlated from the log files collected by the internal EBM software.

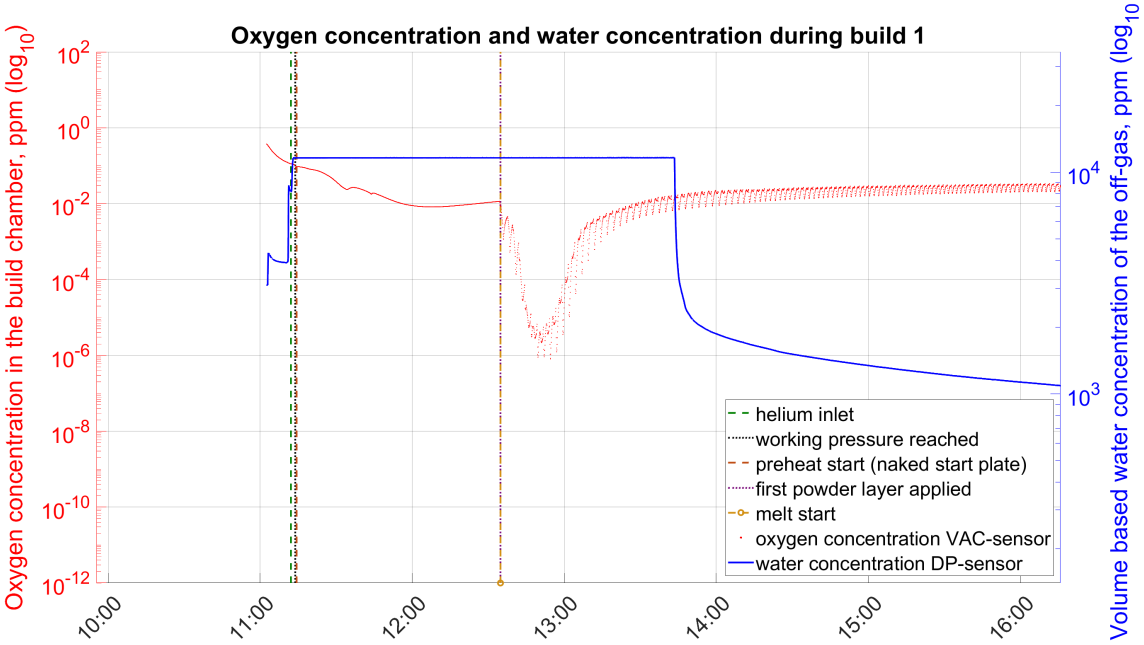

(b) An enlarged view of a characteristic oxygen spike measured by the VAC sensor in the build chamber during a build start.

Figure 4.1

4.1.3 Air-Helium mixture model

The dilution model proposes that the system has a quite slow dilution of air which translates into a relatively stable oxygen concentration over time. In figure 4.2 below, the theoretical dilution over 100 hours is represented.

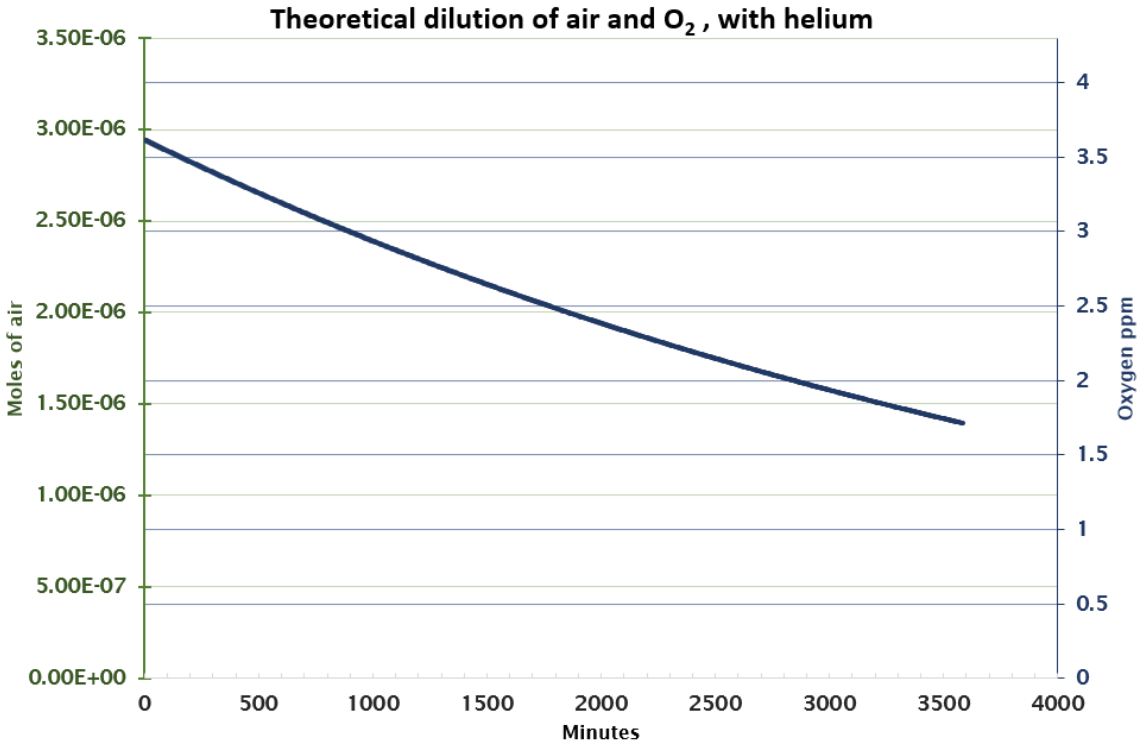

Figure 4.2: A diagram of the theoretical dilution of the assumed levels of air and oxygen in the system, based on the air-helium mixture model. The same curve represents both a theoretical value for the number of moles of air and ppm of oxygen present.

4.2 Mass-spectrometry

As the MS was mounted near the EBU and not the build chamber, the results gathered from this instrument may not show an exact representation of the constituents found in the build chamber. As the build chamber and EBU does share the same process atmosphere, the results should illustrate a fairly similar composition.

The MS acquired one successful measurement for build B7. Three more attempts to collect data were performed for the subsequent builds, which failed due to technical errors with the logging computer. A summary of the results is presented here but are discussed more in detail in the discussion.

The ratio of nitrogen to oxygen in the system could indicate a minor air leak. The air in the system could be entering through the seals, alternatively from the supplied helium. The reasoning leading to identifying the 28 amu signal as the N_2 signal is further pursued in the discussion.

The H_2 peak increase as preheating begins, as can be seen in figure 4.4, and achieve its maximum value after the melting has started. This increase leads to a relative decrease in H_2O, N_2, O_2 and OH.

The system's moisture content is gradually reduced during a process cycle.

Table 4.1: The signals seen in the MS and what elements or compounds that they are derived to represent.

Mass Spectrometry signals						
amu	2	4	17	18	28	32
Proposed dominant compound / Element	H_2	He	OH	H_20	N_2	O_2

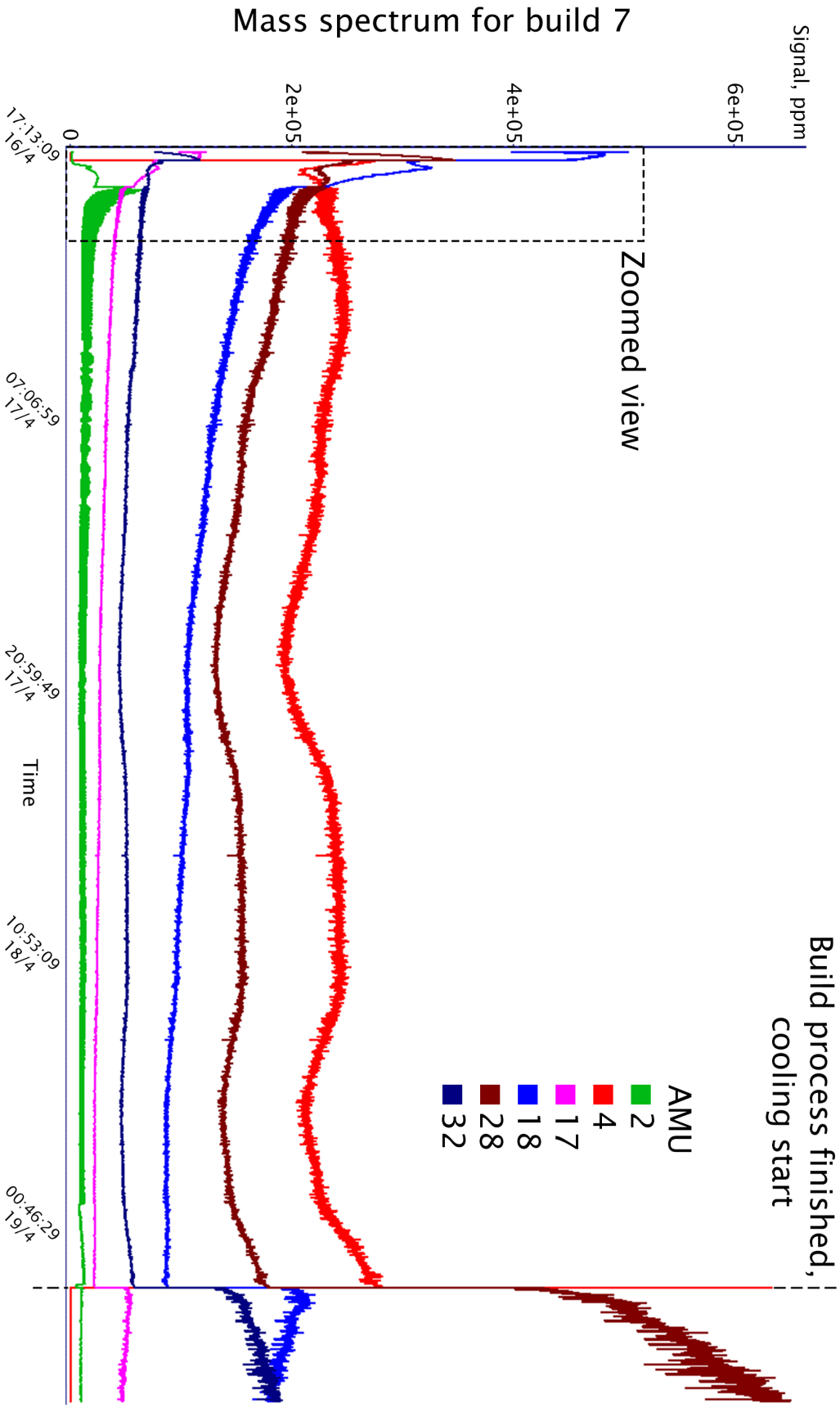

Figure 4.3: View of the mass spectrometry for build 7.

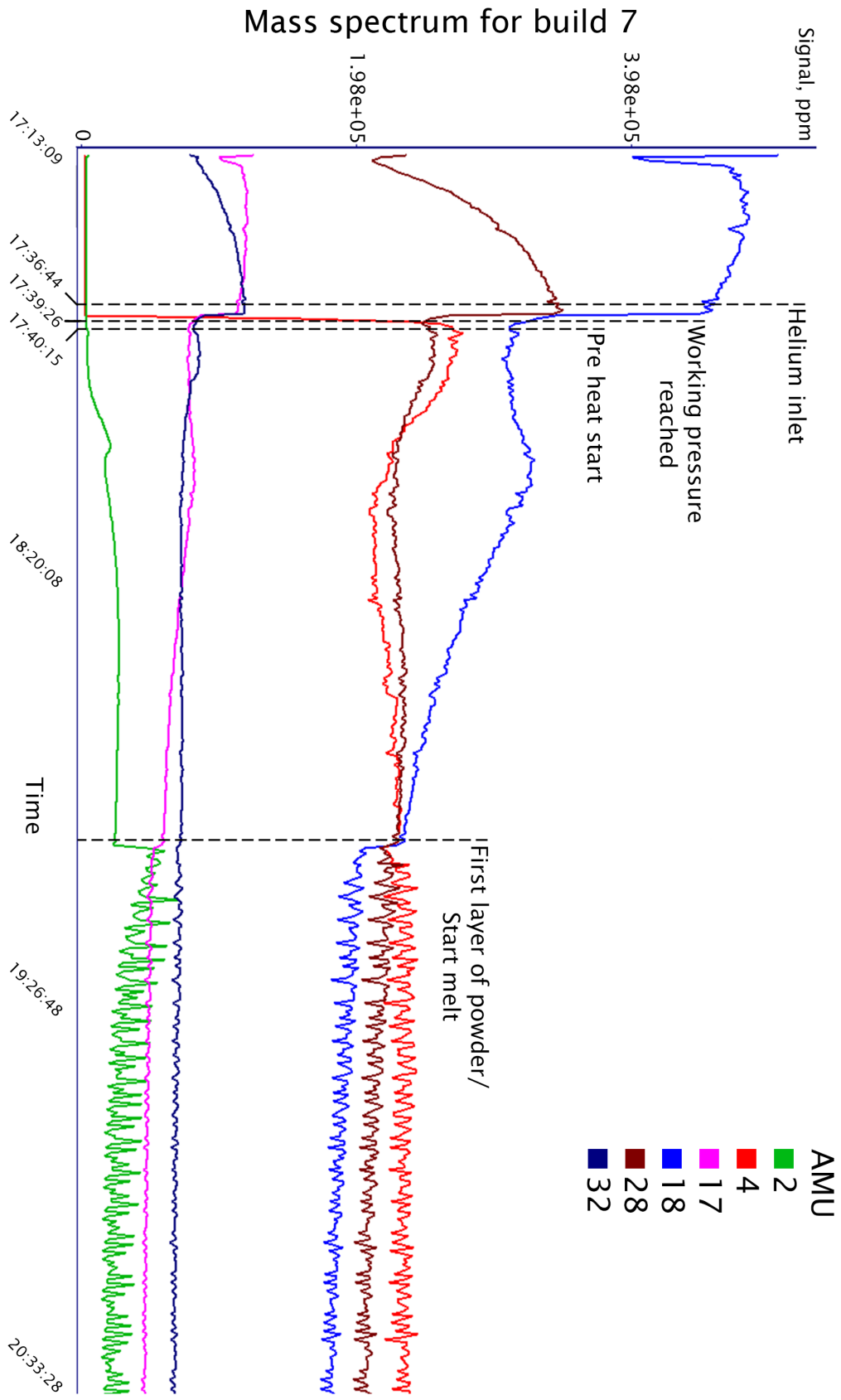

Figure 4.4: Zoomed view of the mass spectrometry for build 7.

4.3 Inert Gas Fusion Analysis

The IGFA revealed a moderate increase in oxygen concentration in the powder, seen in figure 4.5a and 4.5c, for both the sifted and unsifted powder. The same reports also contributed with the nitrogen concentration present in the same powder samples, which are shown to stay consistent throughout all build cycles, shown in figure 4.5b and figure 4.5d. As it can be seen in figure 4.6, the oxygen content in the powder during a build cycle B1, B2, and B3 appears to be stable. This is not verified in the successive builds because of limited access to the LECO ON736, which prevented continued investigation with such a high sample frequency.

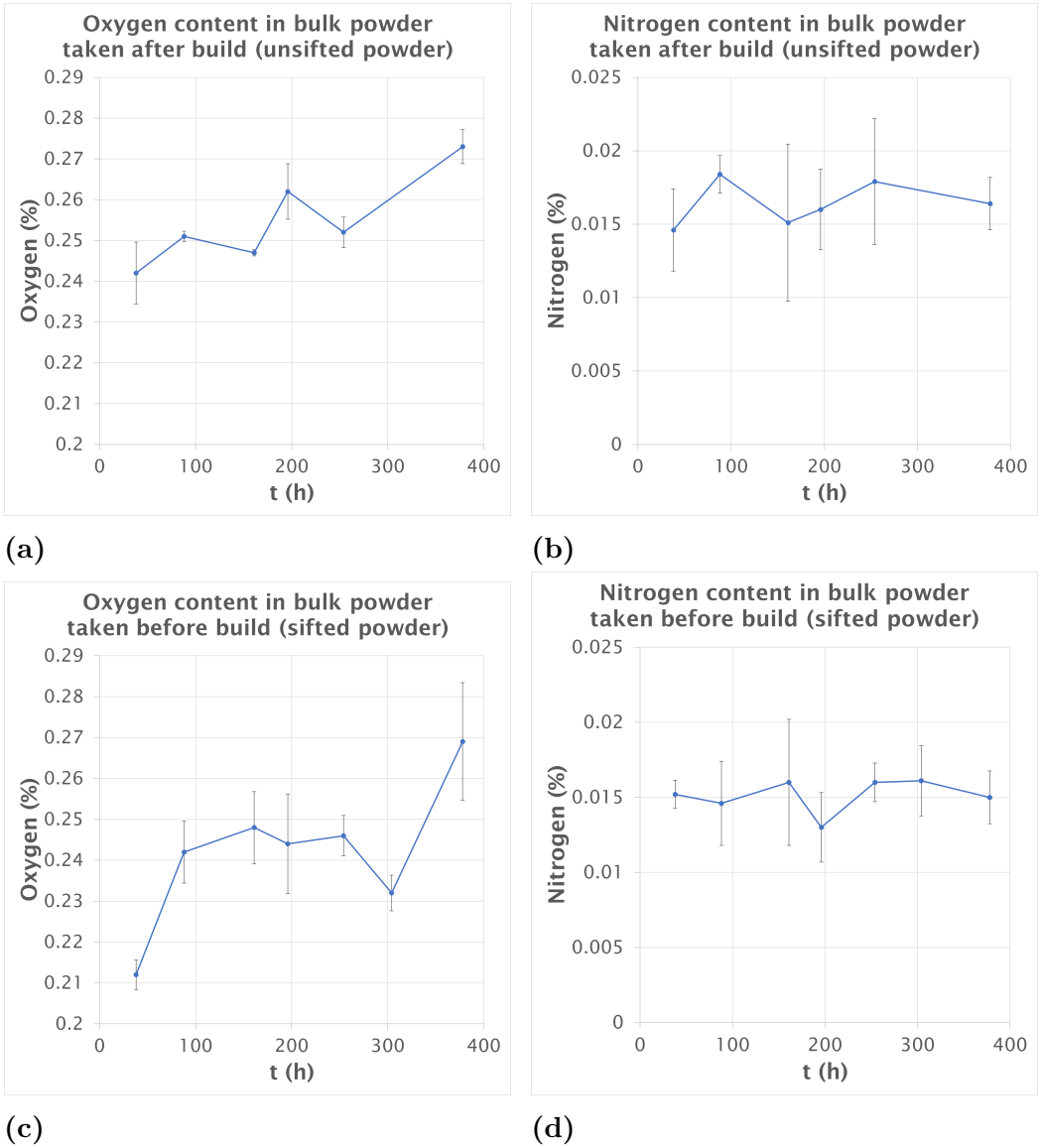

Figure 4.5: IGFA results of the oxygen and nitrogen levels between B1 and B7.

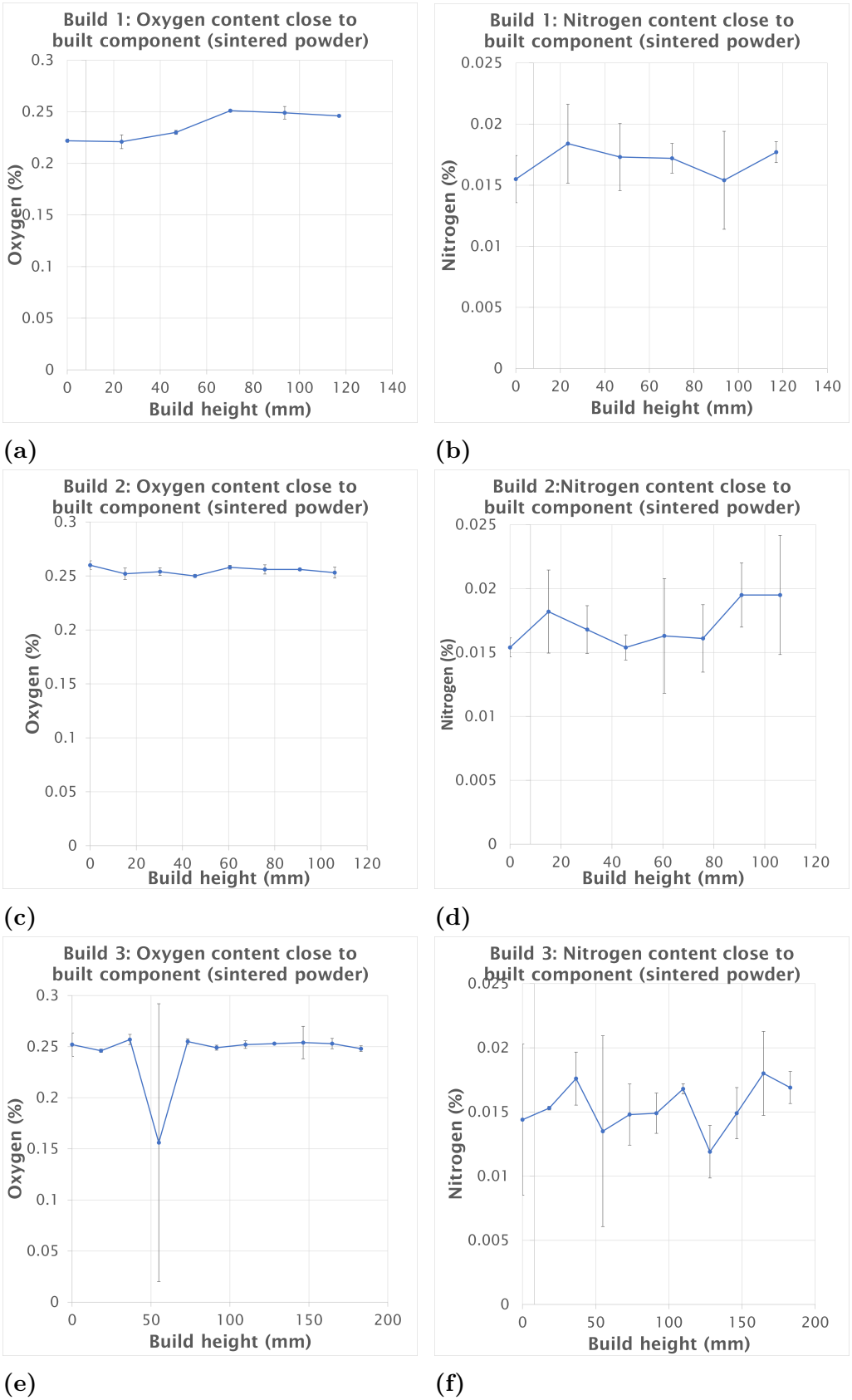

Figure 4.6: IGFA results for build 1. The total build time was approximately 38h. The sampling interval correlates with seven hours of build time, where the sample closest to the build plate (0 mm) has spent the longest time at elevated temperature

4.4 X-ray photoelectron spectroscopy

The survey spectra show nearly identical intensity for the peaks of interest for B1 and B7, as seen in figure 4.7. Figures 4.8a and 4.8b, show the relative intensity of the Ti2p and O1s peaks versus sputtering depth.

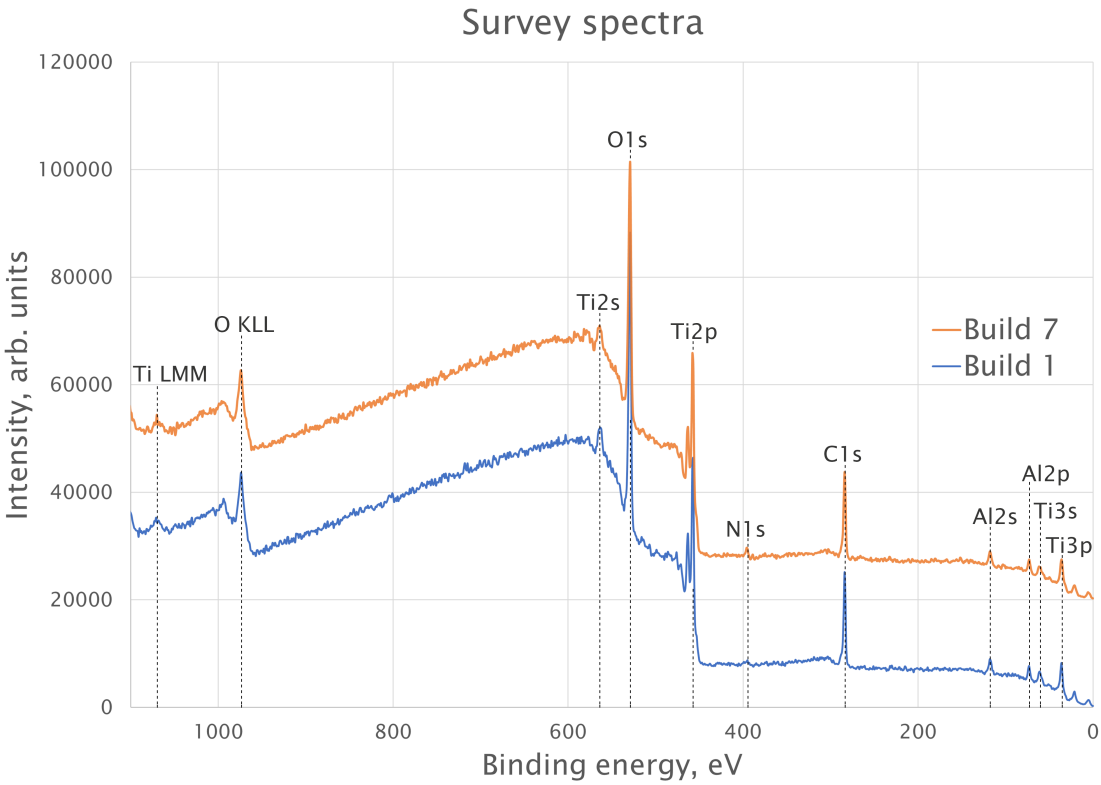

Figure 4.7: An overlay of the survey spectra for B1 and B7.

The calculations of the oxide thicknesses based on the same data showed a slight increase between the two samples. By referencing the metal peak Ti2p, a possible increase of the oxide thickness was up to 0 nm and 14 nm, in B7 powder was obtained, and require a more dedicated fitting to get to the exact values. By instead referencing the oxide peak O1s for the same powder, an increase of ~ 3 nm between B1 and B7 could be derived. The total amount of build time between B1 and B7 were roughly 217h.

High oxygen content on the as-received surface is an indication of the thick oxide layer and presence of carbon is connected to the absorbed carbon species, removed after etching. The oxygen concentration appears to stabilise at around a depth of 100 nm.

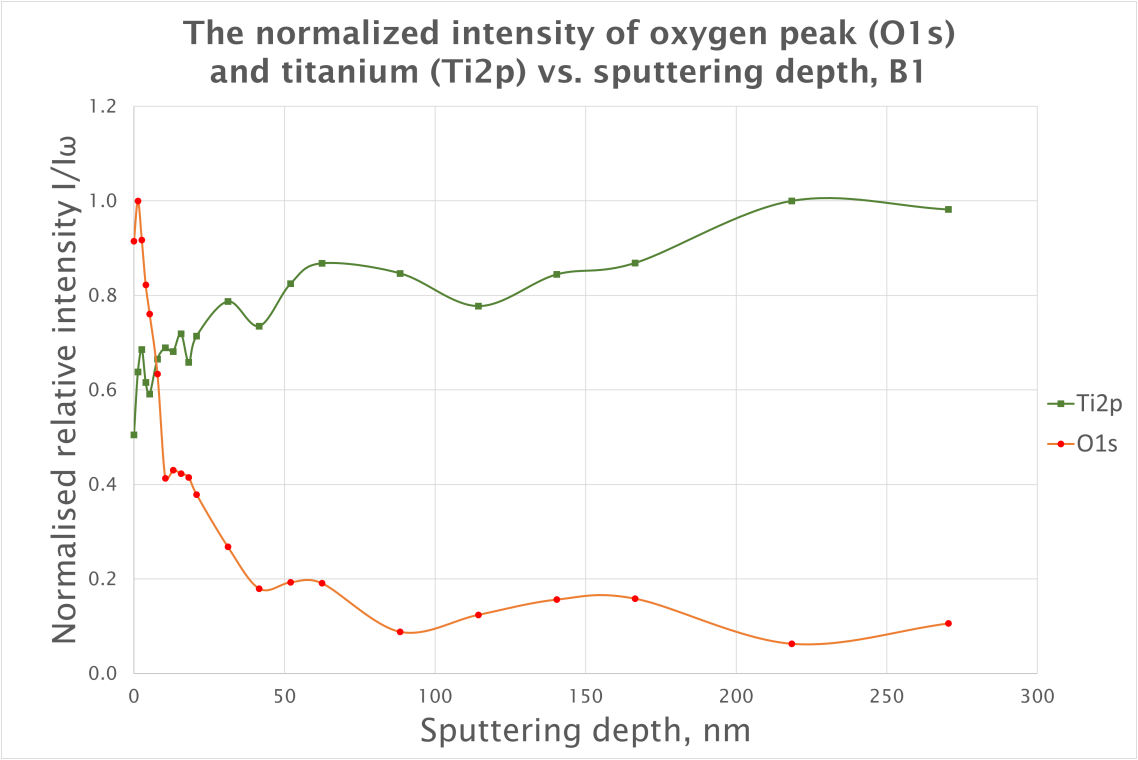

(a)

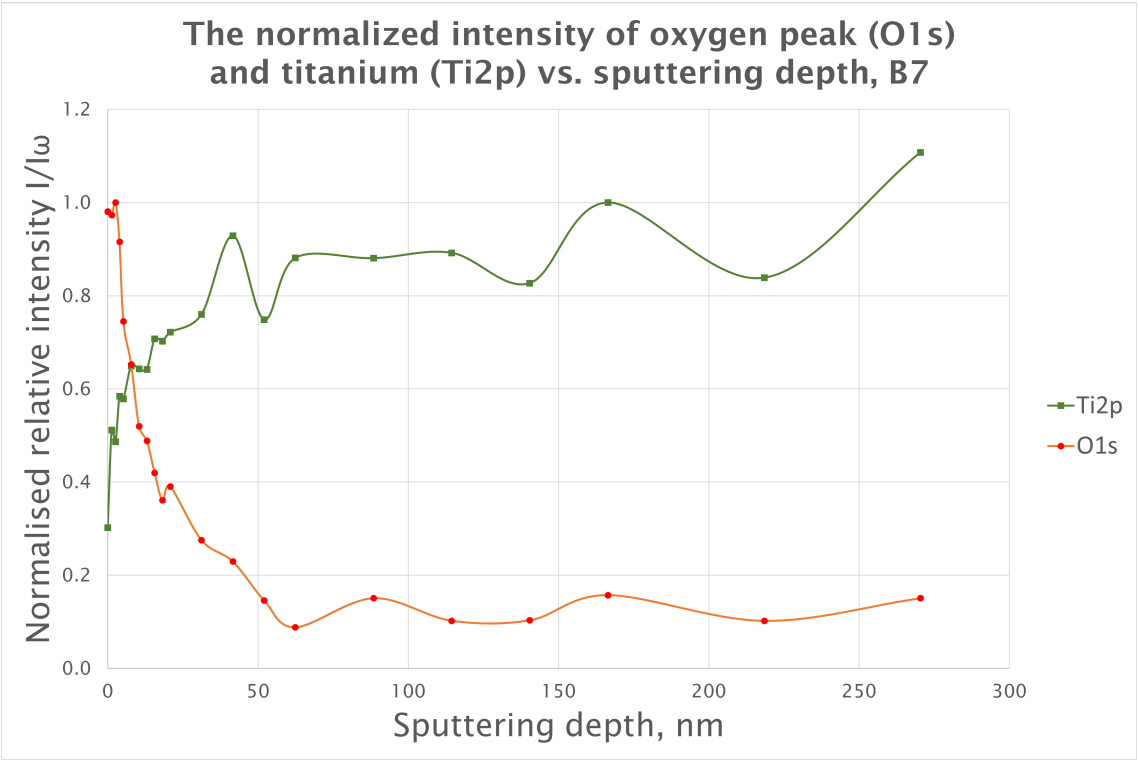

(b)

Figure 4.8: The intensity peaks for both titanium (Ti2p) and oxygen (O1s) for B1-B and B7-B. The initial intensity for the Ti2p is fluctuating too much to be discernible. The O1s peak in figure 4.8a and 4.8b on the other hand, is much more distinguishable.

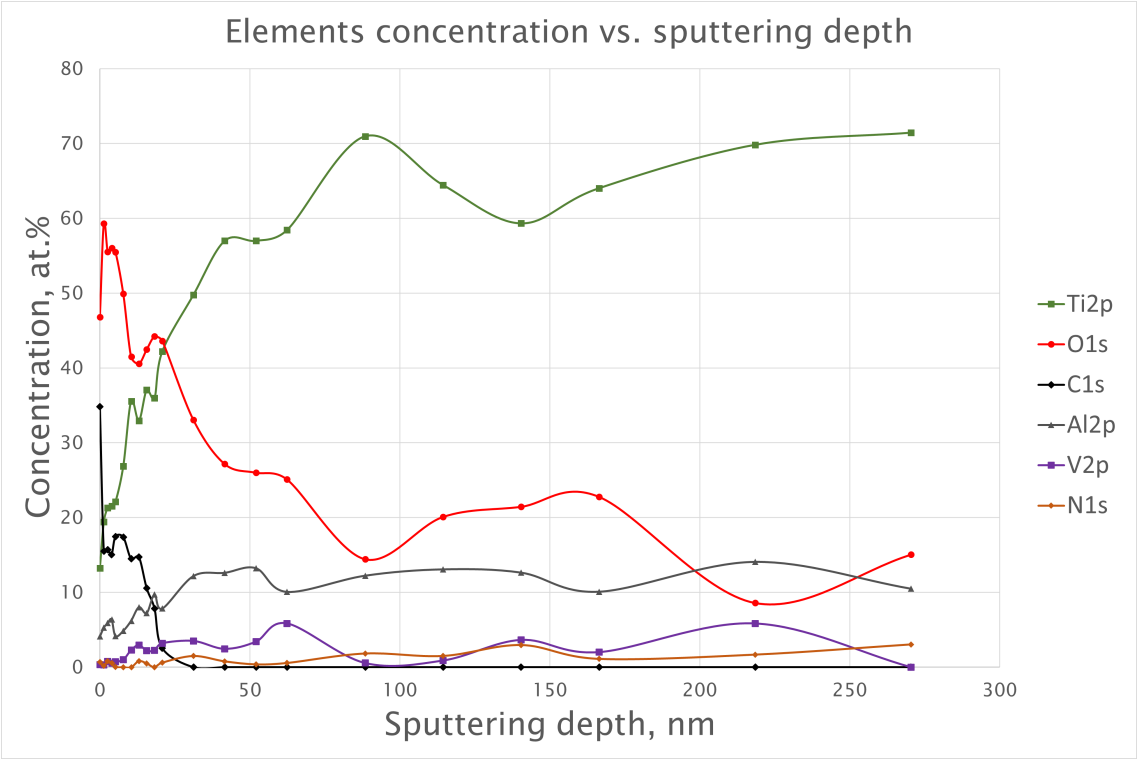

(a)

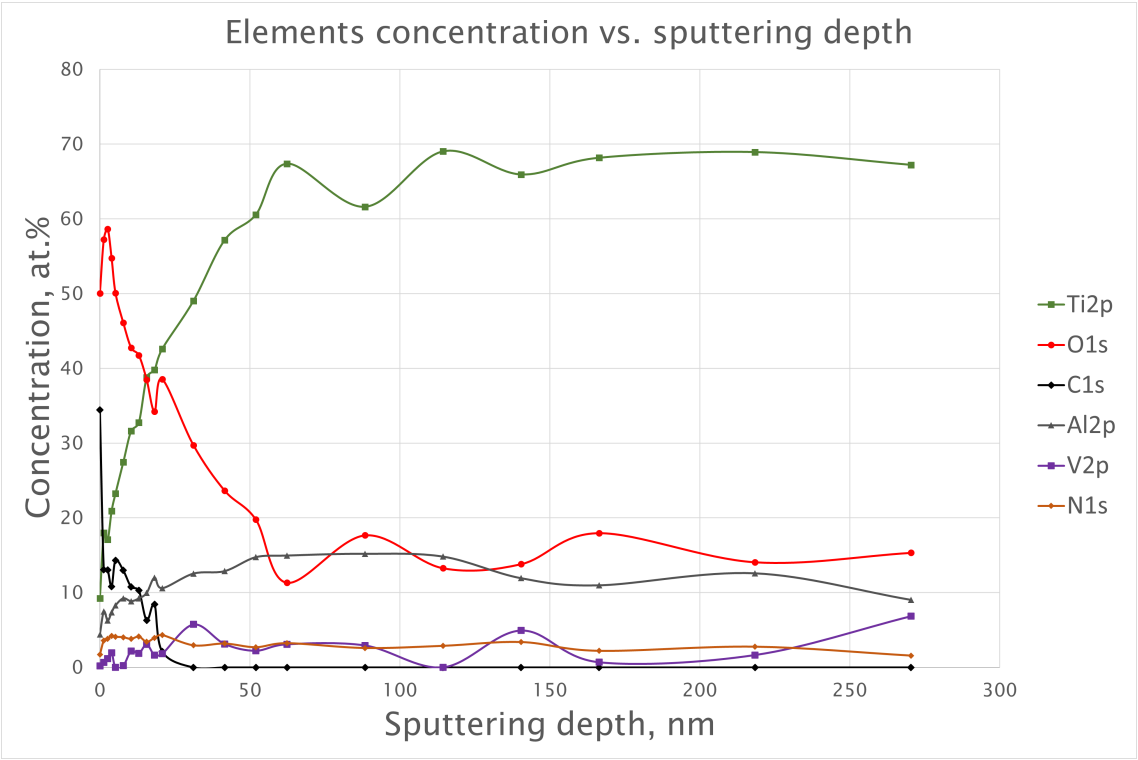

(b)

Figure 4.9: The figures above shows the element concentration versus sputtering depth of the powder samples from B1 4.9a and B7 4.9b

4.5 SEM

The SEM analysis showed that the powder samples between B1 and B10 are visually similar. There is no visual indication that there has been a change in the powder size distribution between the build cycles. The morphology of the powder has also stayed consistent between builds, as a higher quantity of satellites and deformed particles do not appear to be perceptible between B1-A and B10-A. The increase in oxygen content is not discernible from the SEM images.

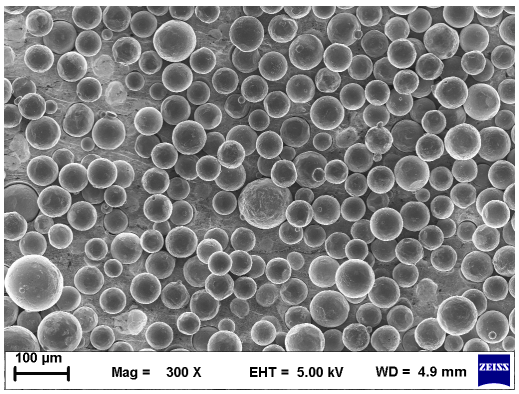

(a) B1-A, 300x magnification.

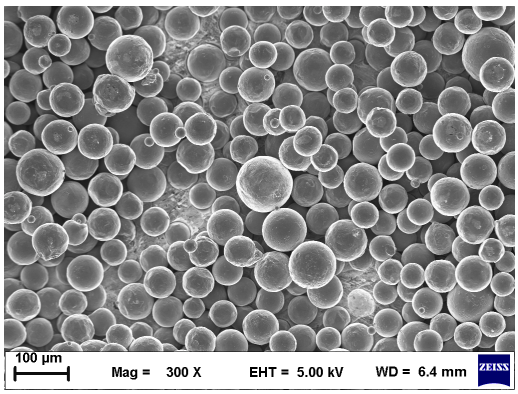

(b) B10-A, 300x magnification.

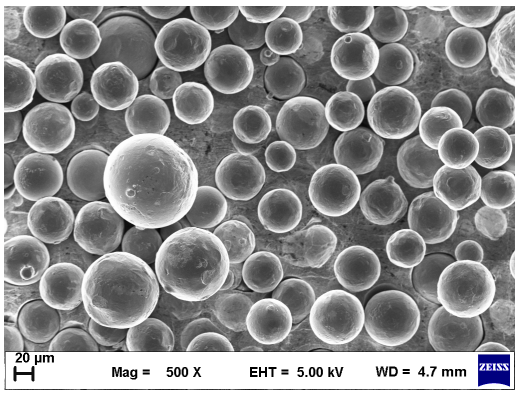

(c) B1-A, 500x magnification.

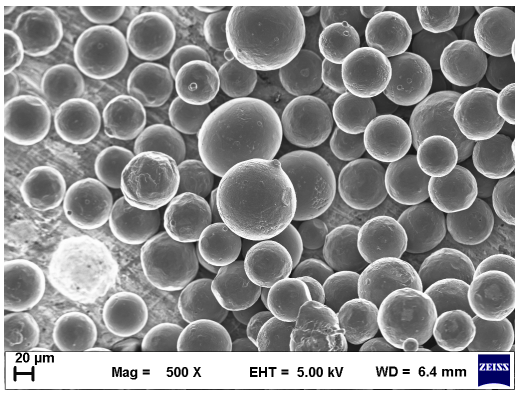

(d) B10-A, 500x magnification.

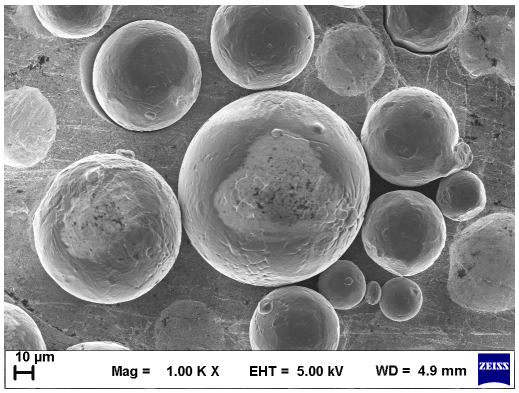

(e) B1-A, 1000x magnification.

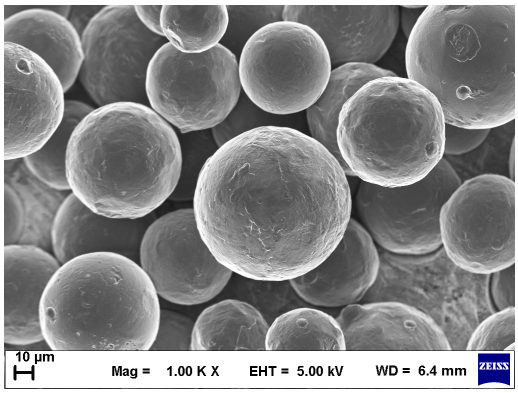

(f) B10-A, 1000x magnification.

Figure 4.10: Images from the SEM analysis conducted on samples B1 and B10. Also available in appendix C in a larger image size.

5
Discussion

After consulting an expert at Linde Gas AB, it was determined that an insufficient off-gas flow caused the low POA readings and likely resulted in invalid measurements (Equipment expert at Linde Gas AB, personal communication, April 29, 2021). Another issue that possibly would have affected the steep concentration fluctuations of both oxygen sensors could be explained by hydrogen influencing the measurement of the electromotive force. The oxygen partial pressure measured by the VAC sensor is around a magnitude lower than the theoretical value suggested to be present in the EBM process by Gruber et al. [28], which suggests this sensor also could be affected by some problems. A known problem exists for lambda sensors used in atmospheres containing hydrocarbons. The hydrocarbons accumulate on the zirconium ceramic, creating a sharp decrease in the oxygen content near the sensor, which results in a lower measured value of the oxygen content during printing [29]. This problem would be more common in processes where hydrocarbon-based lubricants are used to a larger extent.

The initially steeply decreasing oxygen content observed for the VAC sensor could, as previously mentioned, be caused by a number of reasons considered in discussions with experts at Linde Gas AB (Equipment expert at Linde Gas AB, personal communication, April 29, 2021). Suppose a high concentration of hydrogen is present close to the sensor, and due to the hot nature of the sensor, resulting in a reaction of the hydrocarbon with the oxygen on the hot surface of the sensor, therefore, resulting in a higher EMF and a lower oxygen concentration measured. Hydrogen could result from water cracking into its constituents due to beam interactions and the intense heat in the process. The initial decrease in the oxygen concentration corresponds within seconds to the onset of beam current during the preheating of the chamber, seen in figure 4.1, which then proceeds to dip even further when melting begins. Similar results can be observed throughout all build cycles, seen in figures B.2b-B.9b in appendix B. These results would further imply that hydrogen is released as the beam heats the chamber. This decrease in oxygen is also supported by an increase of hydrogen in the relative composition, observed when studying the MS results in figure 4.4, also correlating within seconds of starting the preheating and the decrease in oxygen measured by the oxygen sensors.

The water present could be due to several factors, e.g. from the residual atmosphere as the vacuum is pumped, through moisture adsorbed onto the surface of the powder and metallisation in the chamber. Another potential cause could be that minor amounts of air are supplied to the system. The effects from hydrogen

would be most influential when the process has the highest concentration of water. If the water concentration decreased over the build cycle, the hydrogen supply would decrease, explaining why the oxygen sensor stabilises after the initial spike. As observed in figure B.1a, the dew point meter showed a steadily decreasing water content within hours of the initial effects from the onset of preheating and melting. It can also be observed that the dew point meter shows a plateau after preheating has begun, where the maximum value of 20.06 °C, or 11,650 ppm is achieved, as seen in figure B.1b. The instrument has reached its upper measurement limit at this point, meaning a higher water content could very well be possible. Similar results can be seen for build cycle B3 seen in figure B.3a, and build cycles 7-11 in figures B.5a - B.9a. When studying build cycles 2 and 6, seen in figures B.2a and B.4a, the water content appears to be lower initially. This could be a result of lower humidity when the print cycles were started. A suspected under-pressure, which also possibly caused the POA sensor to malfunction, meant that the validity of the dew point meter measurements could not be verified. The low off-gas flow also meant the dew point meter has a slower response time; however, the values would still indicate a significant change, which was discussed during a meeting with the instrument supplier Linde Gas AB (Equipment expert at Linde Gas AB, Personal Communication, April 29, 2021).

The oxygen content presented in the results, measured by the VAC sensor, could be considered a low concentration after the value has stabilised under 0.1 ppm. Helium 4.6 is specified to contain up to 5 ppm of oxygen, according to the supplier Linde Gas AB (Applications expert at Linde Gas AB, Personal communication, May 5, 2021). The measured oxygen concentration is thus within the specified limits for contaminants in helium 4.6. The dilution model proposes that the process atmosphere will eventually be replaced by helium, with the current gas flow into the system. This behaviour seems to be supported by the VAC sensor since the value stabilises at low oxygen concentration. It should be further investigated if this value is accurate since contaminants are supplied through the gas and may also enter through minor air leaks, which the MS results suggest. Also notable when studying the VAC sensor results is a periodicity in the oxygen concentration, which could result from the process steps taking place. With the various measurement techniques carefully synced and correlated with the internally logged data, the effect from each step in the process could be distinguishable, e.g. changing of beam current and raking. This could prove useful to establish the impact on process atmosphere variation and the powder's layer-wise oxygen uptake.

The most notable signals from the MS can be seen in table 4.1. The signal for 28 amu was proposed to be dominated by either CO or N_2, as both have a similar atomic mass and are expected to be present in the process to some degree. When studying figure 4.3 at, a steep increase in the 28 amu signal can be seen once the build process has finished, and the pressure starts to rise with the increasing flow of helium to start off the cooling phase. Minor leaks of air could explain the sudden increase in constituents other than helium in the process since only helium should be flowing into the system at this point. The leaks would only become apparent as the turbopumps

are disengaged when the cooling phase begins. Such a heavy increase seen in the 28 amu peak would not be feasible if it represented CO. This leads to the conclusion that the 28 amu peak represents N_2, since the relative composition of N_2 and O_2 in atmospheric air is approximately 3.7:1, were a similar ratio is observed in the MS.

The H_2 peak can be observed to increase as preheating begins seen in figure 4.4, and achieve its maximum value after the melting has started. He can be seen increasing as the helium inlet valve is opened, which leads to a relative decrease in H_2O, N_2, O_2 and OH.

As the preheating continues, The signal at 18 amu, representing water, increases initially, to later be surpassed by the He peak by the time the melting of the first powder layer occurs. The water concentration then continuously decreases throughout the build process, as seen in figure 4.3, and follows a similar characteristic trajectory as the moisture measured by the DP sensor in the off-gas. This result indicates that the system's moisture content is gradually reduced during a process cycle.

The N_2 peak can be observed to follow the same line characteristics as the He peak after an initial separation when melting starts, which can be observed when studying figures 4.3 and figure 4.4. What this result indicates is unsure. A possible cause for this behaviour could be that N_2 is entering the system through the same channels as the He and is, in turn, being regulated in the same fashion as the He.

Previous studies on powder recyclability have shown that oxygen increases with recycling of the powder [2][3][5][16]. The IGFA performed in this study revealed a moderate increase in oxygen concentration in the powder. The increase is most notable during the first 100 h and the last 100 h. The reloading sequence for the powder used in this thesis, and explained in figure 3.3, could have limited the powder's exposure to the electron beam and contributed to the small increase in oxygen concentration. On the other hand, it could also represent a more realistic use case for external clients. The reasoning being that an EBM would not be used with barely enough powder, as it would increase the risk of a failed build cycle.

Sun et al. [2] found that the oxygen increase occurred in the bulk material, more notably in the β-phase. The same study showed little to no growth in oxide-layer thickness over 30 build cycles. It did not prove easy to distinguish a clear interface from the XPS results in this study, especially when studying the metal Ti2p peak. This could possibly be due to the higher initial oxygen concentration of the powder used in this study. The O1s peak showed less fluctuation in intensity and was therefore used to approximate the thickness. According to the same report mentioned previously [2], using a powder with the same theoretical size distribution, an oxide layer thickness of 10 nm corresponds to less than 200 ppm oxygen. As the difference in oxide thickness could range between 0 nm - 3 nm in this study, it would correspond with a small relative increase in the total oxygen concentration.

6

Conclusions

The first research questions in this thesis focused mainly on the oxygen concentration of the process atmosphere and how it affects the uptake of oxygen by the powder. The second research question was to explore what correlations could be made about the process atmosphere interactions between the different measurement techniques. With these questions in mind, the main findings of this study are presented below:

- There appears to be a low supply of oxygen introduced from the process atmosphere, which supports the moderate increase in oxygen content measured in the powder.
- The powder used had a high initial oxygen concentration, which could also be significant for the low oxygen pick-up seen in the study.
- A small increase in oxide layer thickness (up to 3 nm) can be observed in the studied powder. This is roughly in agreement with the slight oxygen uptake registered.
- The powder morphology and overall visual appearance studied in scanning electron microscopy remained unchanged.
- Residual air and humidity are notable constituents of the process atmosphere as the process starts. These constituents are gradually replaced by helium during as the manufacturing process takes place, where the oxygen content stabilises to a partial pressure around 0.04 ppm in the process as measured by the VAC sensor. This value is lower than the theoretical value proposed. The value is within the limit of oxygen contained in the helium, and the oxygen content did not vary significantly between builds.
- The gas flow exiting the Q20plus proved to be insufficient for the extractive lambda sensor, rendering it unusable for this specific process. Since the off-gas sensors are likely to measure in an under-pressure, the dew point meter values may be inaccurate. The low flow might cause the dew point meter to have a slower response time, but general trends in water concentration should be visible.
- The mass spectrometry results potentially indicate minor air leaks into the vacuum chamber, as the relative amounts of nitrogen remain stable while the process atmosphere was replaced by helium.

6.1 Recommendations for future work

The first recommendation is to use a MS capable of working in the high vacuum chamber. This would give insight into the exact chemical composition of the process atmosphere. Since the VAC sensor showed stable results, it would be plausible to investigate its accuracy using the MS. If it is of continued interest to study the oxygen concentration in the off-gas, chemical sensors might be more successful in further analysis as they are known to be more compatible with a low flow and not as sensitive to hydrocarbons and hydrogen. Measuring the pressure at the location of the off-gas sensors could give insight into the validity of the dew point meter measurements, and help confirm if the POA sensor failed due to under-pressure and low off-gas flow.

The periodicity of the fluctuations found in the oxygen signal could be studied further to possibly find information about the oxidation behaviour of the EBM process. The fluctuations are found in figures B.1a - B.18b in appendix B. The data could perhaps provide more knowledge about layer-wise oxidation behaviour by correlating the fluctuations to either the beam current or the rake movement. One thing to consider is the timing of the data, as the timestamps between sensors may differ in the second range, and the response time of the sensors may create a delayed measurement.

It could be of interest to measure the chemical composition of the helium supplied to the EBM, to establish the effect of gas contaminants in the He on the oxygen and water vapour content in the EBM chamber during the build.

By using a virgin powder in a similar in-situ analysis, further insights into the early stages of oxygen accumulation could be gained.

Bibliography

[1] J. Karlsson, *Optimization of Electron Beam Melting for Production of Small Components in Biocompatible Titanium Grades*. 2015, volume 80, pp. 978–991, ISBN: 978-91-554-9110-9.

[2] Y. Sun, M. Aindow, and R. J. Hebert, "The effect of recycling on the oxygen distribution in Ti-6Al-4V powder for additive manufacturing," *Materials at High Temperatures*, vol. 35, no. 1-3, 2018, ISSN: 09603409. DOI: 10.1080/09603409.2017.1389133.

[3] H. P. Tang, M. Qian, N. Liu, X. Z. Zhang, G. Y. Yang, and J. Wang, "Effect of Powder Reuse Times on Additive Manufacturing of Ti-6Al-4V by Selective Electron Beam Melting," *JOM*, vol. 67, no. 3, 2015, ISSN: 15431851. DOI: 10.1007/s11837-015-1300-4.

[4] M. Mahdi Siblani, M. Ollivier, and L. Favergeon, "An experimental study of Ti-6Al-4V powder reactivity in gaseous environment: Application to additive manufacturing," *MATEC Web of Conferences*, vol. 321, p. 3035, 2020. DOI: 10.1051/matecconf/202032103035.

[5] P. Nandwana, W. H. Peter, R. R. Dehoff, L. E. Lowe, M. M. Kirka, F. Medina, and S. S. Babu, "Recyclability Study on Inconel 718 and Ti-6Al-4V Powders for Use in Electron Beam Melting," *Metallurgical and Materials Transactions B: Process Metallurgy and Materials Processing Science*, vol. 47, no. 1, pp. 754–762, 2016, ISSN: 10735615. DOI: 10.1007/s11663-015-0477-9. [Online]. Available: https://link.springer.com/article/10.1007/s11663-015-0477-9.

[6] GE Additive. (n.d.). "About Arcam | GE Additive," [Online]. Available: https://www.ge.com/additive/who-we-are/about-arcam (visited on 04/30/2021).

[7] M. Galati and L. Iuliano, "A literature review of powder-based electron beam melting focusing on numerical simulations," vol. 19, pp. 1–20, Jan. 2018, ISSN: 22148604. DOI: 10.1016/j.addma.2017.11.001.

[8] Arcam AB. (2015). "Arcam Q20 Technical Data," [Online]. Available: www.arcam.com/wp-content/uploads/Arcam-Q20-final.pdf (visited on 04/15/2021).

[9] V. Lunetto, M. Galati, L. Settineri, and L. Iuliano, "Unit process energy consumption analysis and models for Electron Beam Melting (EBM): Effects of process and part designs," *Additive Manufacturing*, vol. 33, p. 101 115, May 2020, ISSN: 22148604. DOI: 10.1016/j.addma.2020.101115.

[10] GE Additive. (n.d.). "Arcam EBM Q20plus - Aerospace Component AM Machine | GE Additive," [Online]. Available: https://www.ge.com/additive/

additive-manufacturing/machines/ebm-machines/arcam-ebm-q20plus (visited on 05/12/2021).

[11] ——, (n.d.). "Arcam EBM Q20plus - Brochure," [Online]. Available: https://www.ge.com/additive/sites/default/files/2020-07/EBM_QPlus20_Bro_A4_EN_v1.pdf (visited on 04/20/2021).

[12] The Editors of Encyclopaedia Britannica. (2021). "Titanium | Properties, Uses, & Facts | Britannica," [Online]. Available: https://www.britannica.com/science/titanium#ref1042708 (visited on 02/28/2021).

[13] A. Palmquist, A. Snis, L. Emanuelsson, M. Browne, and P. Thomsen, "Long-term biocompatibility and osseointegration of electron beam melted, free-form–fabricated solid and porous titanium alloy: Experimental studies in sheep," *Journal of Biomaterials Applications*, vol. 27, no. 8, pp. 1003–1016, May 2013, ISSN: 0885-3282. DOI: 10.1177/0885328211431857. [Online]. Available: https://pubmed.ncbi.nlm.nih.gov/22207608/.

[14] ASTM. (2014). "ASTM F2924-12: Standard Specification for Additive Manufacturing Titanium-6 Aluminum-4 Vanadium with Powder Bed Fusion," [Online]. Available: https://www.astm.org/Standards/F2924.htm (visited on 05/03/2021).

[15] GRANTA Design Limited, *GRANTA Edupack 2020*, version 20.1.0, Cambridge, 2020.

[16] V. Petrovic and R. Niñerola, "Powder recyclability in electron beam melting for aeronautical use," *Aircraft Engineering and Aerospace Technology*, vol. 87, no. 2, pp. 147–155, Mar. 2015, ISSN: 00022667. DOI: 10.1108/AEAT-11-2013-0212.

[17] LibreTexts. (May 2020). "Dalton's Law (Law of Partial Pressures)," [Online]. Available: https://chem.libretexts.org/@go/page/1518 (visited on 03/19/2021).

[18] AGA Gas AB. (2021-08-03). "How do you control your oxygen process level?" [Online]. Available: https://www.linde-gas.se/sv/images/Oxysensor%20English_tcm586-405133.pdf (visited on 02/15/2021).

[19] Vaisala. (n.d.). "DMP248 Dewpoint and Temperature Transmitter," [Online]. Available: http://www.iprocessmart.com/images/Vaisala/DMP248.pdf.

[20] LECO. (n.d.). "736 Series Inert Gas Fusion," [Online]. Available: https://www.leco.com/product/736-series (visited on 04/01/2021).

[21] D. Briggs, "X-ray photoelectron spectroscopy (XPS)," *Handbook of Adhesion: Second Edition*, pp. 621–622, 2005. DOI: 10.1002/0470014229.ch22.

[22] Chalmers University of Technology. (2020-09-19). "Scanning Electron Microscopy (SEM) | Chalmers," [Online]. Available: https://www.chalmers.se/en/researchinfrastructure/CMAL/instruments/SEM/Pages/default.aspx (visited on 05/19/2021).

[23] Arcam EBM. (2017). "Operation Manual Q10plus," [Online]. Available: www.arcam.com/wp-content/uploads/Arcam-Q10.pdf (visited on 02/25/2021).

[24] AP&C. (n.d.). "Ti-6AI-4V Gr. 5 | Advanced Powders," [Online]. Available: https://www.advancedpowders.com/powders/titanium/ti-6al-4v-5 (visited on 06/04/2021).

[25] Yunus A. Cengel and Michael A. Boles, *Thermodynamics: An Engineering Approach*, 4th edition. Mcgraw-Hill College (June 1, 2001), ISBN: 978-0072383324.

[26] L. Nyborg, A. Nylund, and I. Olefjord, "Thickness determination of oxide layers on spherically-shaped metal powders by ESCA," *Surface and Interface Analysis*, vol. 12, no. 2, pp. 110–114, 1988, ISSN: 10969918. DOI: 10.1002/sia.740120209.

[27] Ceramic Oxide Fabricators. (n.d.). "Oxygen Concentration Calculators," [Online]. Available: https://www.cof.com.au/oxygen-sensors/nernst.html (visited on 05/27/2021).

[28] H. Gruber, M. Henriksson, E. Hryha, and L. Nyborg, "Effect of powder recycling in electron beam melting on the surface chemistry of alloy 718 powder," *Metallurgical and Materials Transactions A*, vol. 50, no. 9, pp. 4410–4422, Sep. 2019, ISSN: 1543-1940. DOI: 10.1007/s11661-019-05333-7. [Online]. Available: https://doi.org/10.1007/s11661-019-05333-7.

[29] E. Hryha and L. Nyborg, "Process control system for delubrication of PM steels," *Acta Metallurgica Slovaca*, vol. 18, no. 2-3, pp. 60–68, 2012, ISSN: 13381156.

A

IGFA data

Table A.1: Table containing values from IGFA for build 1.

Build 1				
Sample	**Oxygen avg. [%]**	**Oxygen std. dev. [%]**	**Nitrogen avg. [%]**	**Nitrogen std. dev. [%]**
1	0.222	0.00166	0.0155	0.00193
2	0.221	0.00666	0.0184	0.00323
3	0.230	0.00193	0.0173	0.00274
4	0.251	0.00124	0.0172	0.00122
5	0.249	0.00612	0.0154	0.00401
6	0.246	0.00110	0.0177	0.000859

Table A.2: Table containing values from IGFA for build 2.

Build 2				
Sample	**Oxygen Avg. [%]**	**Oxygen std. dev. [%]**	**Nitrogen avg. [%]**	**Nitrogen std. dev. [%]**
1	0.260	0.00391	0.0154	0.000740
2	0.252	0.00525	0.0182	0.00325
3	0.254	0.00363	0.0168	0.00187
4	0.250	0.00136	0.0154	0.000982
5	0.258	0.00176	0.0163	0.00449
6	0.256	0.00426	0.0161	0.00264
7	0.256	0.00110	0.0195	0.00251
8	0.253	0.00508	0.0195	0.00466

Table A.3: Table containing values from IGFA for build 3.

Build 3				
Sample	**Oxygen avg. [%]**	**Oxygen std. dev. [%]**	**Nitrogen avg. [%]**	**Nitrogen std. dev. [%]**
1	0.253	0.0051	0.0144	0.00588
2	0.252	0.0115	0.0153	0.00142
3	0.246	0.0017	0.0176	0.00207
4	0.257	0.005	0.0135	0.00743
5	0.255	0.0027	0.0148	0.00238
6	0.249	0.0025	0.0149	0.00157
7	0.252	0.0037	0.0168	0.00404
8	0.253	0.0008	0.0119	0.00205
9	0.254	0.0159	0.0149	0.00200
10	0.253	0.005	0.0180	0.00327
11	0.248	0.0028	0.0169	0.00125

Table A.4: Samples taken before each build cycle (sifted powder)

B-samples				
Sample	**Oxygen avg. [%]**	**Oxygen std. dev. [%]**	**Nitrogen avg. [%]**	**Nitrogen std. dev. [%]**
B1	0.212	0.00364	0.0152	0.000944
B2	0.242	0.00760	0.0146	0.00280
B3	0.248	0.0088	0.016	0.0042
B6	0.244	0.0122	0.013	0.00232
B7	0.246	0.00495	0.016	0.00129
B8	0.232	0.00435	0.0161	0.00233
B9	0.269	0.0144	0.015	0.00176

Table A.5: Samples taken after each build cycle (sintered powder)

A-samples				
Sample	**Oxygen avg. [%]**	**Oxygen std. dev. [%]**	**Nitrogen avg. [%]**	**Nitrogen std. dev. [%]**
A1	0.242	0.00760	0.0146	0.00280
A2	0.251	0.00124	0.0184	0.00128
A3	0.247	0.0008	0.0151	0.00535
A6	0.262	0.0068	0.016	0.00275
A7	0.252	0.00373	0.0179	0.00429
A9	0.273	0.00416	0.0164	0.00179

B

Sensor and dew point graphs

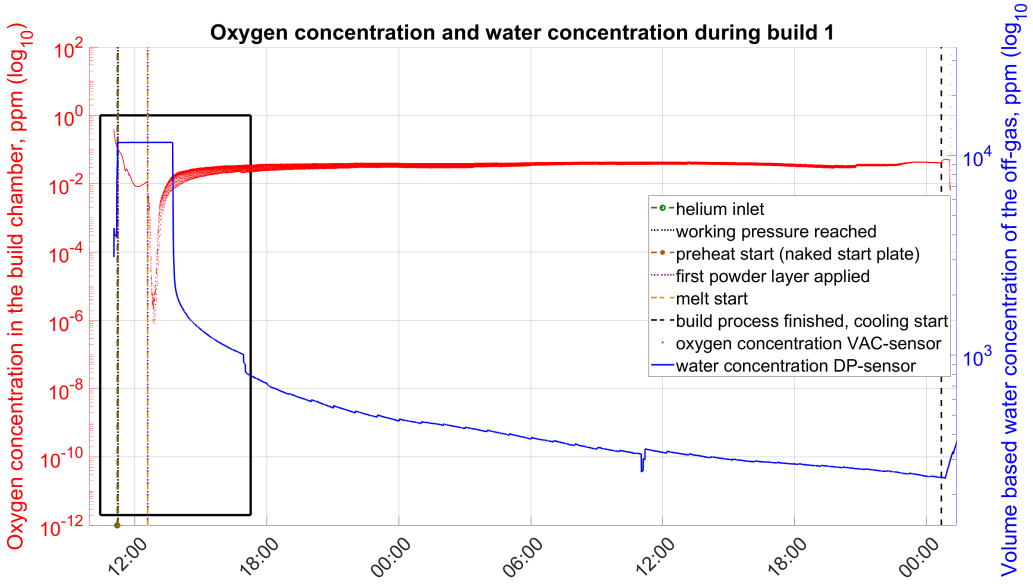

(a)

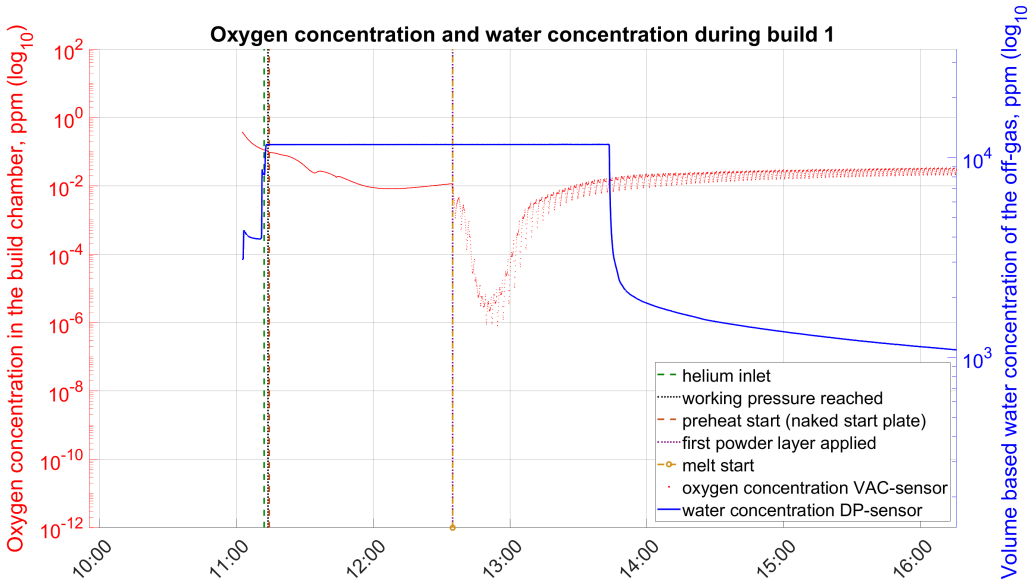

(b)

Figure B.1: An overlay for build cycle 1: The oxygen concentration in the build chamber (VAC) plotted on the primary axis, and water concentration of the off-gas plotted on the secondary axis. The preheat, start and stop times are correlated from the log files collected by the internal EBM software.

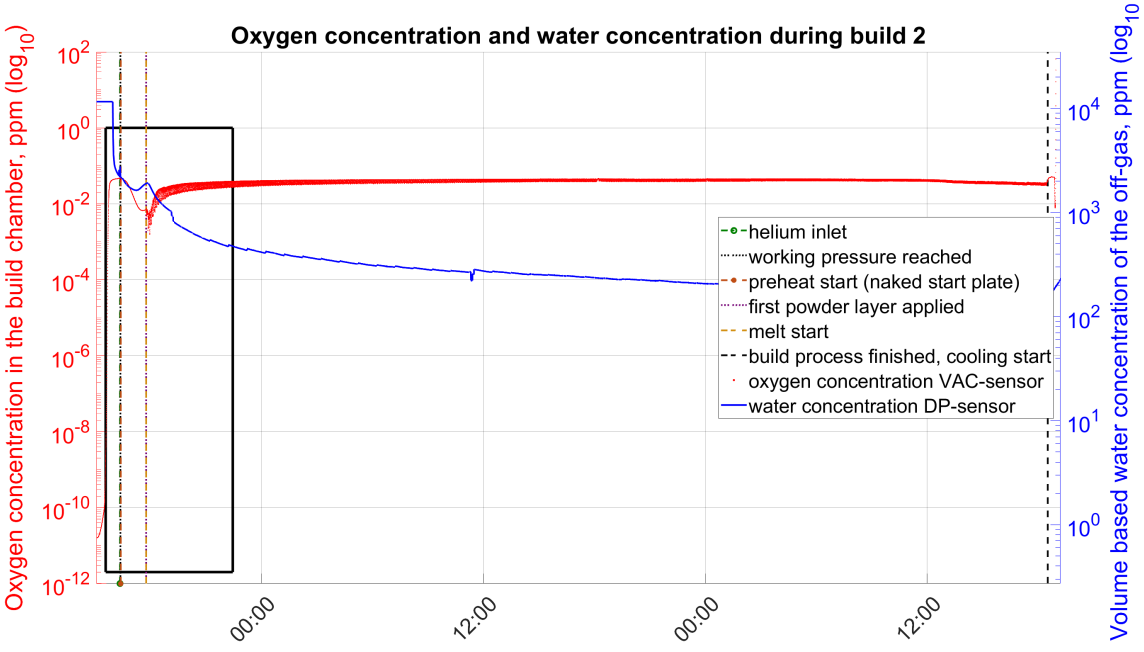

(a)

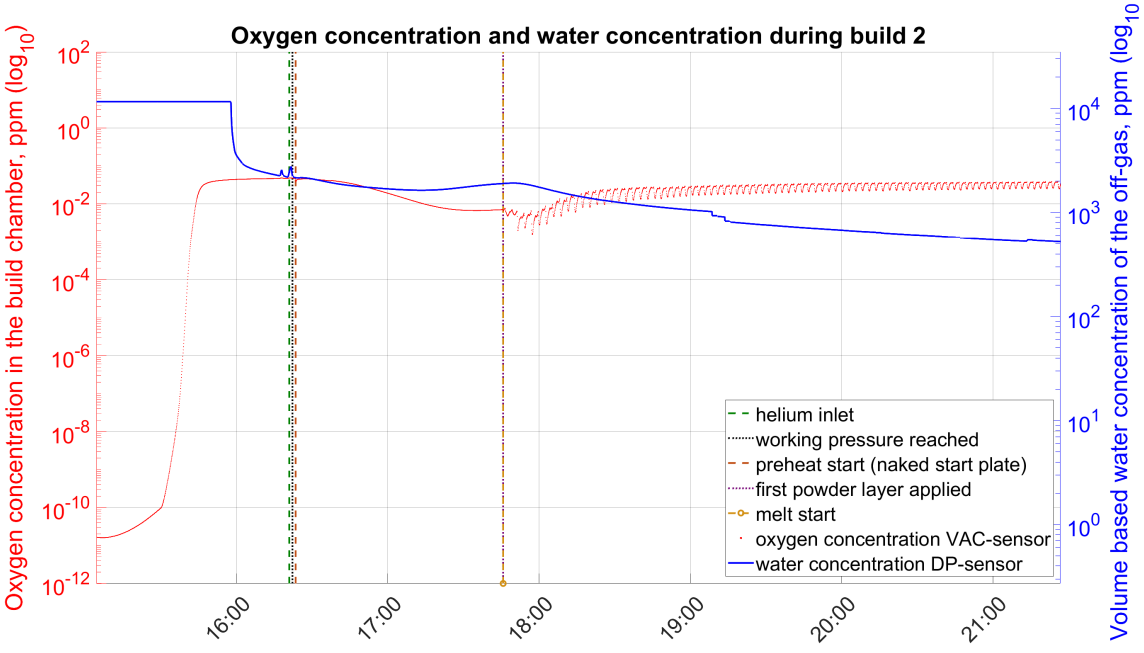

(b)

Figure B.2: An overlay for build cycle 2: The oxygen concentration in the build chamber (VAC) plotted on the primary axis, and water concentration of the off-gas plotted on the secondary axis. The preheat, start and stop times are correlated from the log files collected by the internal EBM software.

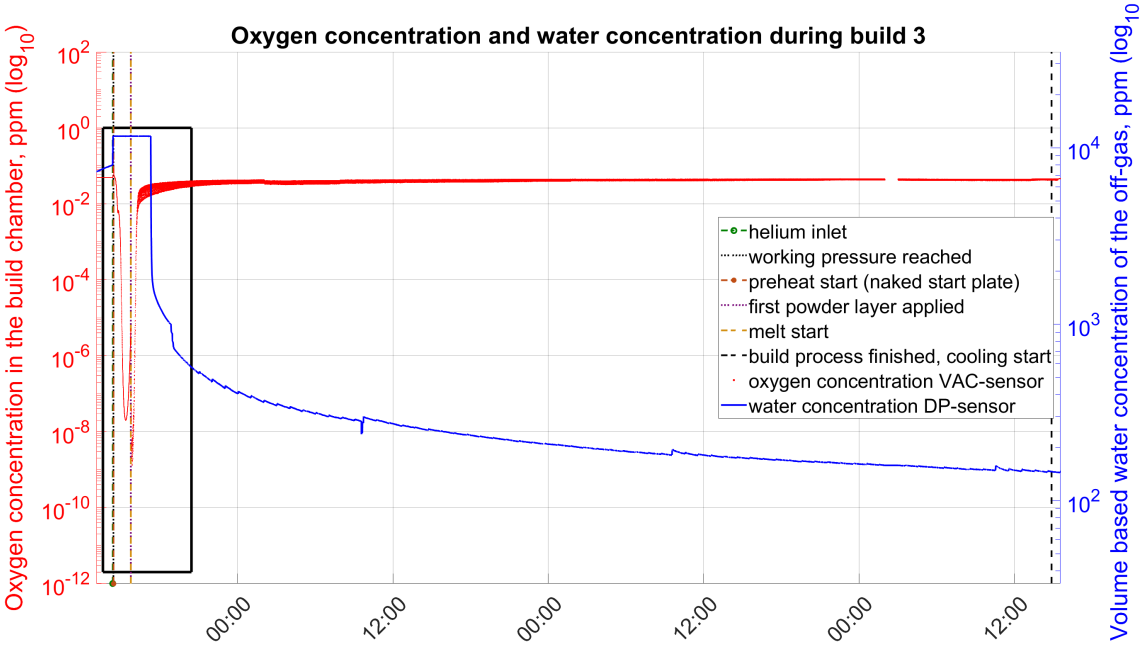

(a)

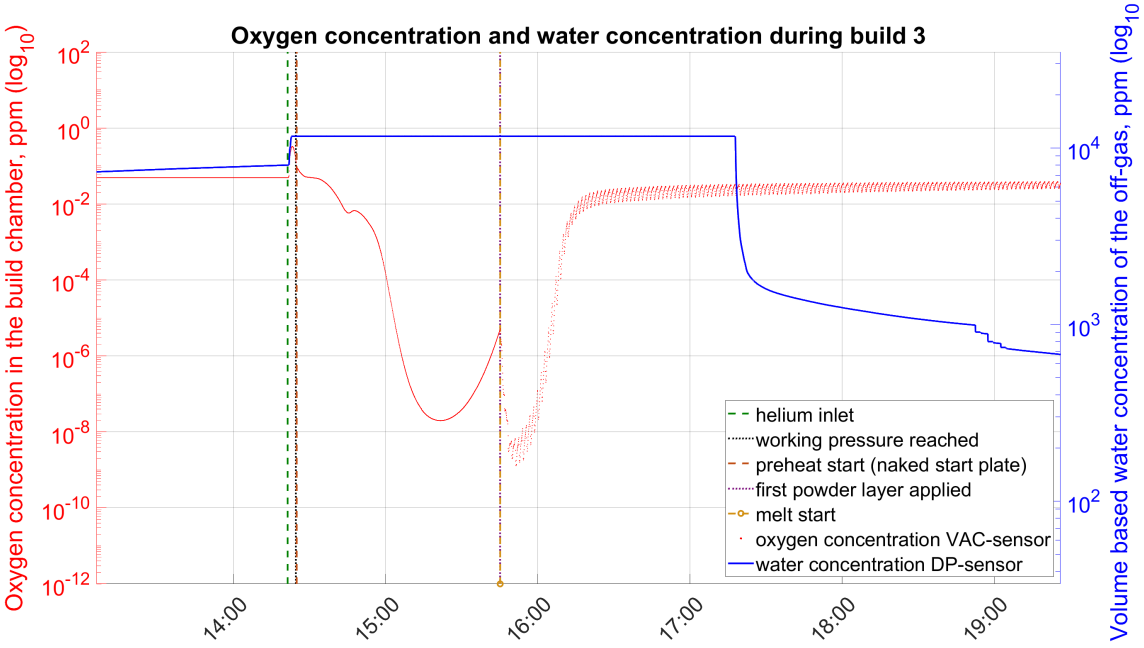

(b)

Figure B.3: An overlay for build cycle 3: The oxygen concentration in the build chamber (VAC) plotted on the primary axis, and water concentration of the off-gas plotted on the secondary axis. The preheat, start and stop times are correlated from the log files collected by the internal EBM software.

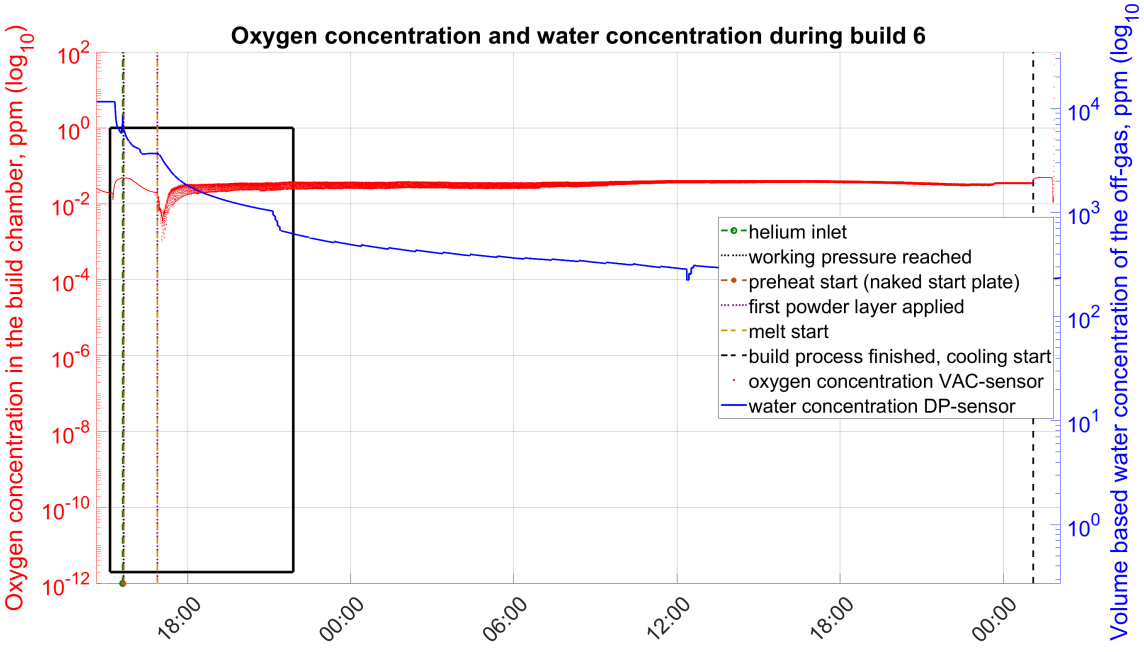

(a)

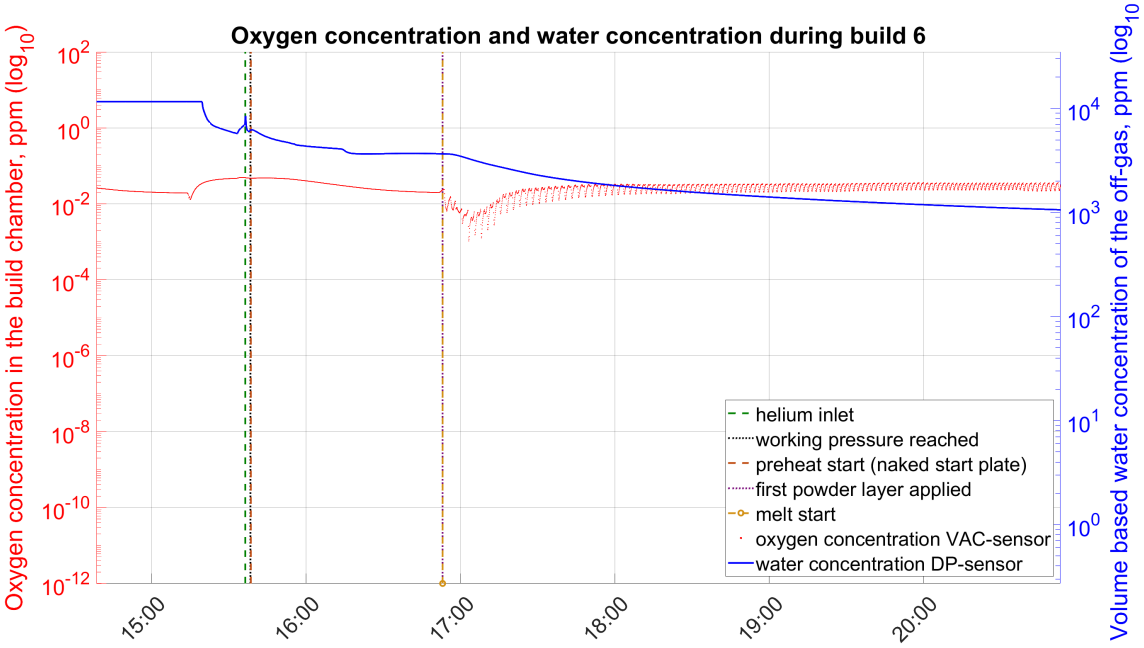

(b)

Figure B.4: An overlay for build cycle 6: The oxygen concentration in the build chamber (VAC) plotted on the primary axis, and water concentration of the off-gas plotted on the secondary axis. The preheat, start and stop times are correlated from the log files collected by the internal EBM software.

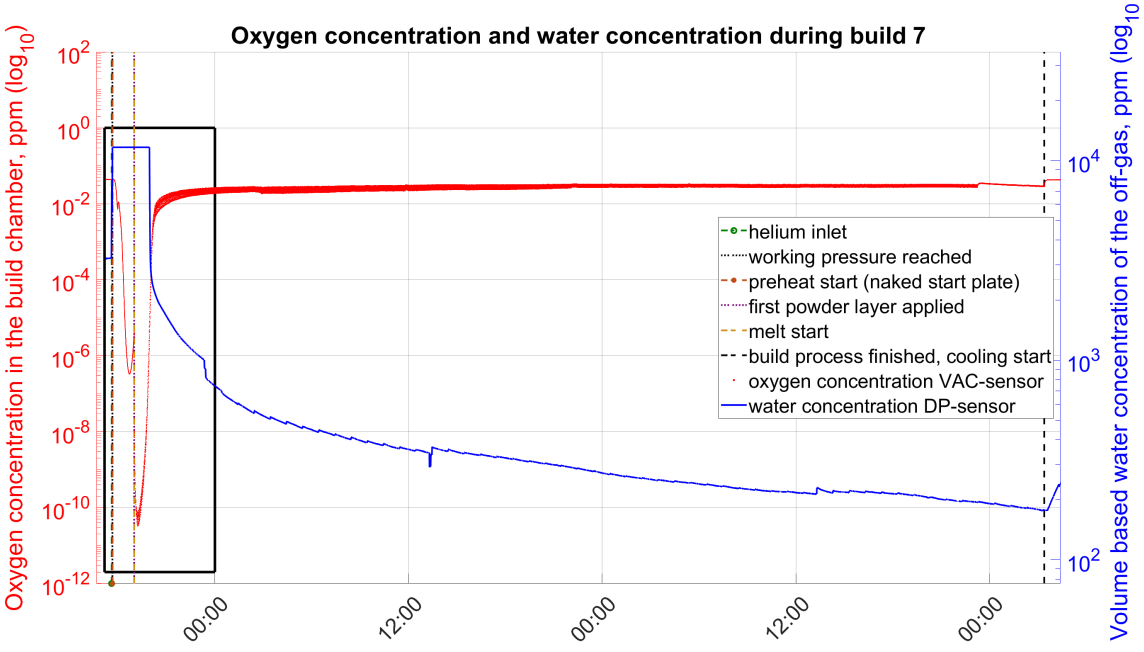

(a)

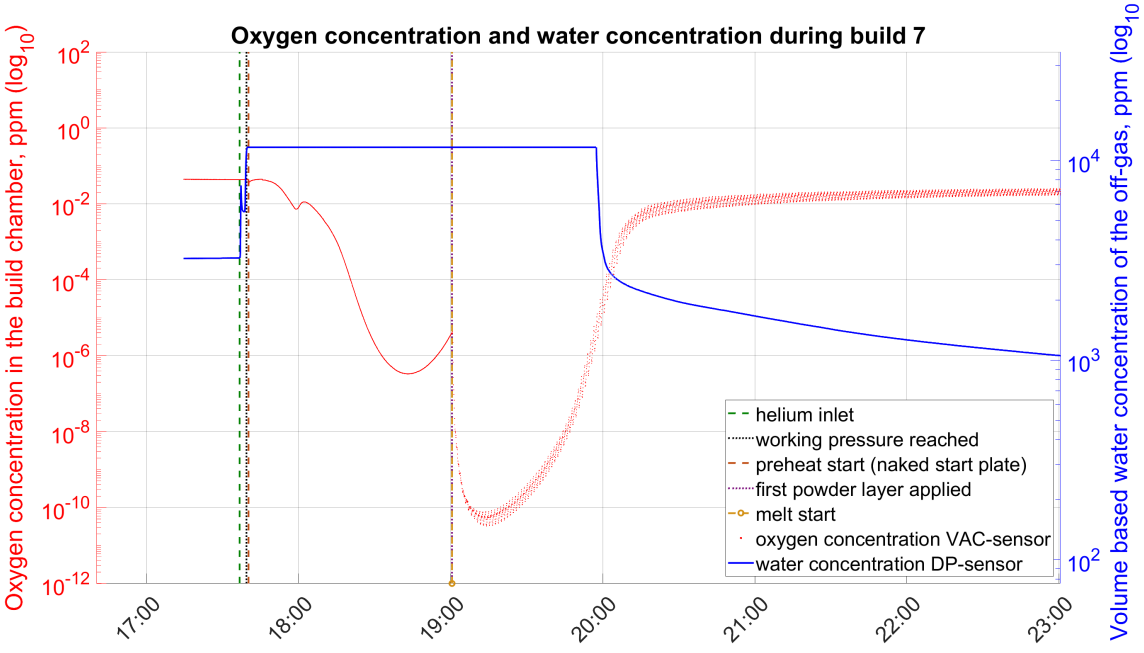

(b)

Figure B.5: An overlay for build cycle 7: The oxygen concentration in the build chamber (VAC) plotted on the primary axis, and water concentration of the off-gas plotted on the secondary axis. The preheat, start and stop times are correlated from the log files collected by the internal EBM software.

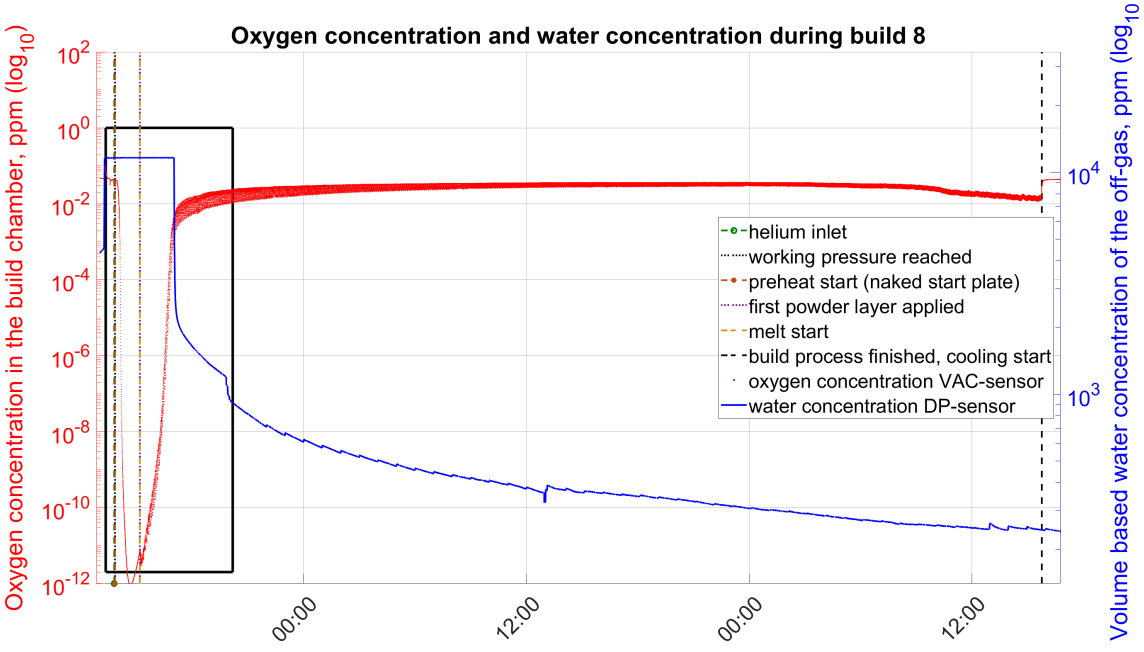

(a)

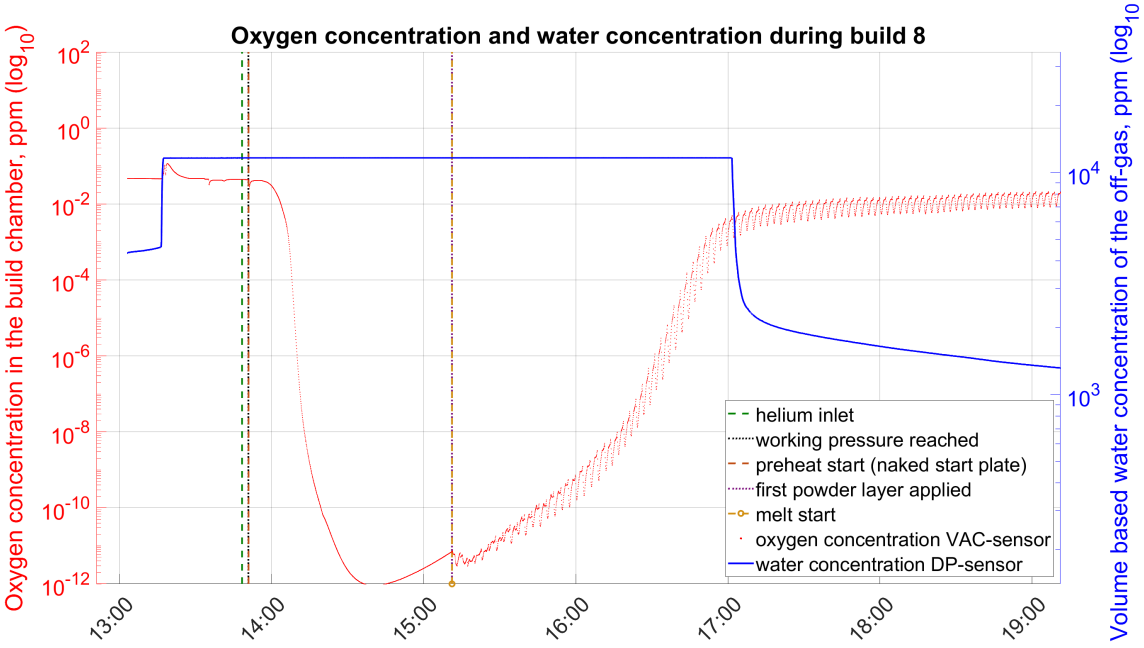

(b)

Figure B.6: An overlay for build cycle 8: The oxygen concentration in the build chamber (VAC) plotted on the primary axis, and water concentration of the off-gas plotted on the secondary axis. The preheat, start and stop times are correlated from the log files collected by the internal EBM software.

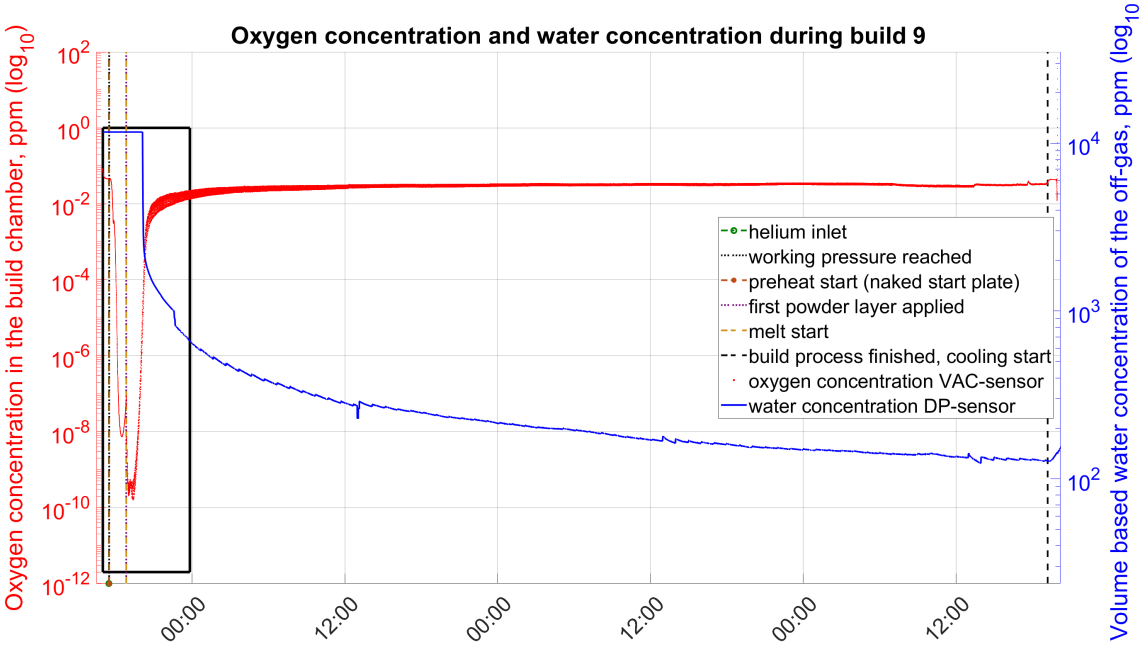

(a)

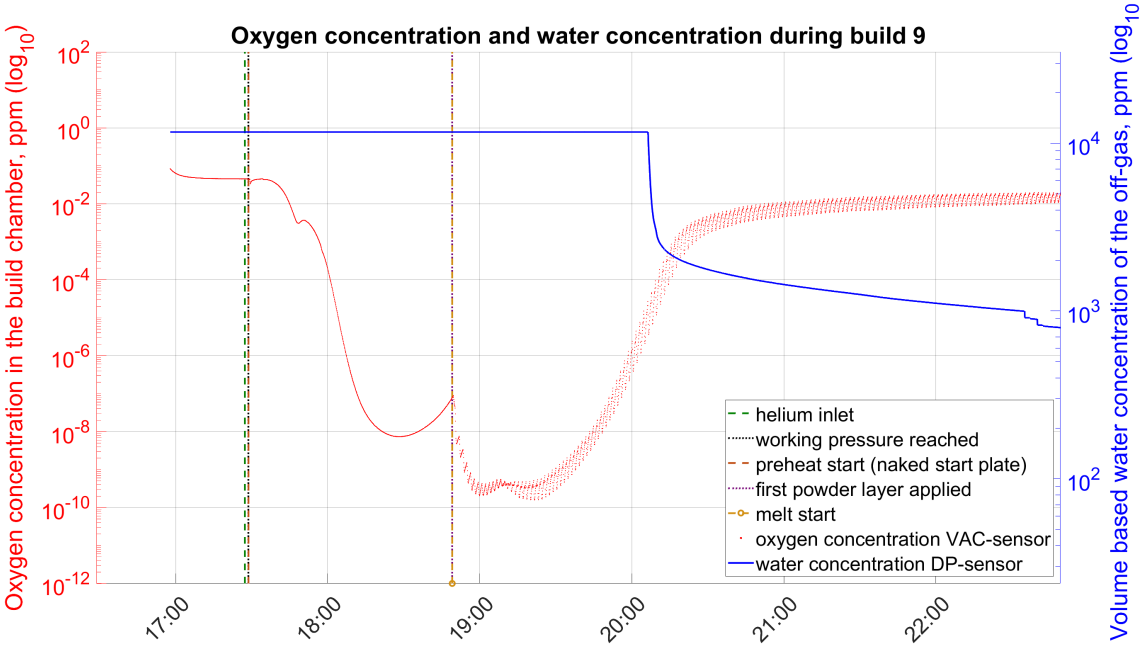

(b)

Figure B.7: An overlay for build cycle 9: The oxygen concentration in the build chamber (VAC) plotted on the primary axis, and water concentration of the off-gas plotted on the secondary axis. The preheat, start and stop times are correlated from the log files collected by the internal EBM software.

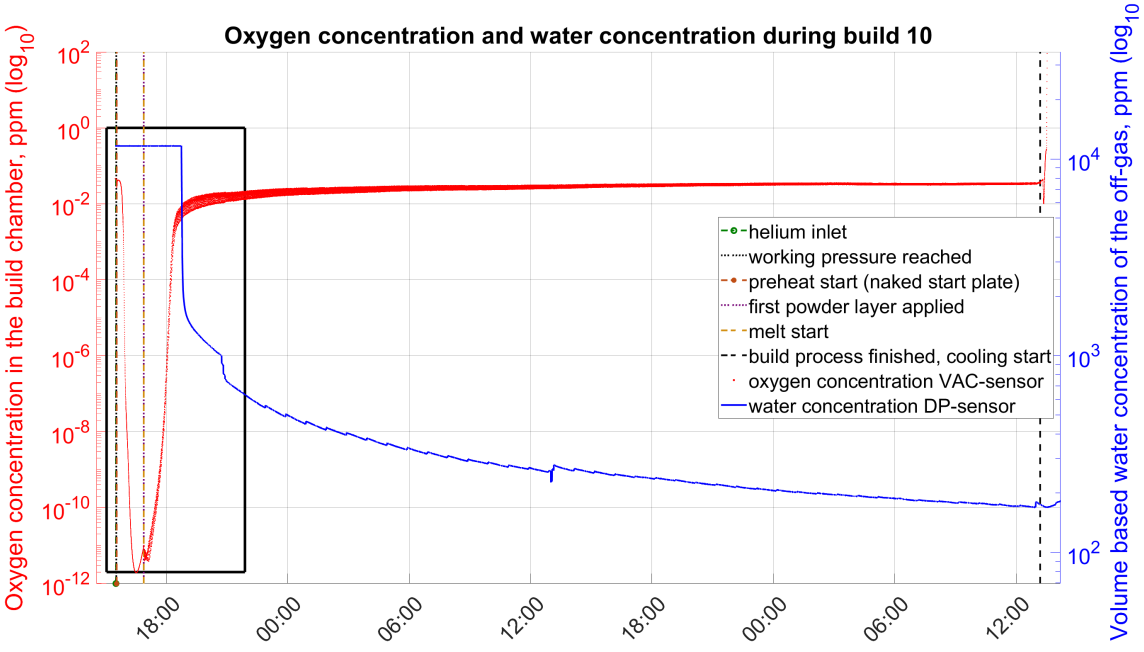

(a)

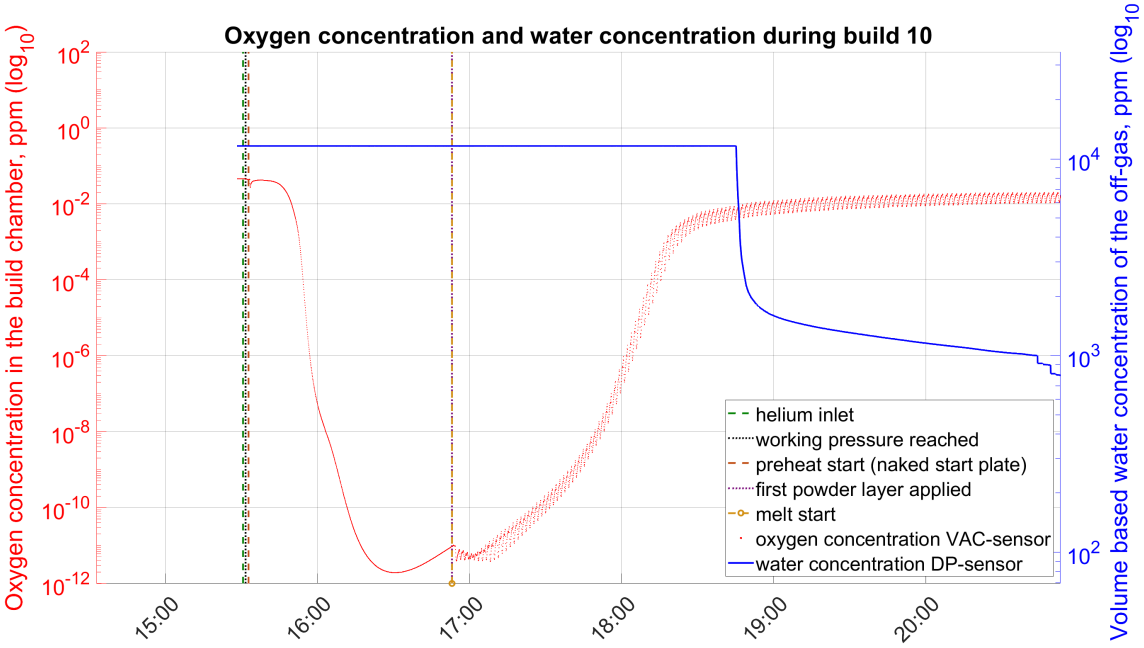

(b)

Figure B.8: An overlay for build cycle 10: The oxygen concentration in the build chamber (VAC) plotted on the primary axis, and water concentration of the off-gas plotted on the secondary axis. The preheat, start and stop times are correlated from the log files collected by the internal EBM software.

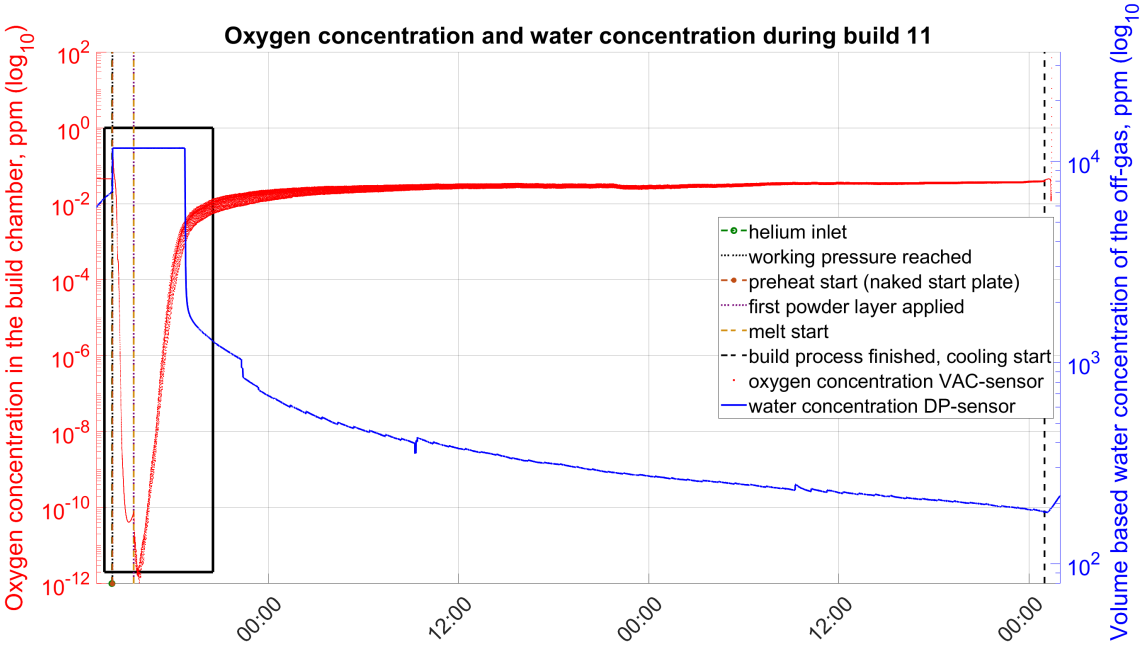

(a)

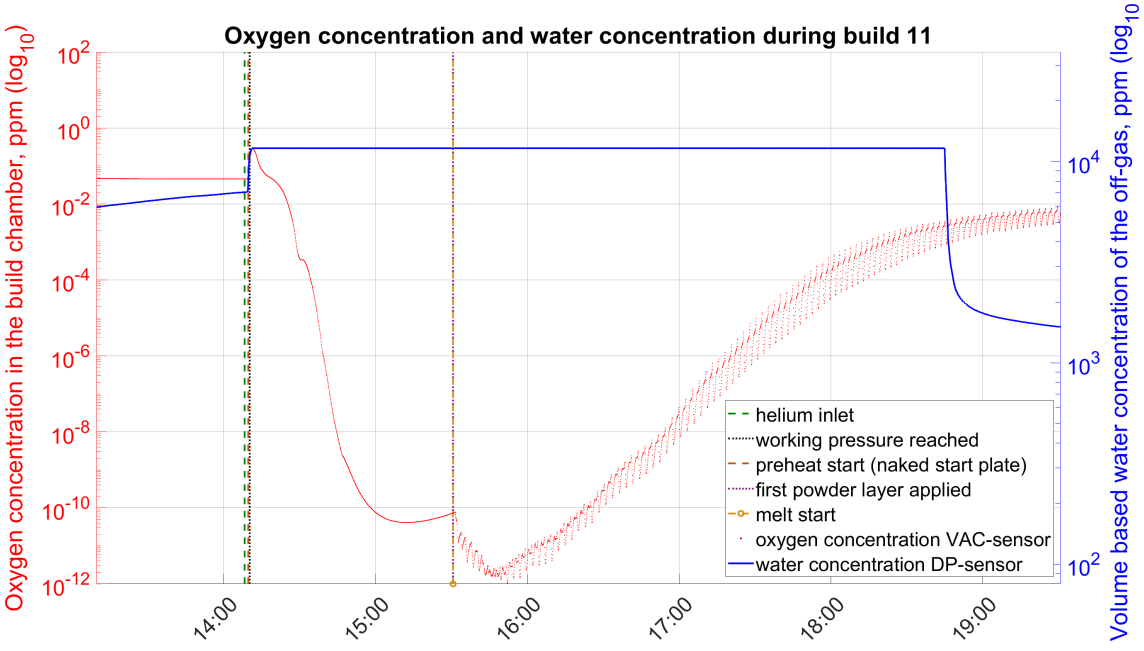

(b)

Figure B.9: An overlay for build cycle 11: The oxygen concentration in the build chamber (VAC) plotted on the primary axis, and water concentration of the off-gas plotted on the secondary axis. The preheat, start and stop times are correlated from the log files collected by the internal EBM software.

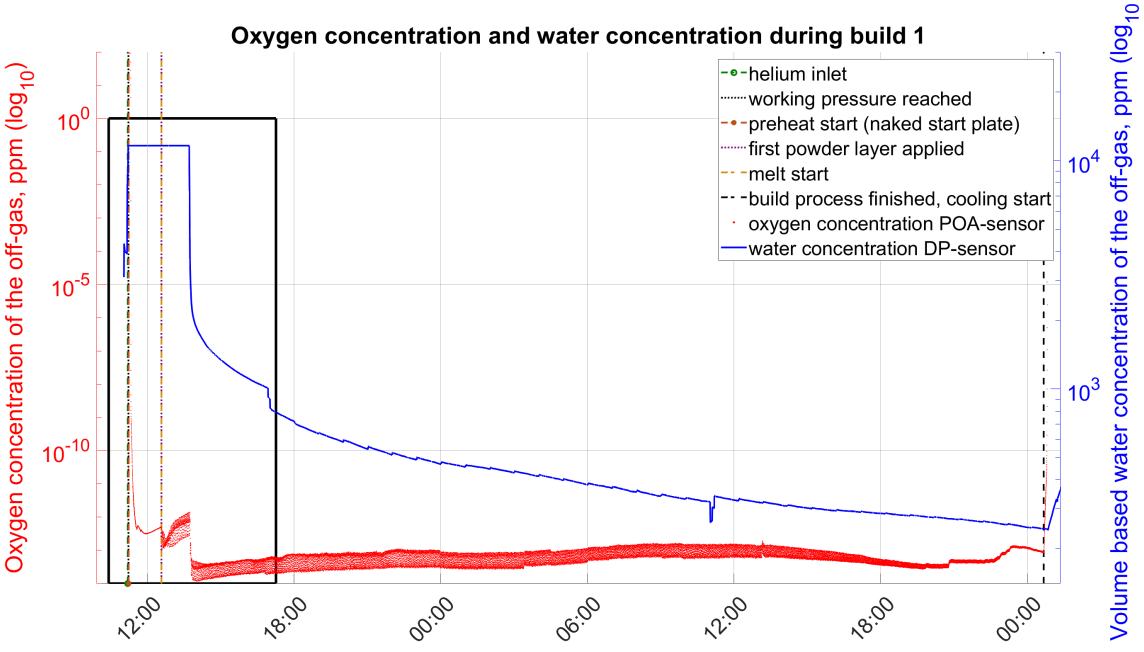

(a)

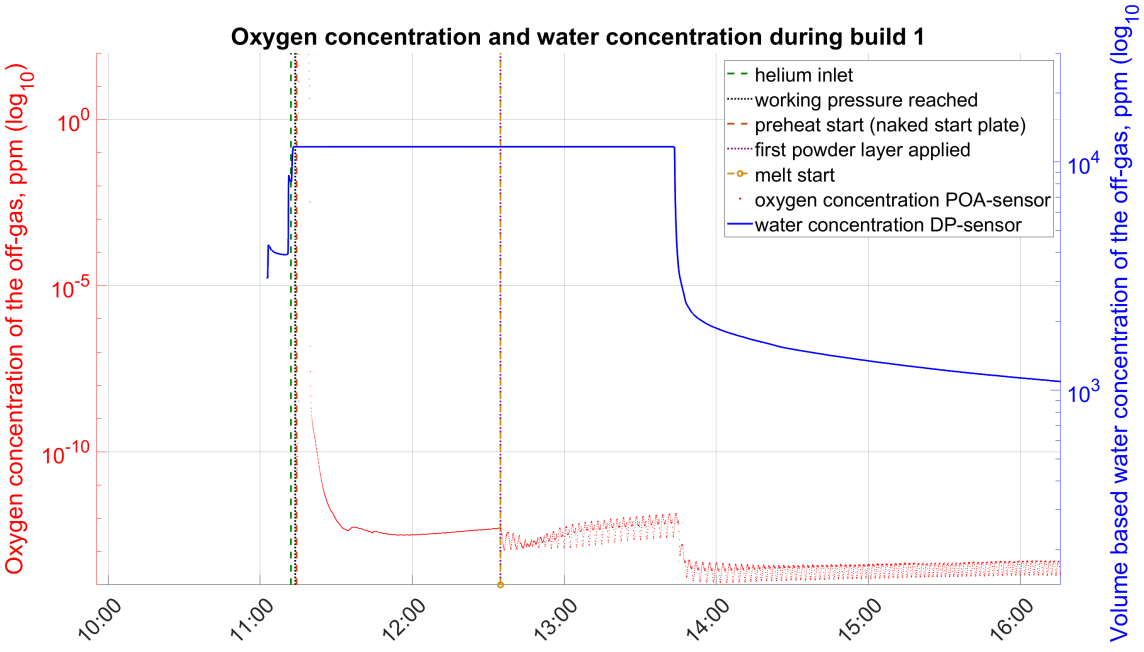

(b)

Figure B.10: An overlay for build cycle 1: The oxygen concentration in the off-gas (POA) plotted on the primary axis, and water concentration in the off-gas plotted on the secondary axis. The preheat, start and stop times are correlated from the log files collected by the internal EBM software.

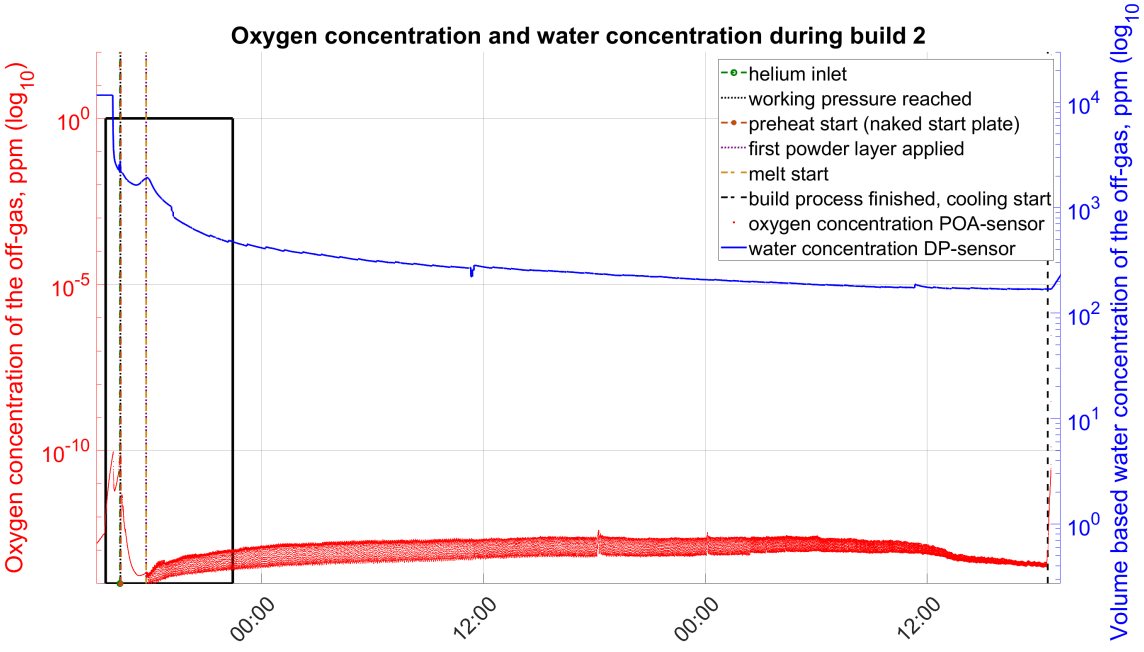

(a)

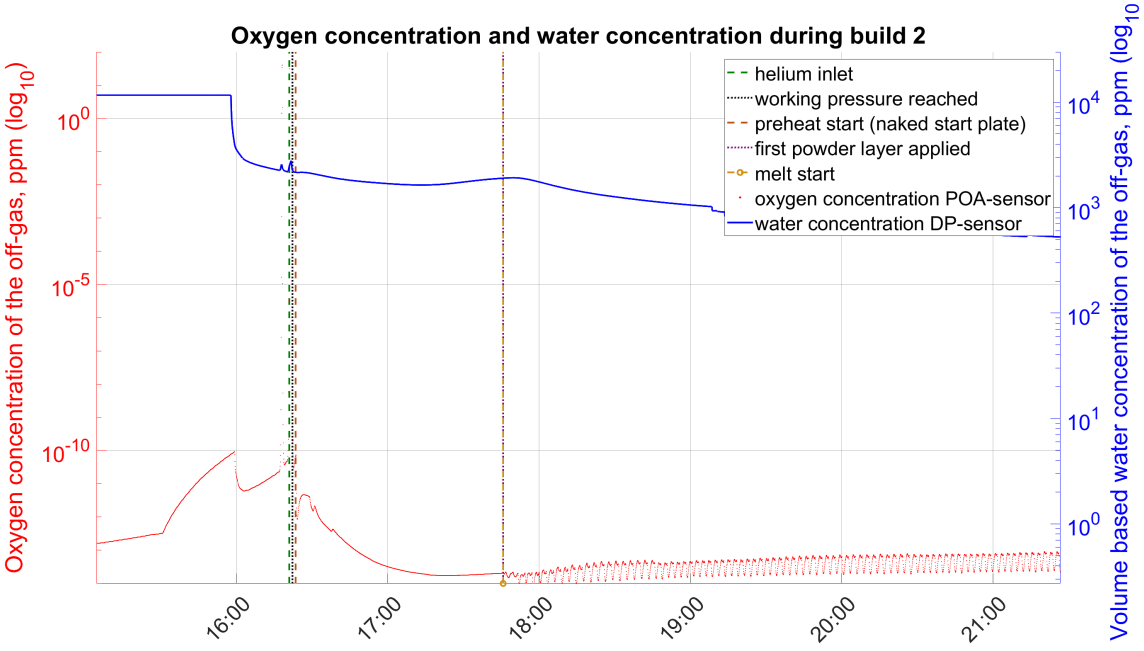

(b)

Figure B.11: An overlay for build cycle 2: The oxygen concentration in the off-gas (POA) plotted on the primary axis, and water concentration in the off-gas plotted on the secondary axis. The preheat, start and stop times are correlated from the log files collected by the internal EBM software.

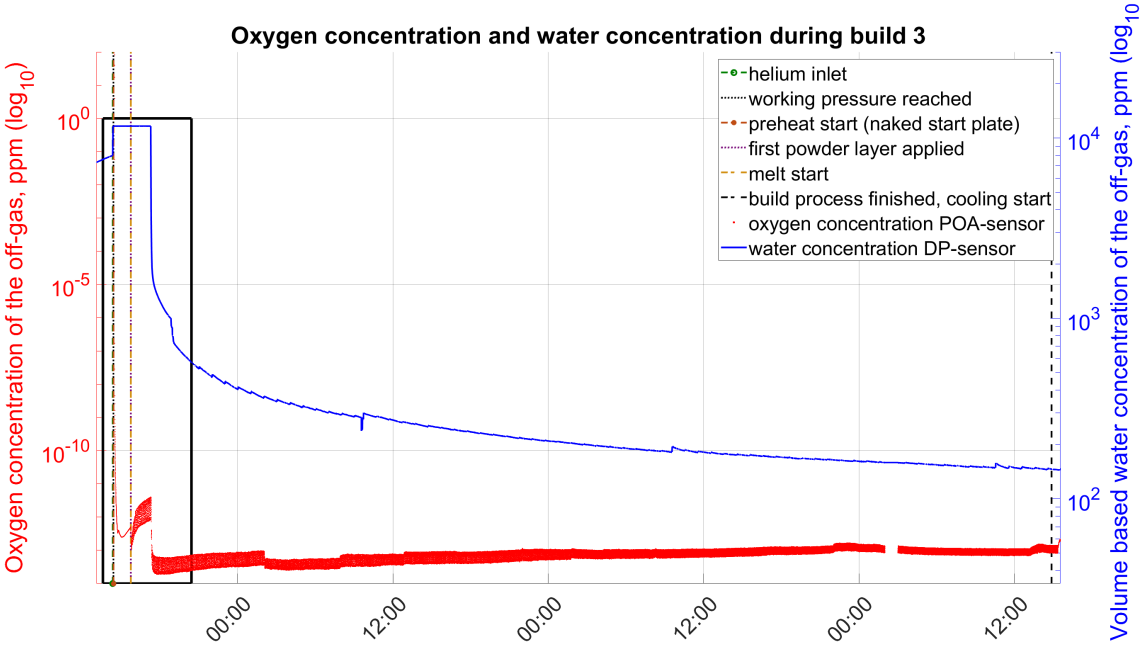

(a)

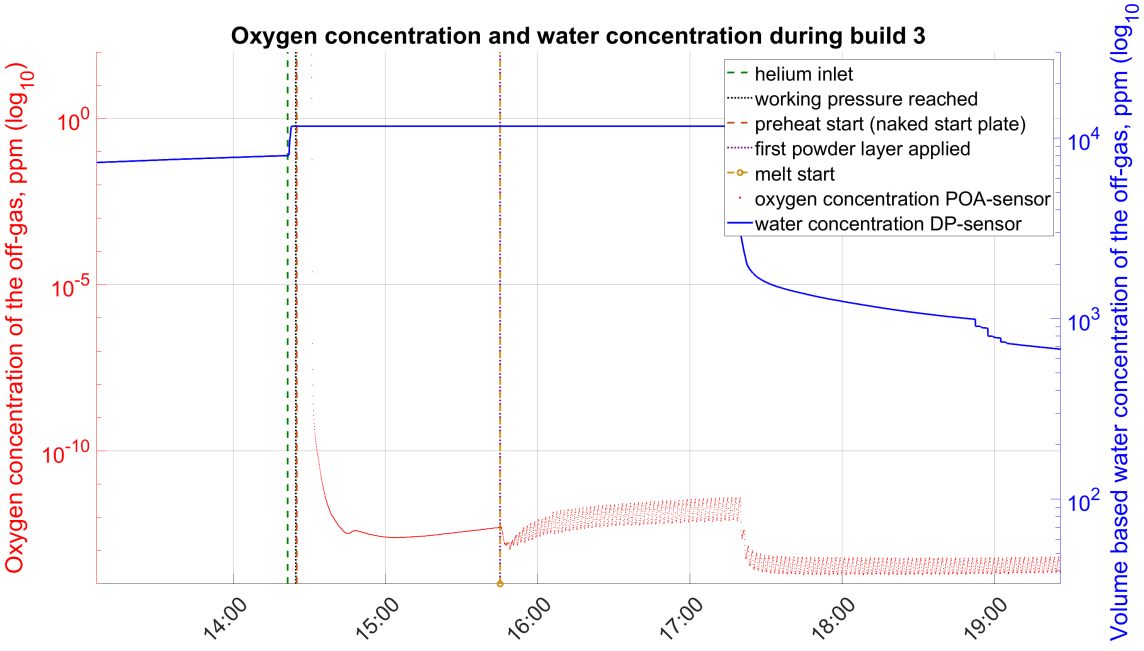

(b)

Figure B.12: An overlay for build cycle 3: The oxygen concentration in the off-gas (POA) plotted on the primary axis, and water concentration in the off-gas plotted on the secondary axis. The preheat, start and stop times are correlated from the log files collected by the internal EBM software.

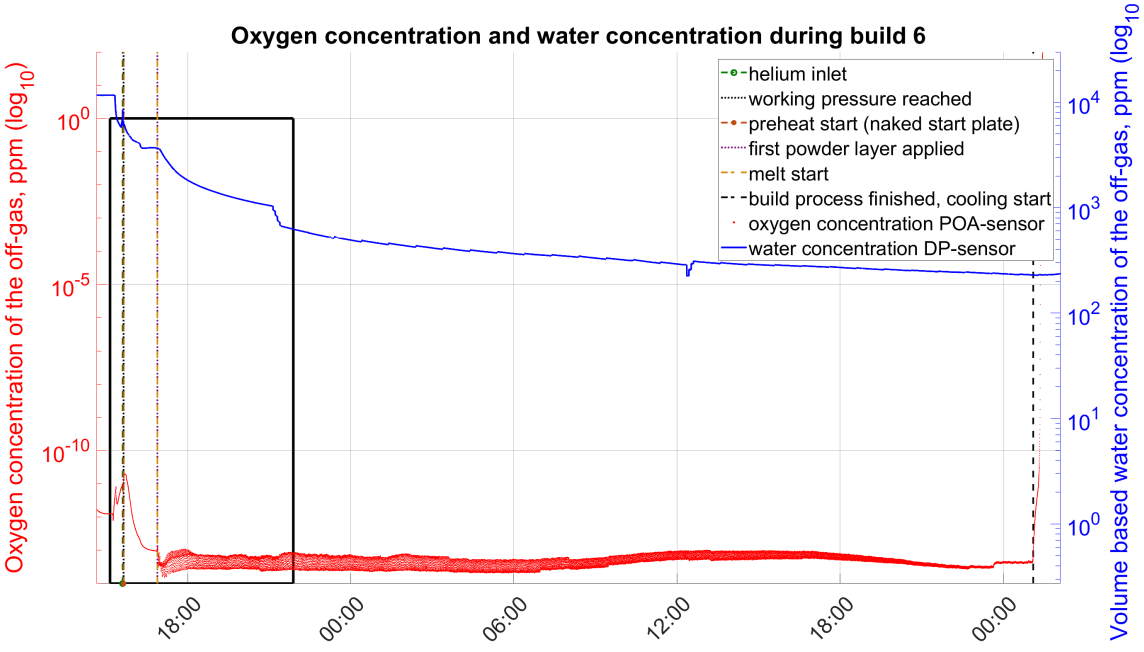

(a)

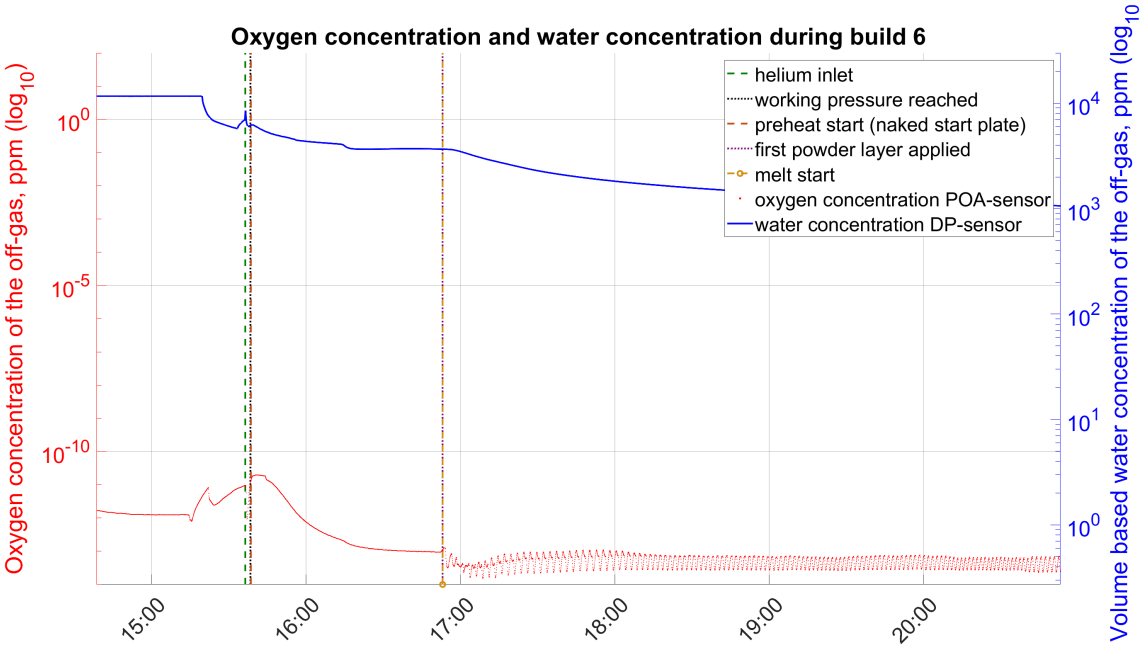

(b)

Figure B.13: An overlay for build cycle 6: The oxygen concentration in the off-gas (POA) plotted on the primary axis, and water concentration in the off-gas plotted on the secondary axis. The preheat, start and stop times are correlated from the log files collected by the internal EBM software.

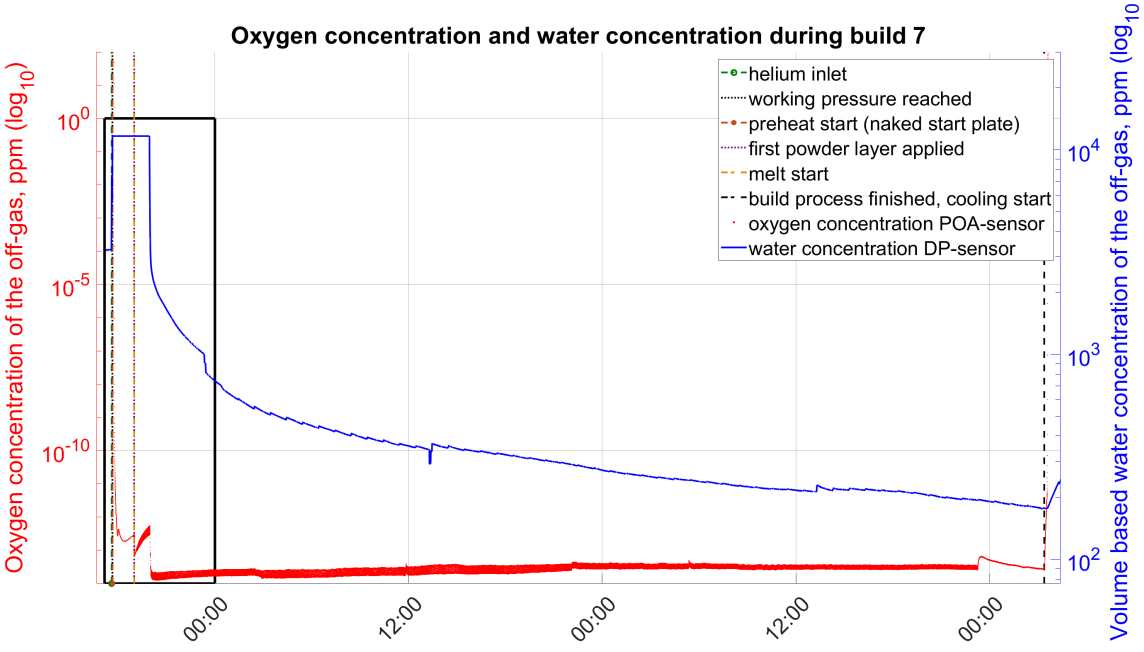

(a)

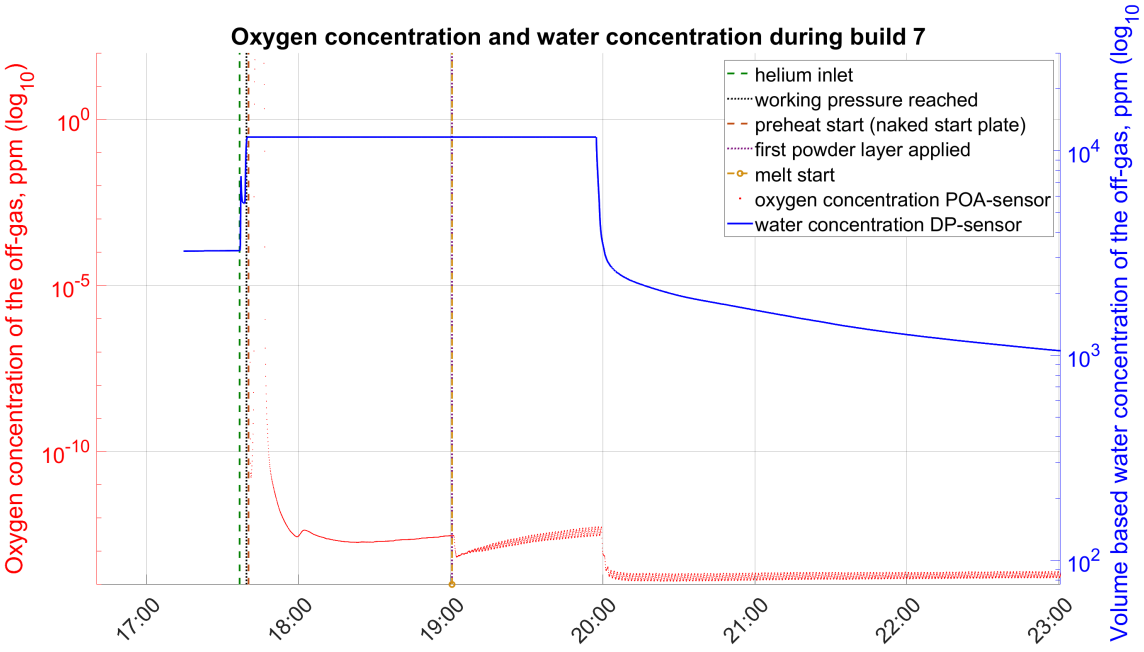

(b)

Figure B.14: An overlay for build cycle 7: The oxygen concentration in the off-gas (POA) plotted on the primary axis, and water concentration in the off-gas plotted on the secondary axis. The preheat, start and stop times are correlated from the log files collected by the internal EBM software.

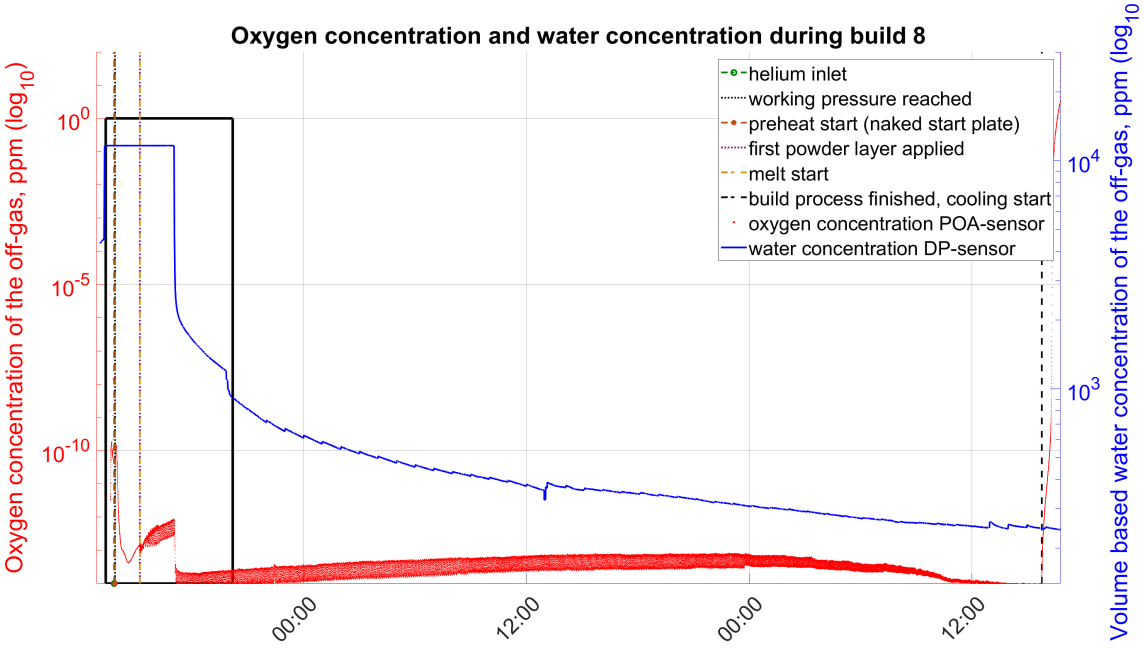

(a)

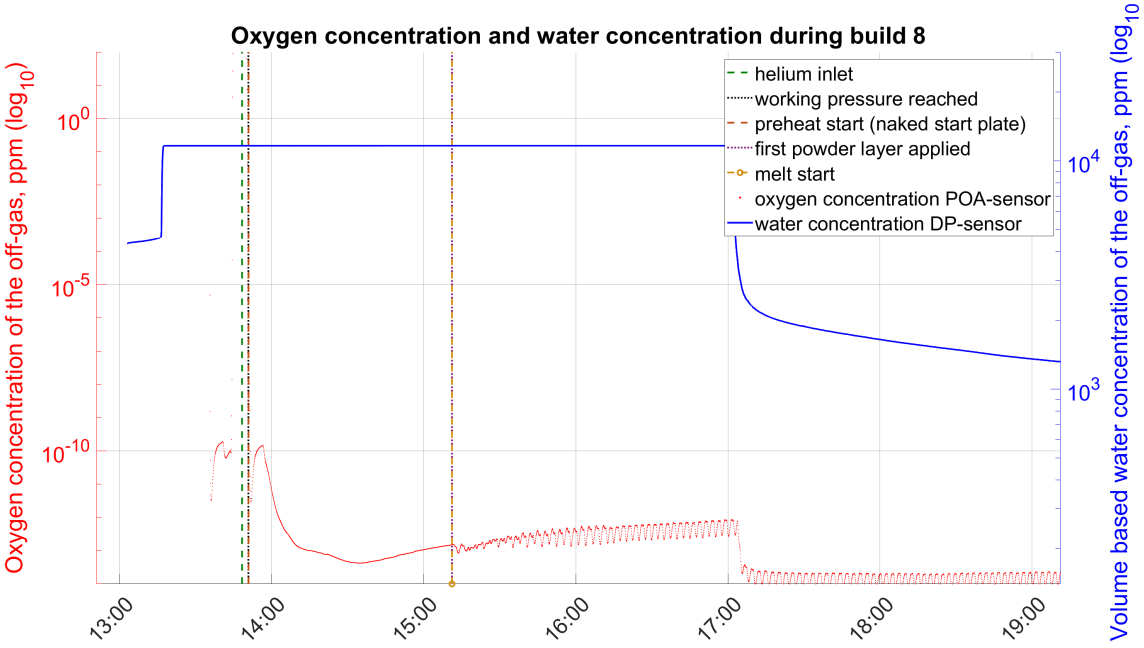

(b)

Figure B.15: An overlay for build cycle 8: The oxygen concentration in the off-gas (POA) plotted on the primary axis, and water concentration in the off-gas plotted on the secondary axis. The preheat, start and stop times are correlated from the log files collected by the internal EBM software.

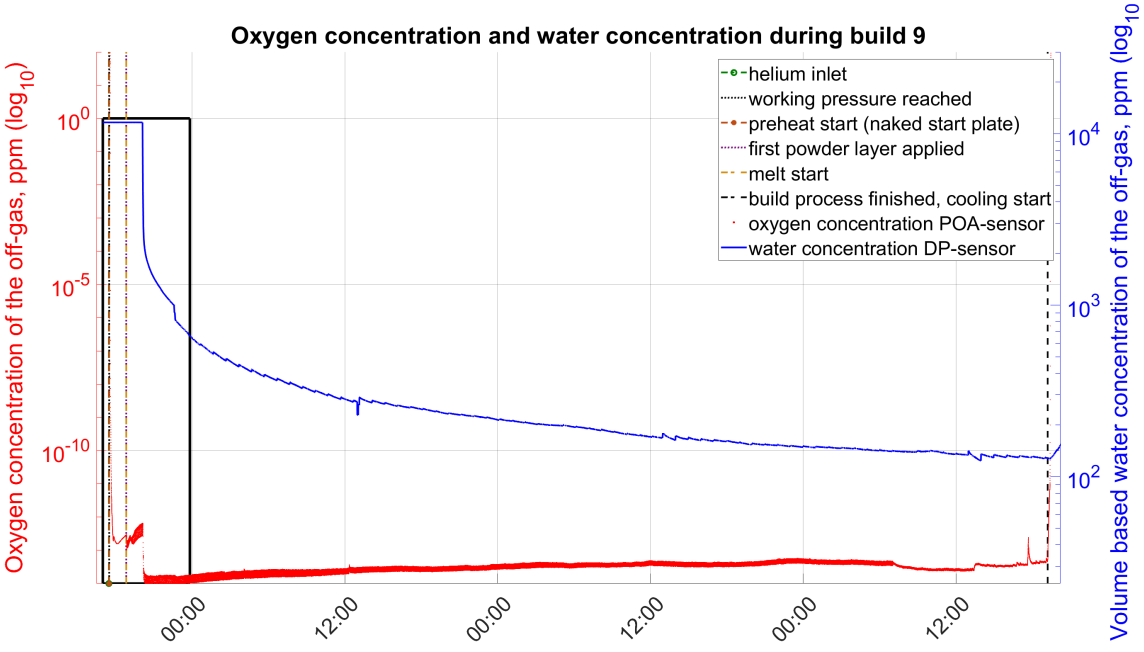

(a)

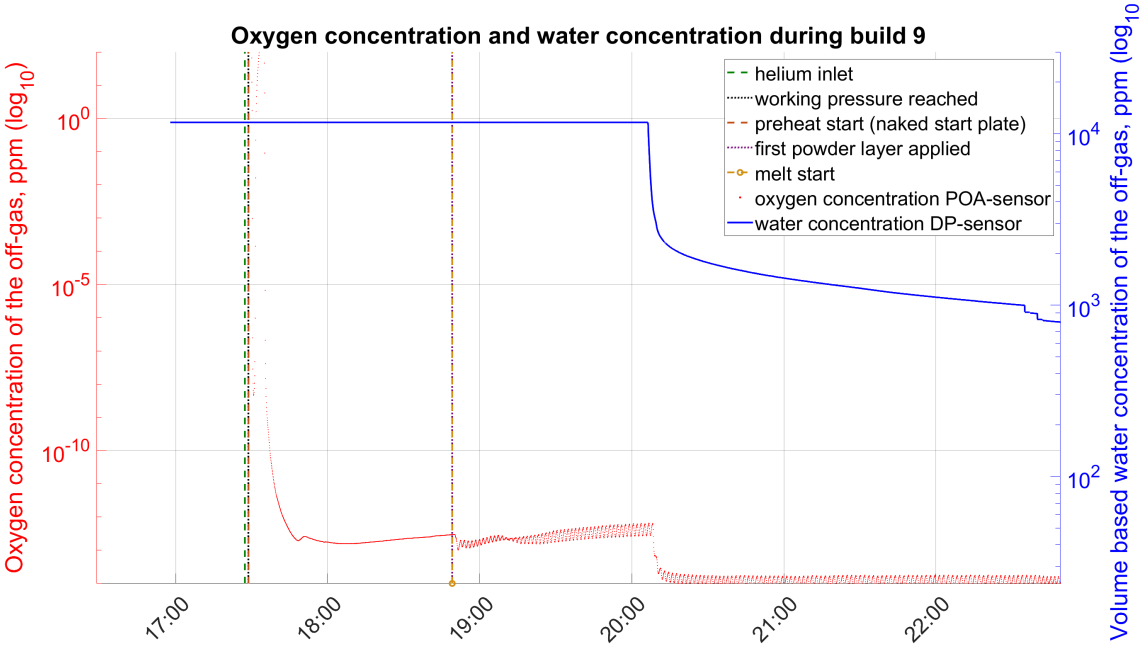

(b)

Figure B.16: An overlay for build cycle 9: The oxygen concentration in the off-gas (POA) plotted on the primary axis, and water concentration in the off-gas plotted on the secondary axis. The preheat, start and stop times are correlated from the log files collected by the internal EBM software.

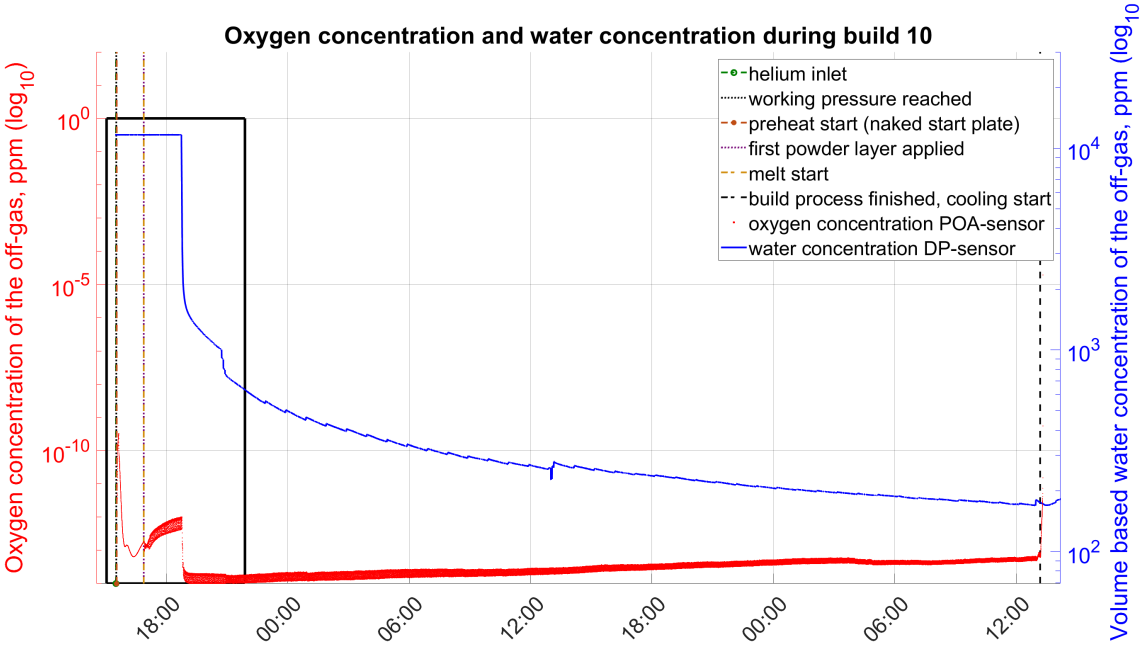

(a)

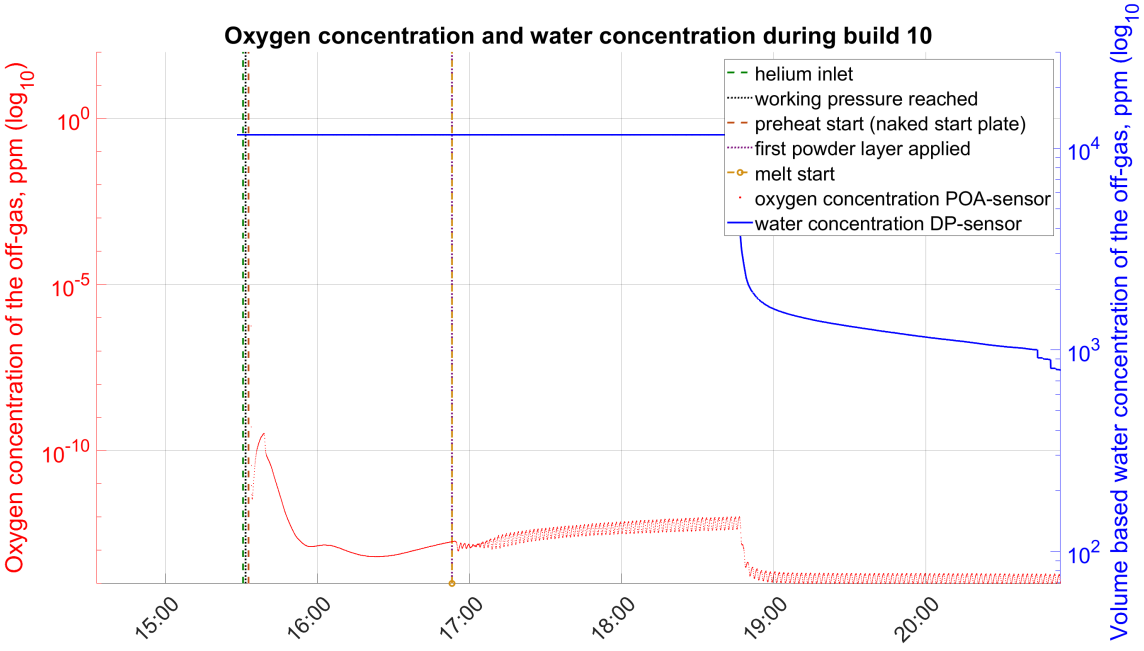

(b)

Figure B.17: An overlay for build cycle 10: The oxygen concentration in the off-gas (POA) plotted on the primary axis, and water concentration in the off-gas plotted on the secondary axis. The preheat, start and stop times are correlated from the log files collected by the internal EBM software.

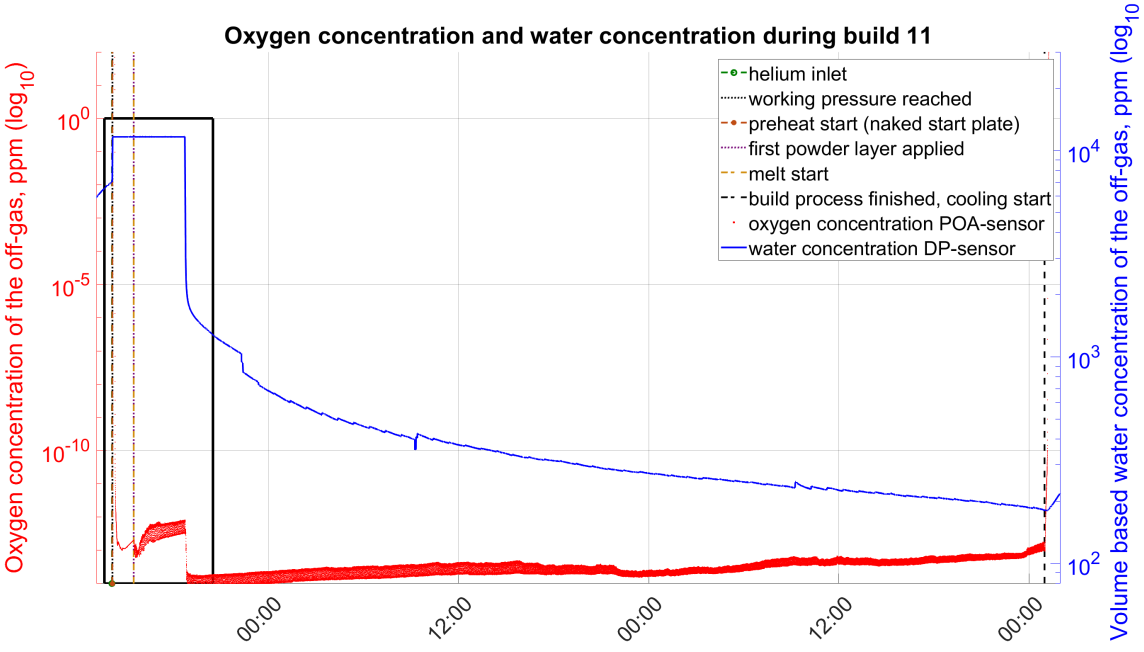

(a)

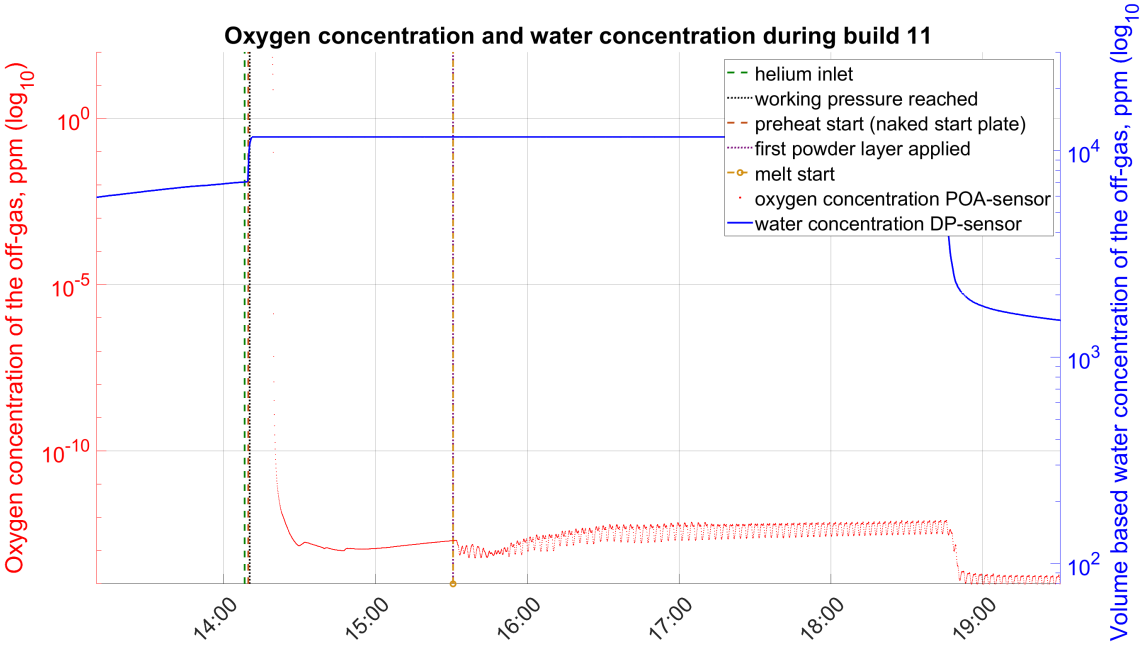

(b)

Figure B.18: An overlay for build cycle 11: The oxygen concentration in the off-gas (POA) plotted on the primary axis, and water concentration in the off-gas plotted on the secondary axis. The preheat, start and stop times are correlated from the log files collected by the internal EBM software.

C

SEM images

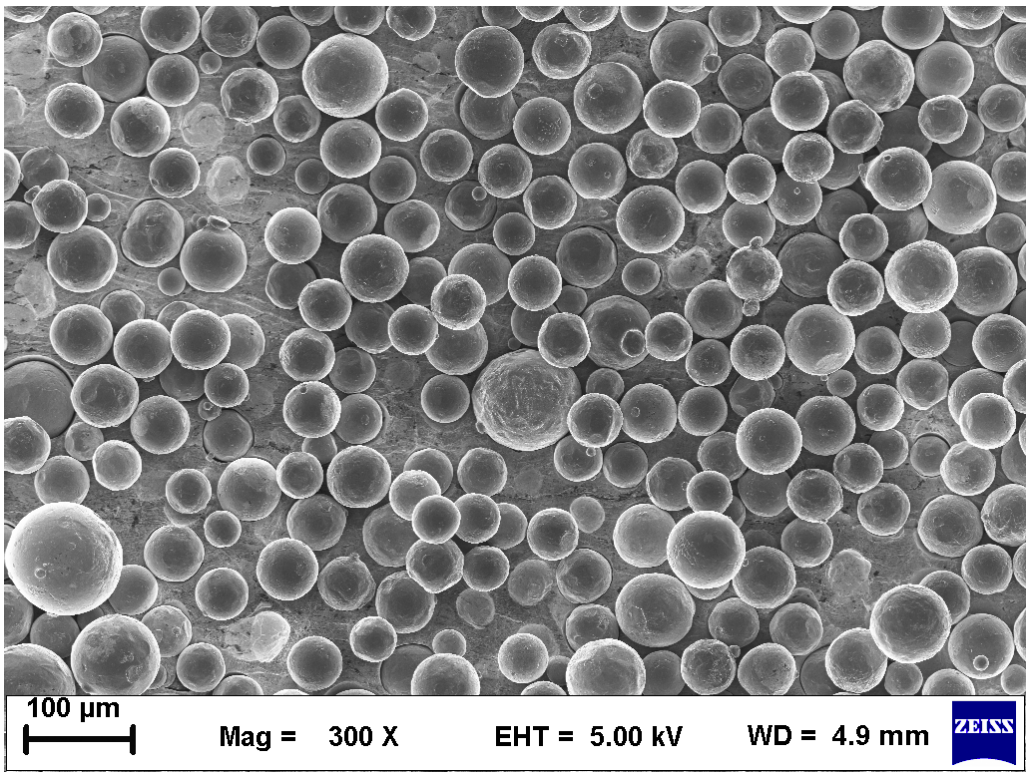

Figure C.1: B1-A, 300x

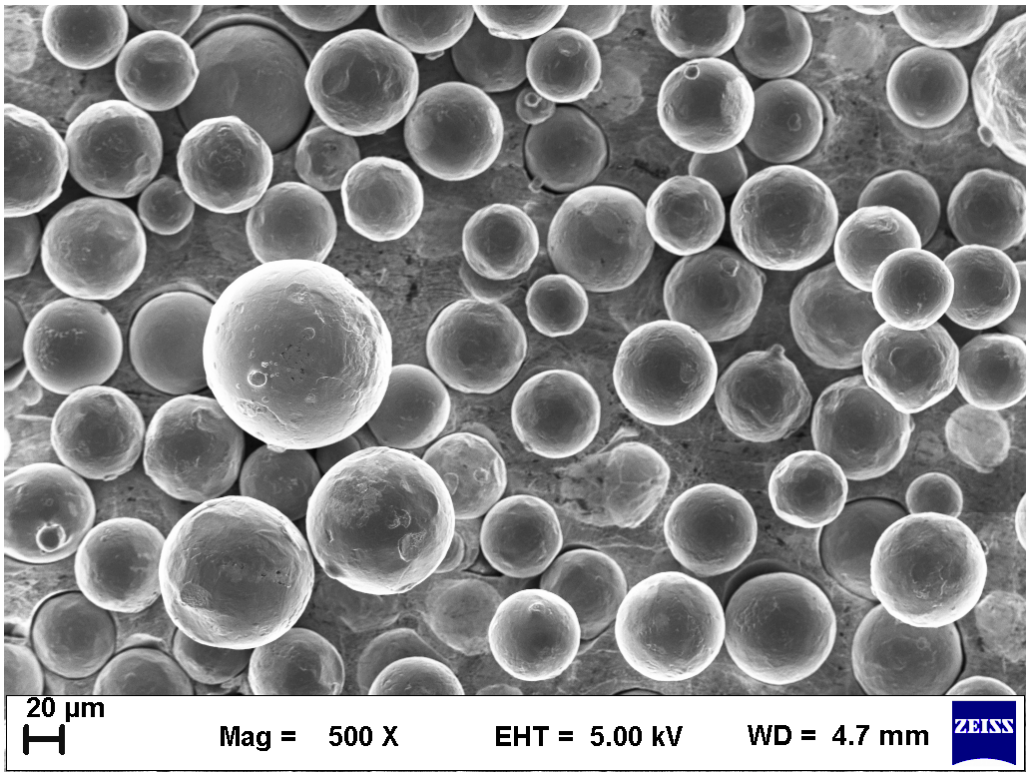

Figure C.2: B1-A, 500x

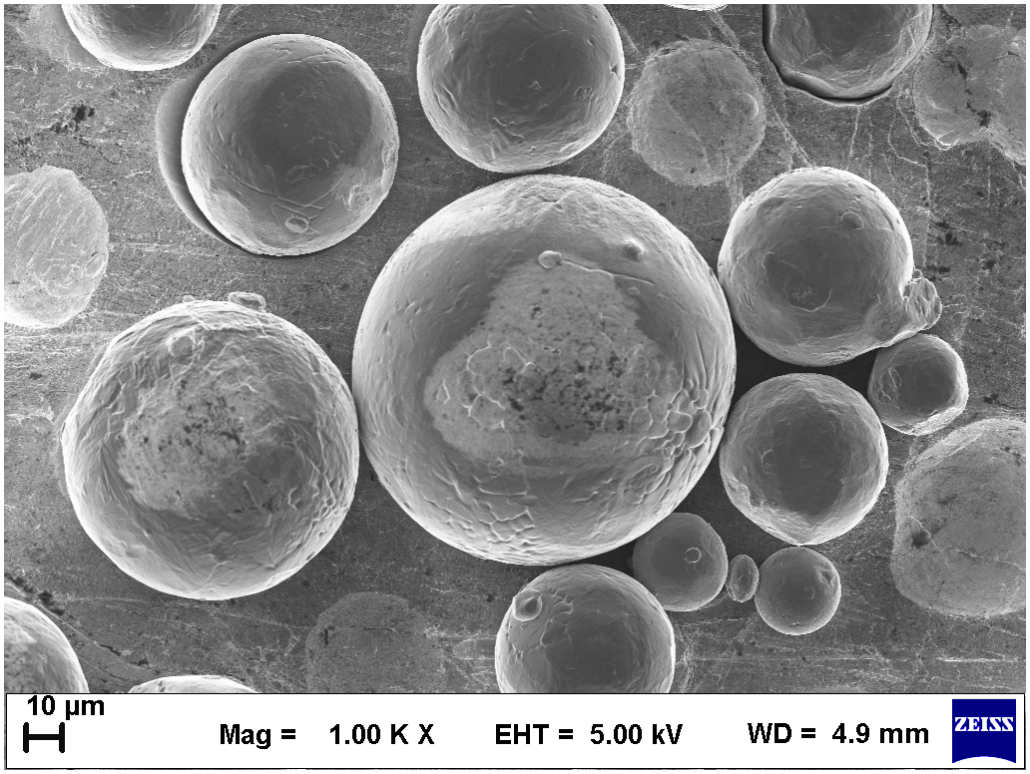

Figure C.3: B1-A, 1000x

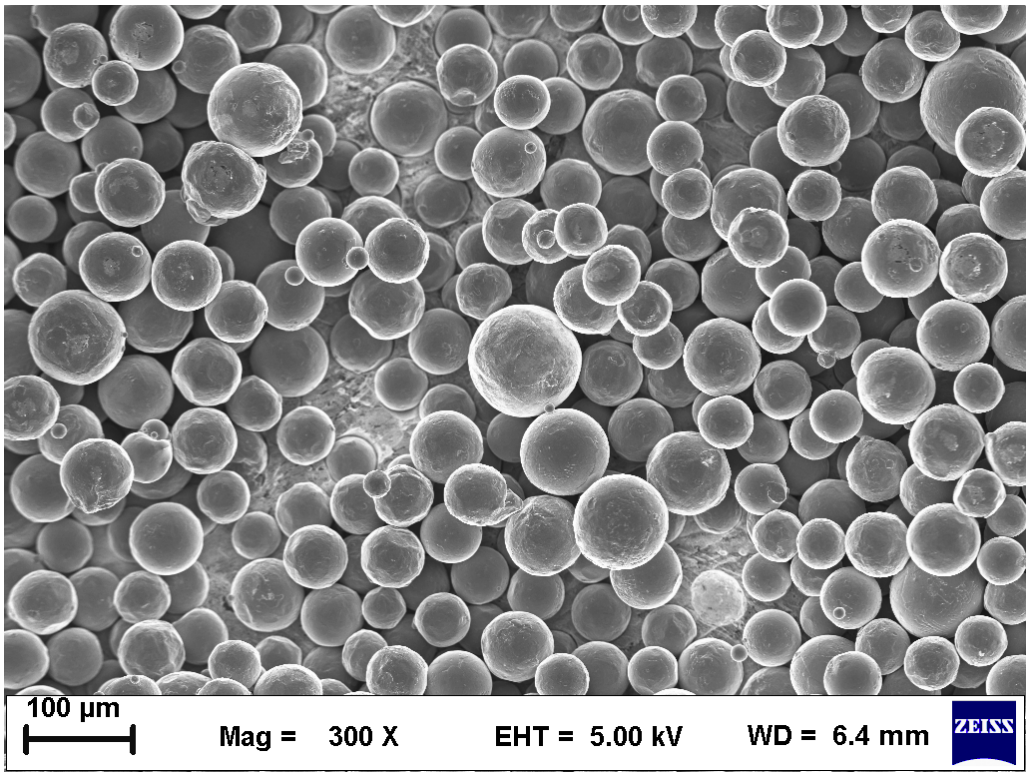

Figure C.4: B10-A, 300x

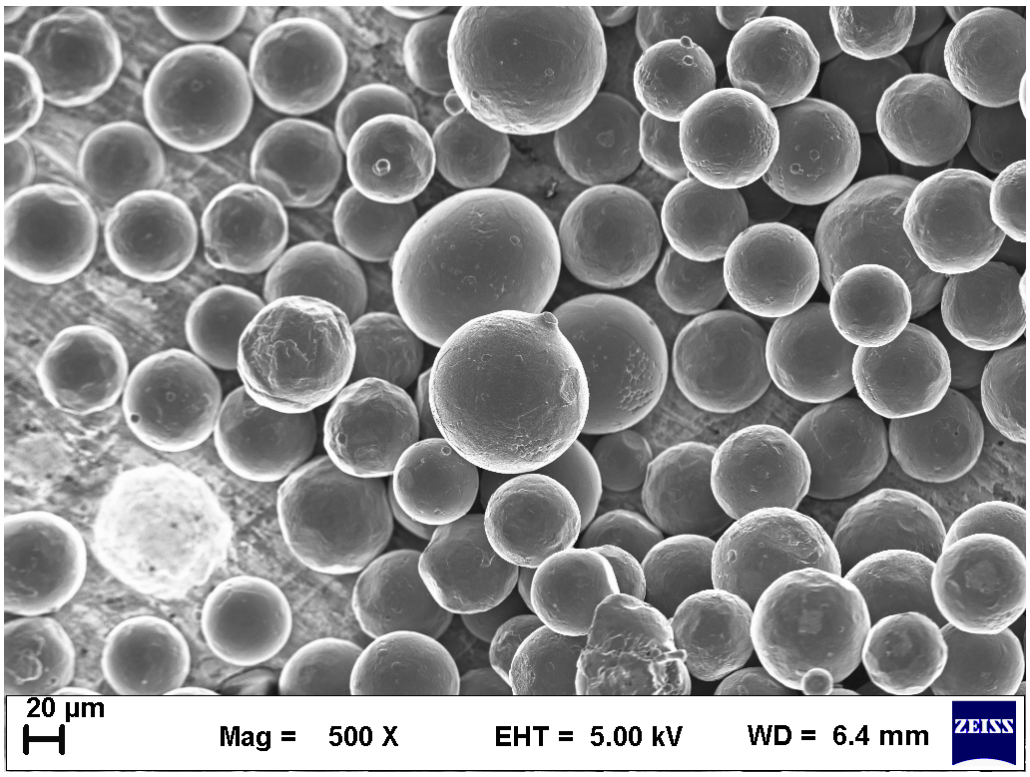

Figure C.5: B10-A, 500x

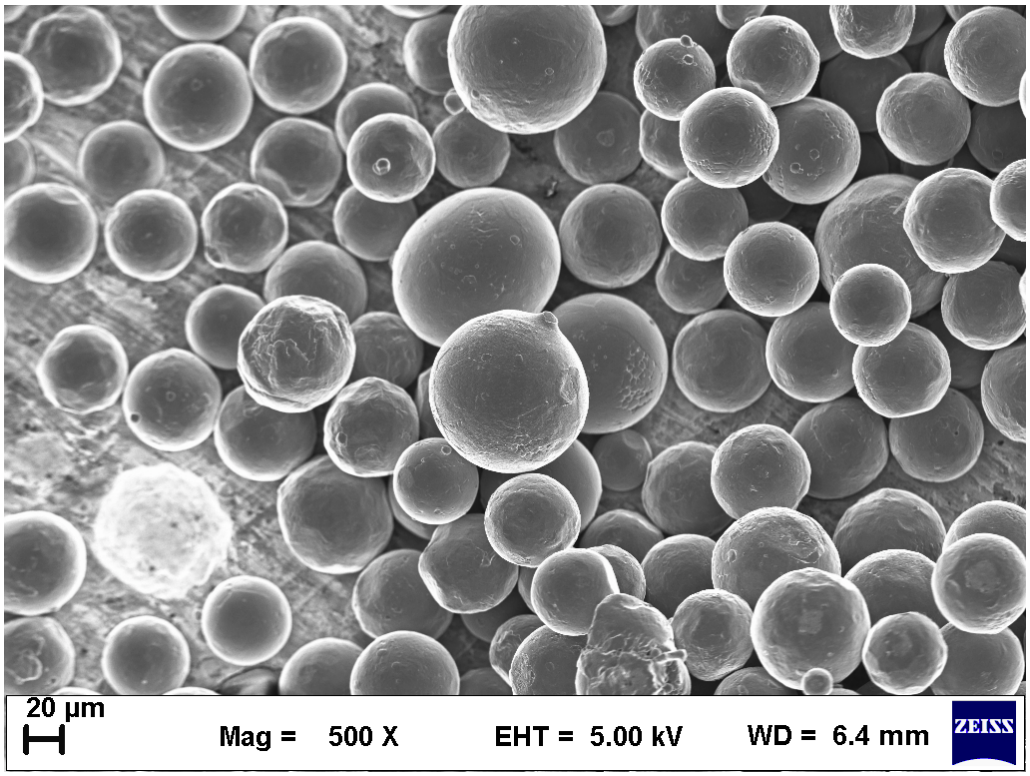

Figure C.6: B10-A, 1000x

DEPARTMENT OF INDUSTRIAL AND MATERIALS SCIENCE
CHALMERS UNIVERSITY OF TECHNOLOGY
Gothenburg, Sweden
www.chalmers.se

CHALMERS
UNIVERSITY OF TECHNOLOGY